nature climate change

SUPPLEMENTARY INFORMATION

DOI: 10.1038/NCLIMATE2921

Future cost-competitive electricity systems and their impact on US CO_2 emissions

A. E. MacDonald,[1*] C. T. M. Clack,[1,2*] A. Alexander,[1,2]
A. D. Dunbar,[1] J. Wilczak,[1] Y. Xie[1]

[1]National Oceanic and Atmospheric Administration
325 Broadway Boulder, Colorado 80305, USA

[2]Cooperative Institute for Research in Environmental Sciences
University of Colorado, Colorado 80305, USA

*Correspondence to: alexander.e.macdonald@noaa.gov; christopher.clack@noaa.gov.

The supplemental materials for the paper future cost-competitive electric systems and their impact on US CO_2 emissions. The methods are written in section 1. Supplemental results are shown in section 2. A summary of the major assumptions and features of the study conducted in the present paper are summarized in section 3.

Contents

List of Figures

List of Tables

1 Methods

1.1 Weather and Electrical Power Modeling

To adequately incorporate weather-driven renewable electricity into an electric grid system model requires an accurate assessment of the wind and solar electricity capable of being generated. The wind and solar electricity production depends, among other things, on characteristics of the weather, which are best provided by numerical weather prediction (NWP) assimilation models that are used for operational weather forecasting. Operational NWP models assimilate large amounts of local and global meteorological observations routinely, and provide consistent meteorological information over large geographic areas. The assimilation model data used should be of high temporal and spatial resolution, so as to realistically depict the variability of the atmosphere over the time and spatial scales required by the power system. The present paper has leveraged many years of development of high-resolution assimilation models at the National Oceanic and Atmospheric Administration, and uses the data to investigate cost-optimized wind and solar electricity production within the US electric power system for cost projections to 2030.

High-spatial-resolution weather data facilitates the ability to have different sized electric power systems each containing a relatively large number of potential wind and solar resource sites for the optimization model to select from. Severely limiting the number of choices for the optimization restricts the fidelity and value of the model. For the present study there were a total of 36,791 model grid cells identified as potential wind and/or solar resource sites, from a possible $\sim$152,000 (see section 1.2 on how sites were discarded). For comparison, the Renewable Electricity Futures study (REFS) led by the DOE/ National Renewable Energy Laboratory had 356 wind (with five different technologies available) and solar sites for the entire US (*8*), while the SWITCH model being developed at the University of California, Berkley currently only models the Western Interconnect and has a total of 1,527 sites for wind (*15*). As a result, the present study provides maps of optimal wind and solar sites down to the 13km model grid resolution of the spanning the entire Contiguous United States (CONUS), something not available from these previous studies.

The temporal resolution of the meteorological data is also essential for generating a realistic optimal solution. We produced three years of data at hourly resolution for all of the resource sites, resolving diurnal, weekly, seasonal, and annual resource variations. At least one chronological year of hourly data were used for any individual analysis. In comparison, REFS used 17 time-slice averages, while the SWITCH study used 12 monthly averaged 24-hour diurnal profiles, for a total of 280 effective time steps. The higher temporal resolution allows for a more accurate dispatch of electricity required to keep the grid in continuous balance. The remainder of the present subsection describes the methodology of how the weather datasets were obtained and processed into power data.

1.1.1 Weather Data

The primary meteorological data utilized were obtained from the analysis fields of the 13-km Rapid Update Cycle (RUC) assimilation model (*33, 34*) used operationally at the National Centers for Environmental Prediction (NCEP) from 1998 until 2012. The RUC utilizes 3-D variational analysis (3DVAR), where the

cost function is given by (*35*)

$$J(\mathbf{x}) = \frac{1}{2}(\mathbf{x}-\mathbf{x}_b)^T\mathbf{B}^{-1}(\mathbf{x}-\mathbf{x}_b) + \frac{1}{2}\left[\mathbf{y}-\mathbf{H}(\mathbf{x})\right]^T\mathbf{R}^{-1}\left[\mathbf{y}-\mathbf{H}(\mathbf{x})\right], \quad (1)$$

where $\mathbf{x}$ is the analysis vector, $\mathbf{x}_b$ is the model background vector, $\mathbf{B}$ is the static background error covariance matrix, $\mathbf{y}$ is the observation vector, $\mathbf{H}$ is the (linearized) observation operator, and $\mathbf{R}$ is the observation error covariance matrix. The output analysis field is the minimization of Eq. (1) at $\mathbf{x} = \mathbf{x}_a$. For the model background vector, the RUC uses the previous hour's cycle forecast hour one, so the change in the variables due to the NWP physics from the analysis time is relatively small. The RUC procedure uses Gridpoint Statistical Interpolation (GSI) 3-DVAR followed by a Digital Filter Initialization (DFI) to enhance variable consistency. The data assimilation in the RUC used in excess of 20,000 observations each hour, making it extremely data rich and highly constrained. Since the RUC is updated every hour, we had access to the analysis field for almost all hours for the three-year period of 2006–2008 (for 2.4% of the hours, the archived data were either corrupted or contained missing cycles). The critical point to this approach is that the weather data input here is a highly accurate estimation of the state of the atmosphere over the contiguous US. Further, lengthy forecasts are not required since we use the model analysis fields, which removes a potential source of error from the dataset. The full three-dimensional RUC assimilation matrices were collated and stored to be used for power modeling (described in subsection 1.1.2).

The RUC assimilation model output did not include analysis fields for shortwave or long-wave radiation. Therefore, to enable the production of an accurate solar dataset, we use a combination of RUC analysis model variables (hydrometeors, pressure, temperature, and relative humidity) together with satellite data. Geostationary Operational Environmental Satellite (GOES) data were obtained every 15 minutes for the three-year period. The data we obtained were in five channels; three in the infrared spectrum (shortwave 4-micron, long-wave 11-micron, and long-wave 13-micron), the visible spectrum, and a water vapor channel. There was a small percentage of time when satellite data were unavailable due to maintenance or other malfunctions, which resulted in a dataset with 87.99% of the hours having all five channels. The spatial resolution of the satellite data is 4-km, except for the visible which is 1-km.

Since the spatial resolution of the RUC is at 13 km and the temporal resolution is 60 minutes, we perform averaging to bring the satellite data to the RUC model space. A decision was made to scale to the coarser resolution to keep the mathematical optimization more tractable. The spatial averaging is a cubic-spline fit from 4-km (and 1-km) to the 13-km grid. The temporal interpolation was only used if the top of the hour (hh:00) was not available (aligned to the NWP analysis hour), and a linear interpolation was applied for successive 15-minute intervals around the top of the hour up to a maximum of 45 minutes each side of that hour. If there were no data for the whole period of (hh-1):15–hh:45 no interpolation was applied and no satellite data is reported. In total, we created a satellite dataset that has all five channels on 23,145 hours of the possible 26,304 hours between 2006–2008. When there was no satellite data, the irradiance model used just the RUC assimilation model data.

It would have been possible to use an existing algorithm to estimate solar irradiance, see e.g., (*36–39*), but when the project began they were very new. In addition, they were being produced on different grids and solely relied on satellite data. We decided to produce a solar irradiance dataset that was temporally and spatially aligned with the wind speed dataset. Thus, we needed to devise a method to produce the solar

irradiance estimates. To enable that goal, we collected solar measurements from the SURFace RADiation budget (SURFRAD) network [www.esrl.noaa.gov/gmd/grad/surfrad/] and the Integrated Surface Irradiance Study (ISIS) Network [www.esrl.noaa.gov/gmd/grad/isis/]. These two networks provide some of the best quality solar irradiance measurements over the contiguous US. For more information of the two networks, see e.g., (*40–42*). The locations of the SURFRAD sites used are: Bondville IL, Table Mountain CO, Desert Rock NV, Goodwin Creek MS, Fort Peck MT, Penn State University PA, and Sioux Falls, SD. The locations of the ISIS sites used are: Albuquerque NM, Madison WI, Salt Lake City UT, Sterling VA, Hanford CA. There are three sites from the ISIS network that were not active during the study dates of 2006–2008 and, therefore, are not included (Seattle WA, Bismarck ND, and Tallahassee FL).

The SURFRAD and ISIS site measurements of direct normal irradiance (DNI), diffuse horizontal irradiance (DHI), and zenith angle are taken as the truth and are provided at a frequency of three minutes. The SURFRAD and ISIS sites measure global horizontal irradiance (GHI); however, the direct GHI measurements are less accurate than calculating the GHI from the DNI and DHI measurements, known as the component-sum technique (*43*)

$$\mathrm{GHI} = \mathrm{DNI} \cdot \cos\left(\mathrm{sza}\right) + \mathrm{DHI}, \tag{2}$$

where $\cos\left(sza\right)$ is the cosine of the zenith angle at the site.

To compensate for the fact that the SURFRAD and ISIS sites are point measurements and the RUC assimilation model variables represent a grid cell average, we averaged the solar irradiance measurements over time. The solar irradiance measurements are averaged from six minutes before the top of the hour to six minutes after the top of the hour (five measurements). The averaging time was chosen to match the average advection time of clouds through a RUC grid cell (see section 1.1.2). It is designed to be short enough that the clouds do not have enough time (on average) to advect fully out of a RUC grid cell, but long enough to provide some averaging of scattered clouds. We investigated several averaging time scales and determined that the chosen time scales gave the best overall performance. The ground measurements were temporally aligned with the assimilation data and the satellite data and quality control was performed. The instrument errors were taken to be $\pm 1\%$ of the observed value (see documentation at www.esrl.noaa.gov/gmd/grad/instruments.html).

In addition to the weather, satellite, and ground irradiance data, we constrained the data from above, by computing the solar irradiance falling onto the top of the atmosphere for each hour, taking into account the eccentricity of the Earth's orbit. The average extraterrestrial irradiance (I_0), about which the irradiance fluctuates, is 1366 Wm^{-2} (*44*). The equation for the extraterrestrial irradiance outside the Earth's atmosphere (normal to the photosphere of the sun) is:

$$\mathrm{DNI}_0 = I_0 \cdot \left(\frac{R_{av}}{R}\right)^2 \tag{3}$$

where R_{av} is the mean Sun-Earth distance and R is the actual Sun-Earth distance at a specific instant. We use the approximation for $(R_{av}/R)^2$

$$\left(\frac{R_{av}}{R}\right)^2 \approx 1.000110 + 0.034221 \cdot \cos\left(\delta\right) + 0.001280 \cdot \sin\left(\delta\right) + 0.000719 \cdot \cos\left(2\delta\right) + 0.000077 \cdot \sin\left(2\delta\right). \tag{4}$$

Here $\delta = 2\pi d/365.242$ radians, and d is the day of the year (*45*). Another parameter that we computed for the dataset was the solar zenith angle (sza), or more specifically, the cosine of the zenith angle. The solar zenith angle is defined as

$$\cos(sza) = \sin(lat) \cdot \sin(dec) + \cos(lat) \cdot \cos(dec) \cdot \cos(ha), \tag{5}$$

where dec is the declination angle, ha is the hour angle, and lat is the latitude in radians. The declination angle can be approximated by

$$dec = \epsilon \cdot \sin[\delta + \frac{\pi}{180} \cdot (279.93 + 1.915 \cdot \sin(\delta) - 0.0795 \cdot \cos(\delta) + 0.02 \cdot \sin(2\delta) - 0.00162 \cdot \cos(2\delta))] \tag{6}$$

where ϵ is the Earth's axial tilt or obliquity of the ecliptic in radians (0.409173^c). The hour angle is simply computed as

$$ha = \pi \cdot \left(1 - \frac{hr}{12}\right) - lon, \tag{7}$$

with hr being the hour of the day in UT and lon is the longitude in radians.

To produce solar irradiance estimates, we use the technique of multiple multivariate linear regression. The regression can be represented mathematically as (*46–48*)

$$Y_{n\times p} = X_{n\times(r+1)} \cdot \beta_{(r+1)\times p} + \varepsilon_{n\times p}, \tag{8}$$

where $Y_{n\times p}$ are the endogenous variables or regressands, $X_{n\times(r+1)}$ are the exogenous variables or regressors, $\beta_{(r+1)\times p}$ are the effects or regression coefficients, and $\varepsilon_{n\times p}$ are the disturbance or error terms. In Eq. (8), n is the number of observations, p is the number of different properties modeled, and $(r+1)$ is the number of independent inputs. For our specific cases; Y is the ground-based measurements of GHI, DNI, and DHI, X is the NWP model variable (the hydrometeors, temperature and water vapor) and satellite data, ε is the residuals from the model compared with the data, and β is the regression coefficients to be applied to all other locations when the training set has been regressed against. The training set contains the data from the SURFRAD and ISIS sites along with the corresponding satellite data at those locations. We assumed that the expected value of the error term is zero, that is $E(\varepsilon_i) = 0$. We also assumed that the errors are independent between types of irradiance, that is $cov(\varepsilon_i, \varepsilon_k) = \sigma_{ik} I$, $i, k = 1, 2, ..., p$ (I being the identity matrix). The solution of the multiple multivariate linear regression can be found to be

$$\hat{\beta} = (X'X)^{-1} X'Y, \tag{9}$$

with $\hat{\beta}$ being the estimators of the regression. Equation (9) is derived by minimizing Eq. (8). The minimization finds the smallest sum of deviations from *all* the independent variables. The estimators are placed into

$$I_q = \sum_{j=1}^{r+1} \hat{\beta}_j \cdot x_j, \tag{10}$$

to model the irradiance at all locations over the domain being studied. I_q is the estimated GHI, DNI, or DHI at a single instant (hour).

The performance of the technique is assessed via the mean-bias error (MBE) at hourly resolution and the adjusted multiple linear correlation coefficient, $\overline{R}$, which is defined as (*47*)

$$\overline{R}^2 = 1 - (1 - R^2)\frac{\rho - 1}{\rho - \eta - 1} = R^2 - (1 - R^2)\frac{\eta}{\rho - \eta - 1}, \tag{11}$$

where η is the number of regressors and ρ is the sample size. Table 1 shows the $\overline{R}$ and MBE for the solar irradiance estimates. The regression is best for GHI. It is less accurate for the DNI and DHI components, but as we are estimating solar PV power, the most important term is the GHI. The estimates have low bias for all irradiance species that will result in a conservative estimate for power production at the solar PV sites.

Table 1: The adjusted multiple correlation coefficient and mean-bias error for the solar irradiance estimates.

	$\overline{R}^2$	MBE
GHI	89.37%	-2.82%
DNI	65.91%	-12.41%
DHI	66.26%	-4.19%

1.1.2 Power Modeling

The wind speed estimates for use in power modeling are obtained from the weather data described in subsection 1.1.1. The conversion from wind speed to power is defined by the well-known equation (*49*)

$$P = \frac{1}{2}C_p \rho A U^3. \tag{12}$$

In Eq. (12), ρ is the air density (kg/m^3), A is the area swept out by the wind turbine blades (m^2), U is the wind speed (ms^{-1}) and C_p is known as the coefficient of power.

Table 2: Turbines used to calculate the generic coefficient of power curves for the IEC classes.

	Turbine	Rated Power (MW)	Cut-In Speed (m/s)	Max Output Speed (m/s)	Cut-Out Speed (m/s)	Rotor Diameter (m)
IEC-I	Siemens 3.0 MW	3.0	3.0	14.0	25.0	101.0
	Gamesa G80	2.0	4.0	17.0	25.0	80.0
	Nordex N90HS	2.5	4.0	14.0	25.0	90.0
	Vestas V90	3.0	4.0	14.0	25.0	90.0
IEC-II	Vestas V112	3.0	3.0	13.0	25.0	112.0
	Siemens 2.3 MW	2.3	3.0	13.0	25.0	93.0
	GE1.6 82.5	1.6	4.0	12.0	25.0	82.5
	GE2.5xl	2.5	3.0	14.0	25.0	100.0
IEC-III	Vestas V100	1.8	3.0	12.0	20.0	100.0
	GE1.6-100	1.6	3.0	12.0	25.0	100.0
	Repower 3.2M	3.2	3.0	12.0	22.0	114.0
IEC-IV	Siemens 3.6 MW	3.6	4.0	14.0	25.0	107.0
	GE4.1MW	2.3	4.0	14.0	25.0	113.0
	Repower 6M	6.15	3.5	14.0	30.0	126.0

The coefficient of power is an empirically derived curve from simulations and performance of individual turbines. We take the composite of three or four specific turbines for each of the International Electrotech-

nical Commission (IEC) classes I, II, III and offshore (IV) and back calculate the C_p curves. The turbines used are found in Table 2. The C_p curves are shown in Fig. 1.

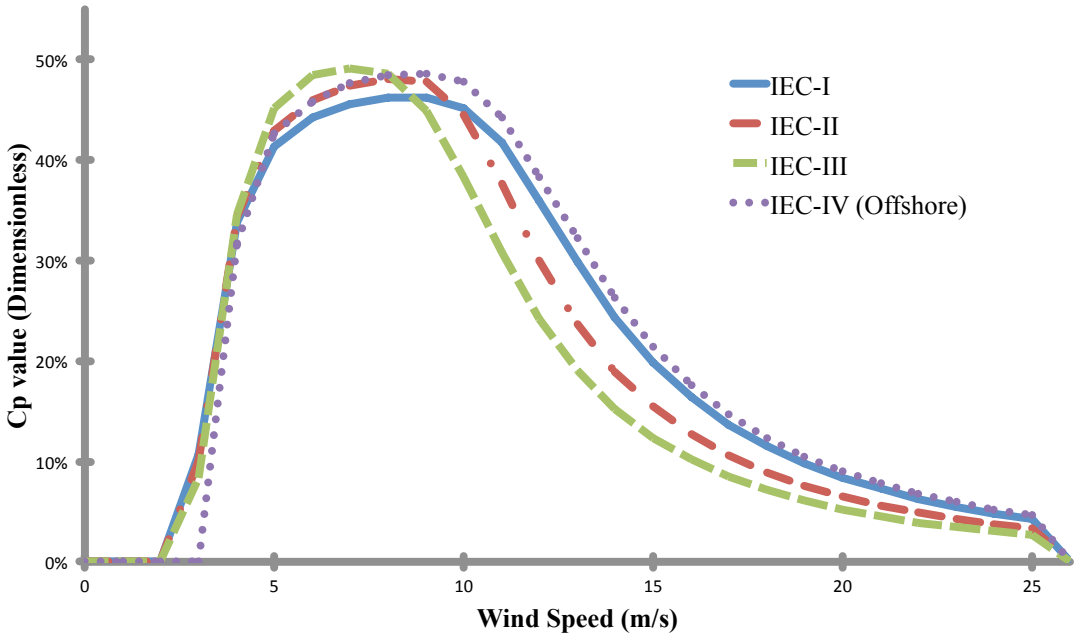

Figure 1: The coefficient of power (C_p) graph for the three IEC wind classes (IEC-I, II, III) and offshore wind (IEC-IV).

We define the rotor diameter to be 112 m for all terrestrial turbine classes and 123 m for the offshore class, which means the rated power of each turbine class is different. The choice to make all the turbine diameters the same simplifies the separation constraints set out in section 1.2. Since the rotor diameters are uniformly set (and is different to those in Table 2), the nameplate capacity for each class is a set value. For IEC-I the rated power modeled is 4.04 MW, the IEC-II is 3.14 MW, IEC-III is 2.52 MW, and IEC-IV is 5.25 MW. For the contiguous US, the three-year average of the wind speeds at 90 m was utilized to define which class was appropriate for which regions. Grid cells that have an average speed closest to 10 ms^{-1} are IEC-I, those closest to 8.5 ms^{-1} are IEC-II, and those closest to 7.5 ms^{-1} are class IEC-III. Offshore locations were found by using a land/sea mask. The classifications can be seen in Fig. 2. It shows that the US is predominantly IEC-III with small areas of IEC-II and even fewer locations of IEC-I.

To create the dataset of wind power estimates for the three years of 2006–2008, an algorithm was created that passed the wind speeds (U) through Eq. (12) along with the density from the model. To make the estimations more realistic, we defined conditions when the turbines should be turned off: temperatures below -20°C at 90 m Above Ground Level (AGL), below 0°C with precipitation falling in the lowest model vertical level, or below 0°C with clouds at 90 m AGL. The algorithm filters the power output for these three constraints and then outputs the final wind power estimations for all the sites. In a final step, we derated the power output by 5% for each turbine to account for maintenance and other down times. The result of the algorithm is hourly resolution wind power production at eachRUC model grid cell.

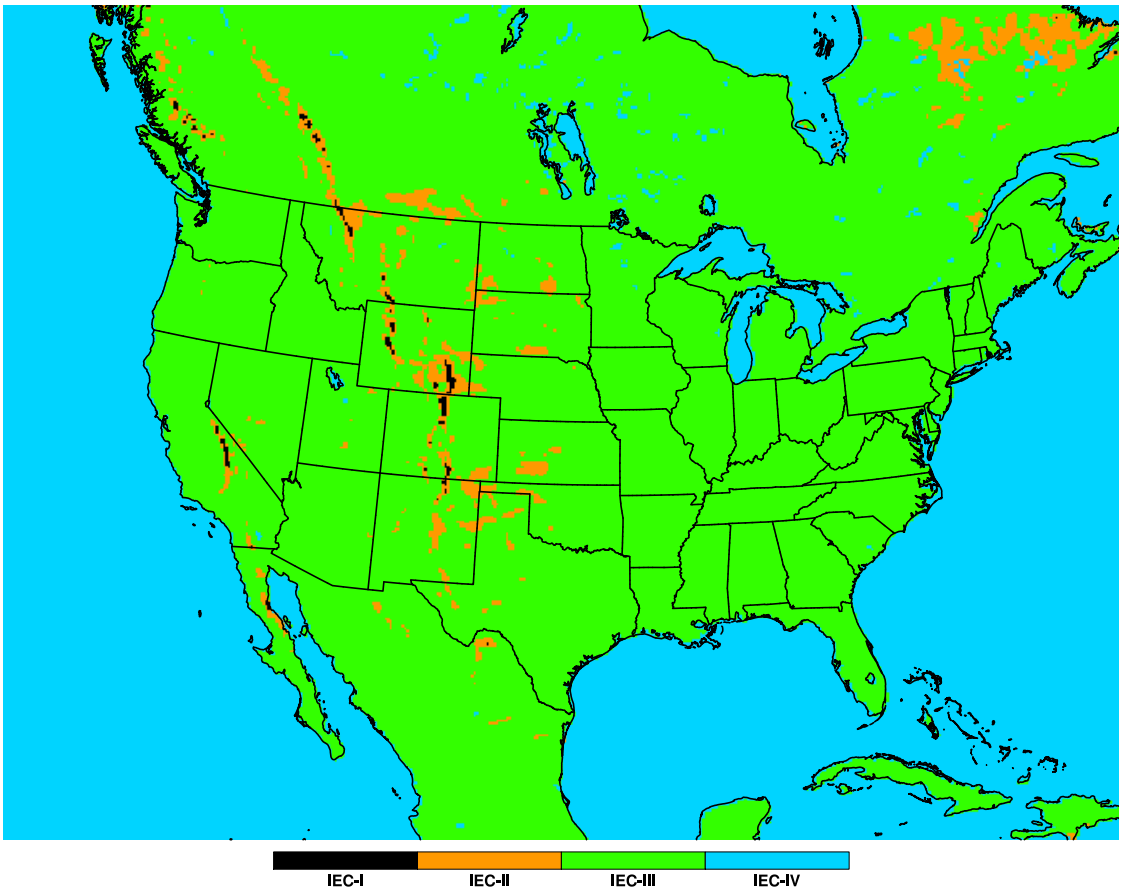

Figure 2: The classification of RUC grid cells. The black is IEC-I, orange is IEC-II, green is IEC-III, and blue is IEC-IV (offshore).

Next, we computed the solar photovoltaic power output from the GHI, DNI, and DHI solar irradiance estimates computed by the regression technique (see subsection 1.1.1). The irradiance estimates were inserted into the equations from Sandia National Laboratories for PV panel generation (*50*). In making the power estimates, we chose to use a standard solar panel for the year of 2007 taken from the NREL System Advisor Model (SAM) version 2012.5.11 (`https://sam.nrel.gov/`), namely the SunPower SPR-315E-WHT. The efficiency of these panels is 19.3%, which is at the high end for commercially available solar PV panels as of 2012 (*51*). We assumed that the panels would be mounted on a single-axis tracker and would be orientated north to south while being tilted at latitude, which results in the angle of incidence on the panels at all times of the day to be the declination angle of the Sun (*52*). The generic constants utilized by the power generation algorithm were obtained from (*53*), while the panel-specific constants were taken from the NREL SAM.

The mathematical formulae for the algorithm of power production are all contained within (*50*), so we do not repeat them here, but we do outline the major parts of the algorithm. First, we imported the solar irradiance estimates (GHI, DNI, DHI, and Solar Zenith Angle) along with any meteorological data (wind speed

at 10m and temperature at 2m). Second, we computed the solar cell temperature (taking into account the irradiance falling on the panel, ambient temperature, and wind speed) and the angle of incidence of the solar irradiance on the tilted and tracked panel. Third, we computed the energy falling onto the panel from the irradiance fields. Fourth, the current and voltages within the panel were approximated (the equations in (*50*) and NREL SAM are empirically derived). Finally, the current and voltage were combined to output the power for the panel. There are equations within the algorithm, which are based on NREL SAM, that computed the derating due to the panel structure and material. The output of the panel is restricted to 115% of the nameplate capacity (because the nameplate capacity is based upon standard test conditions that are inferior to conditions in some of the climates over the globe). After the power was estimated at each location and each time step, a post-processing derate factor of 5% was applied to estimate down-times. The resulting solar PV power dataset is temporally and spatially aligned to the wind power dataset outlined above.

1.2 Spatial Availability for Wind and Solar Plants

The deployment of wind and solar plants can be restricted for numerous reasons; including physical, ecological, and proximity to high population areas. To account for these potential restrictions, we eliminated grid cells from wind and solar plant development based on several factors discussed below.

First, national forest lands were excluded based on land-use types obtained from the University of New Hampshire EOS-Webster Earth Science Information Partner catalogue (`http://eos-earthdata.sr.unh.edu/resources/teachers.jsp`). Next, the elevation data from the 3-km NOAA High-Resolution Rapid Refresh (HRRR) model were used to determine the slope of the land within each RUC grid cell. An algorithm determined the slope between each HRRR grid cell and its eight neighbors. The lines over which the slope is computed define the edges of triangular areas - whose slope is set to the greatest of the two edges. The area below the threshold slope is calculated, summed, and assigned to the corresponding RUC grid cells by overlaying the two grids. Considering the spatial resolution of the slope calculations (3 km), the slope constraints are set at 2.5% for utility-scale PV and 10% for onshore wind compared with 5% and 20%, respectively, provided by NREL (*54*). If a RUC cell is given a slope value over these thresholds, no wind and/or solar PV can be developed. The slope constraints are included because increasing slope makes installation much more expensive, dangerous, and possibly lowers the available resource.

The 3-km HRRR grid was also used for the purpose of identifying and eliminating areas (over land) that contain urban or protected land areas. The elimination procedure removed areas such as state and national parks, recreation areas, military bases, airports, and residential, commercial, and industrial lands. The land area still available, after screening, within the HRRR grid cells was summed and assigned to the corresponding RUC grid cells. Population data from the Socioeconomic Data and Applications Center at 0.5° resolution was interpolated to the RUC grid (*55*). After the interpolation, an area of ≈5,383 m^2 ($1\frac{1}{3}$ acres) per capita within each RUC cell was excluded for wind and solar PV deployment to provide a buffer around populated areas. The purpose of the exclusion perimeter is to ensure that wind turbines and solar PV plants are not constructed in close proximity to populated areas (if the population of an average RUC cell is greater than about 39,500 then the RUC cell is totally excluded due to population). In addition, the (10-km x 10-km resolution) Solar Prospector Map Service (*56*) was employed to eliminate RUC grid

cells that overlapped flora and fauna critical habitats. These critical habitats are only catalogued over the southwestern quadrant of the US, thus any other critical habitats across the remainder of the US are not designated as such in the present study.

A limitation was imposed to restrict the deployment of offshore wind turbines to water depths of less than 50 m (*57*) using bathymetry data from the National Geophysical Data Center (*58*) for the East, West, and Gulf Coasts and for the Great Lakes. In addition, offshore turbine locations had to be greater than 13.5 km and less than 46 km from the shoreline. The distance limitation leaves at least one RUC grid cell between the shore and the closest offshore wind turbine. The limits are based upon current requirements for planned and installed offshore wind farms in the US and Europe (*59, 60*). Lastly, the center points of all the offshore RUC grid cells were plotted on top of the Marine Cadastre Multipurpose dataset (*61*), and RUC grid cells that overlapped with the following usage designation were eliminated: shipping fairways, lanes, and zones; danger zones and restricted areas; critical habitat areas; or habitat areas of particular concern. The marine layers were not used to exclude any on-land RUC grid cells. More specifically, there are areas in Maine that are labeled as critical habitats, but because wind farms already exist there, these areas have not been excluded.

On completion of the screening procedures there remained 36,791 (of $\sim$152,000 possible) RUC grid cells available in the model that could support some amount of wind and/or solar PV power generation development. A minimum spacing of ten rotor diameters between each turbine is maintained in all directions (*62*), in an attempt to compensate for potential wind turbine - turbine interactions. The maximum allowed density of possible onshore wind turbine installations is one turbine per 1.2544 km^2 [using the 10 rotor diameter spacing requirement] (*63*). The maximum turbine density translates to 2.01 – 3.22 W / m^2. For offshore wind turbines, the maximum allowed turbine density is 5.25 W / m^2. The utility-scale solar PV plants are based on data in the NREL Solar Advisor Model. They are assumed to be comprised entirely of SunPower SPR-315E-WHT panels, which leads to an area of 258,840 m^2 (approximately 0.26 km^2) per 20-MW plant. The dimensions for the wind and solar PV installations allows computation of the number of turbines and solar PV plants that can be installed within each RUC grid cell given the remaining area with suitable slope. In Fig. (3), the spatial availability for wind and solar deployment is shown. The plots show the density (MW km^{-2}) that can be developed for each technology in each RUC grid cell. Note that the solar spatial availability density is higher than for the wind. To find the approximate total possible installed capacity in each RUC cell multiply the density by 212 km^2 (the average size of a RUC grid cell).

1.3 Electric Demand or Load

The present study utilizes spatially and temporally detailed electricity demand over the US 48 states. Hourly electricity demand, or electric load, was obtained from FERC via form 714 for balancing area authorities (BAAs) and some individual utilities for the years 2006–2008 (*64*). Each BAAs electric load was population-weighted to the major metropolitan areas based on population data from the 2010 Census to create geographic electric sink points. The assignment of the electric load was a complicated procedure because the BAAs and utilities are in constant flux. For example, in 2006 there was no load data provided for the Public Service Company of Colorado balancing authority, but load was available for the Platte River Power Authority, which falls within that balancing authority. Platte River Power Authority does not account for the

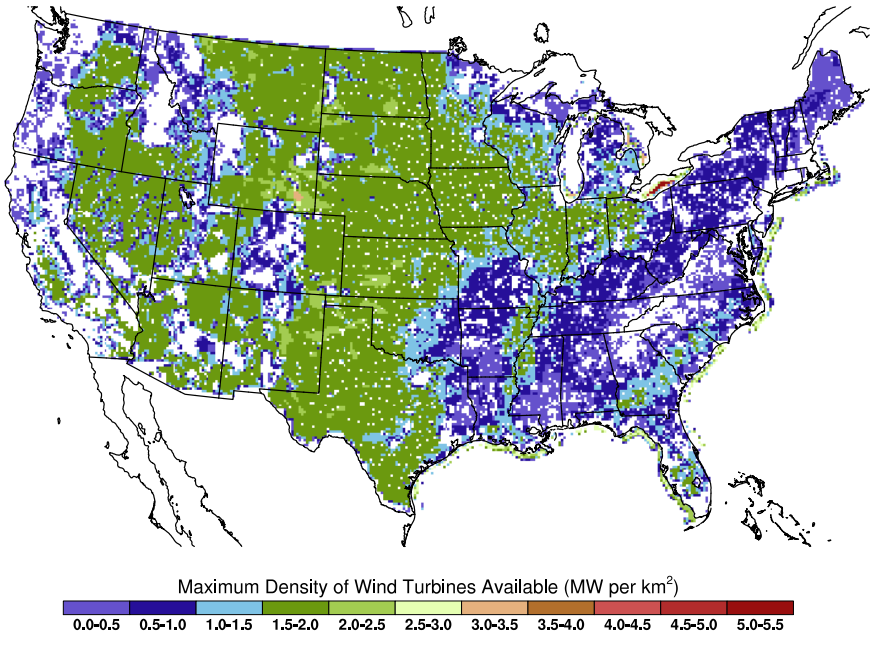

Figure 3: Map of the wind (top) and solar PV (bottom) maximum installed capacity density allowed (MW per km^2). White denotes the region is excluded from having any wind or solar placed within that area.

entire load within the Public Service Company of Colorado balancing authority, but was used as an estimate from which an extrapolation was made. Additionally, for 2007 and 2008, no data was provided for

Southern Company balancing authority, however, load for the four subsidiary companies (Georgia Power, Alabama Power, Mississippi Power, and Gulf Power) was provided instead. Electric load data from each BAA was corrected to standard time from daylight savings time where necessary and shifted to Coordinated Universal Time (UTC). The calculated electric load data for each year was verified against the EIA dataset for the total yearly consumption of electricity in the US.

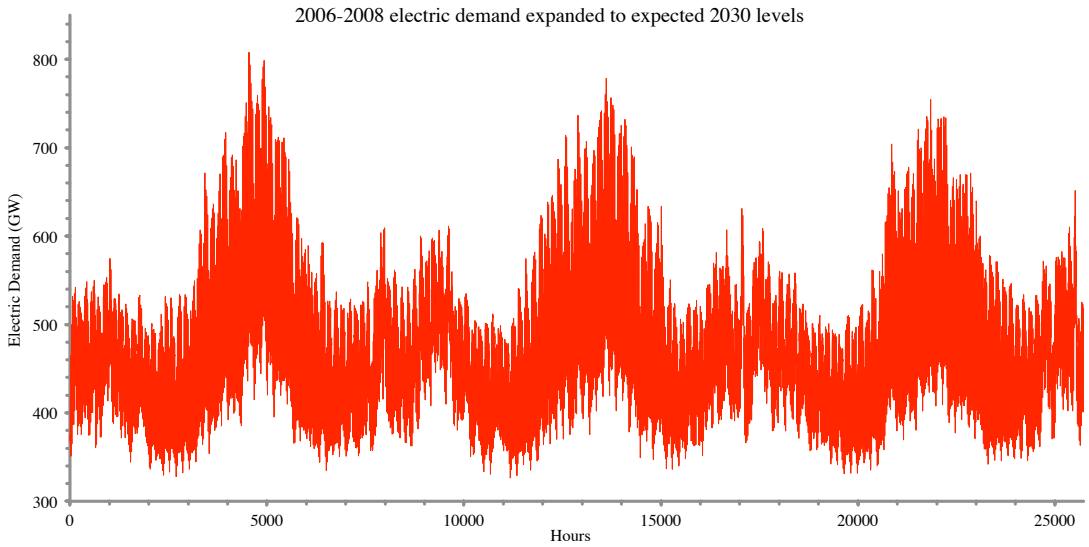

Figure 4: The aggregated US 48 states hourly electric load for 2006–2008 expanded to 2030 levels. The higher peaks are the summers which are dominated by air conditioning demand.

We assumed that all existing (as of 2012) nuclear plants and conventional hydroelectric dams would continue to run through 2030. Although not typically done, we allowed some restricted dispatch ability for nuclear and hydroelectric (described in subsection 1.6) about set values that are computed below. Nuclear power plants *can* alter their output to follow the electric load, although this is not standard procedure in the US. Currently, however, in France they do regularly as 77% of their electricity is provided by nuclear (*65,66*). We recognize that conventional hydroelectric (hydro) generation can be dispatched to match the load, but that characteristic is not taken into account in the present study because the amount of water released from behind dams is also subject to numerous constraints such as flood control, fish habitats, and recreational use (*67*). All of the nuclear fission and hydroelectric power plants in the US were identified and placed into their correct geographic locations within the RUC grid space (*68, 69*). For the nuclear power output, the average capacity and minimum monthly generation for each plant was determined over nine years of data (2003–2011) (*70*). The minima were then divided by the number of hours in each month to calculate the generation value for each hour in each month to ensure that the nuclear generation estimate was conservative. For the hydroelectric power output, we took the actual electricity produced per month for the three years (*71*) and computed the hourly figures from these in a similar manner to the nuclear output. We choose not to dispatch hydroelectric significantly to balance the load because we do not model the hydrological cycle. We, therefore, must constrain the hydroelectric to its meteorological years and not assume that it can be dispatched, as we have no information in the model with regards to water availability.

Further, we do not have solid information and data on the environmental constraints on hydroelectric with respect to, e.g. fish, flood control, recreation or irrigation. Ramping hydroelectric is a possible cheap option to increase the penetration of variable generation, but it is subject to complicated constraints that must be taken into account. Figure 5(a) displays the hydroelectric power output values used for each of the three years and Fig. 5(b) shows the values used for the nuclear power output. These values allow the optimization to take into account the monthly variations in the hydroelectric and nuclear output that is due to the hydrological cycle and maintenance scheduling.

The electric load data was expanded from 2006–2008 to 2030 estimated levels. To estimate the 2030 load, quarterly gross domestic product figures from the Bureau of Economic Analysis (*72*) were applied to the expansion (and contraction) of the load to 2011, and then a 0.7% per year growth rate (*73*) was applied to 2030. The result is a 14% increase in the demand for each hour. Figure 4 shows the total hourly electric load inflated to expected 2030 levels for the three years of 2006–2008.

1.4 Treatment of Costs

Critical variables in the study of electric power systems are the costs of technologies, fuel, and transmission. The weather data, discussed in subsection 1.1, although absolutely essential to the mathematical optimization (explained in section 1.6) is the same for every cost scenario.

Since any construction effort approaching the scale of deployment described in the present study would take years (even decades) to accomplish, a reference date of 2030 was chosen. Selecting a reference date confines the costs (and electric load) available for the studies to projections. Clearly, forecasting future costs is subject to uncertainty. Indeed, the vast available literature provides a considerable range of current and projected costs for all generation types. Consequently, the present investigation relied on multiple cost surveys and studies (*74–85*) in order to populate a parameter space for each of the cost inputs, which produces several cost scenarios for the optimization procedure.

Due to the large amount of data and endogenous variables in the optimization procedure (set out in section 1.6) each optimization is computationally intensive and can take up to hundreds of single-core computing hours to complete. While a fine-grained set of solutions, capturing a broad space of price inputs, is desirable, it may not be computationally feasible. To find a balance between capturing the breadth of the cost parameter space and the computational resources available, three basic generation cost scenarios were devised: first, a Low-cost Renewable High-cost natural Gas LRHG scenario, second a Mid-cost Renewable Mid-cost natural Gas MRMG scenario, and third, High-cost Renewable Low-cost natural Gas HRLG scenario. The intent of the three scenarios is to create effective bounds for the cost parameter space while also providing one representative case.

There are a number of assumptions and methods applied in regards to the costs used in the present study. First, all of the cost figures are given in constant 2013 US Dollars (2013$). For sources that reported costs not in 2013$, the Bureau of Labor and Statistics Consumer Price Index (CPI-U) was used to convert those values into 2013$ (*86*). Second, current tax policies (State or Federal) are not taken into account (such as tax deductions available to businesses). Third, no adjustments were made to the costs obtained from the studies (for example, to address potential carbon tax, cap and trade, penalties, incentives, or policies designed to internalize the externalities of fossil fuel power generation). Fourth,

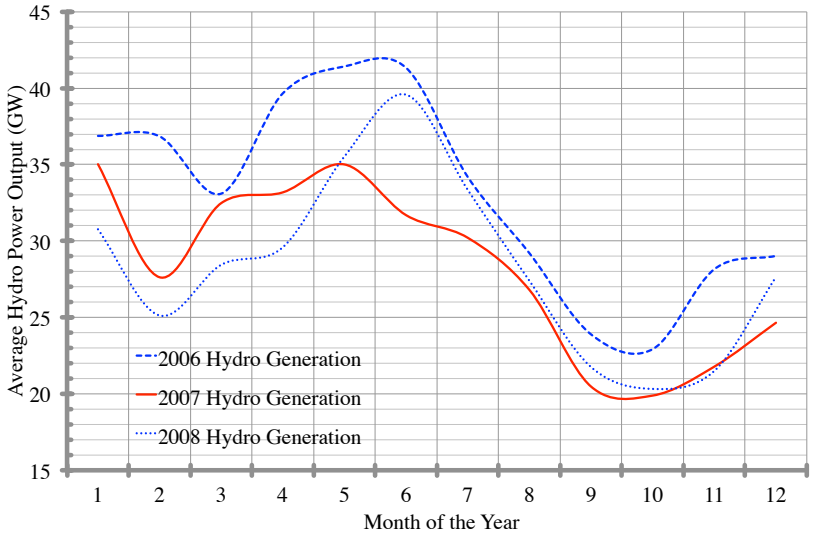

(a) Hydroelectric

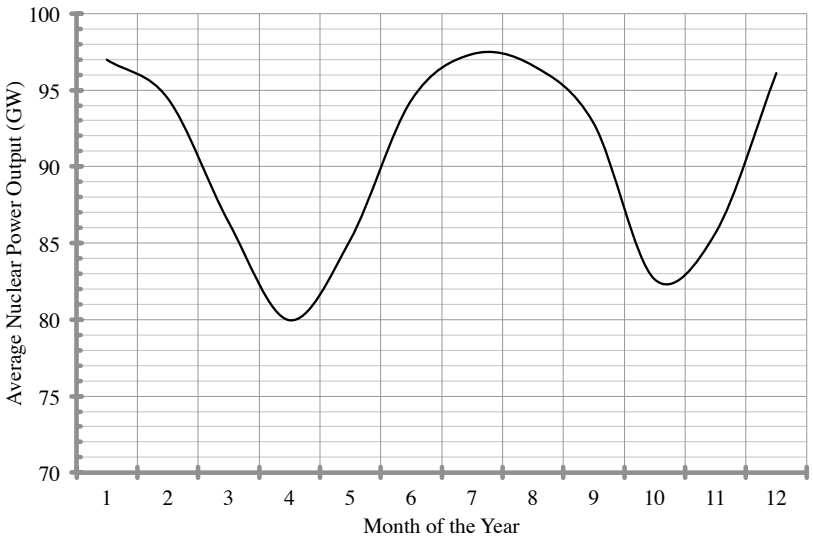

(b) Nuclear

Figure 5: (a) The hourly average combined hydroelectric power output in GW for each month for input into the optimization. Each of the three data years are represented. (b) The hourly average combined nuclear power output in GW for each month. The nuclear values are produced by finding the minimum average over nine years of data. The utilization of these values in the optimization facilitates some inclusion of monthly variations in the hydrologic and maintenance cycles for hydroelectric and nuclear power plants.

costs for generation and transmission are uniform with respect to geography, i.e. the unit costs are not adjusted depending on locality-based factors such as terrain, proximity to roads, railways, or urban areas. Fifth, a fixed real-dollar discount rate of 6.6% (*87*) was applied over the project lifetime, assumed to be 30 years, for each of the scenarios. Currently, there are solar PV manufacturers that will guarantee their

modules for 30 years (*88–90*), and there are efforts underway to extend the service life for wind to 25–40 years (*91, 92*). In addition, it should be noted that for the same amortized payment, the discount rate and project lifetime are a function of each other. Thus, a 15-year project lifetime with a real discount rate of $\sim$1.925%, or a 20-year project lifetime with a real discount rate of $\sim$4.555%, or a 25-year project lifetime with a real discount rate of $\sim$5.875%, or a 30-year project lifetime with a real discount rate of 6.6% have identical amortized payment used in the present paper. Finally, generation and transmission costs "to the substation" are accounted for; local distribution costs are not explicitly modeled, but are accounted for in the final estimated cost of electricity. These distribution costs are independent of generation mix within the electric power system.

To account for curtailment, capacity factors, sunk costs (unrecoverable capital investment), and other factors, the mathematical optimization utilizes an annual cost-per-unit generation capacity for each generating unit. Since there is no fuel cost for the wind and solar PV projects, the total cost per project can be separated into capital costs and Operations and Maintenance (O&M) costs. There are two types of O&M costs, fixed and variable. Fixed O&M costs are based upon the generation capacity, while variable O&M costs are based upon the amount of electricity delivered by the generator. The natural gas plants, however, have capital, O&M, and fuel costs to consider. For natural gas, the fixed O&M costs and amortized capital costs are combined into a single cost per year, while for the wind and solar generators the fixed and variable O&M costs are combined with the amortized capital costs; we do not do this explicitly, these are derived in the reviewed material for the costs. There are numerous ranges for these costs within the literature. Additionally, the variable O&M costs for wind and solar are typically over an order of magnitude smaller than the capital and fixed O&M costs.

A review of the literature for capital costs was carried out (*74–85*). The capital and O&M costs selected for the present study are displayed in Fig. 6 and Table 3. The plot shows the projected 2030 capital and O&M costs in 2013$ per watt installed. The most recent citable current cost is taken to be the high cost for each technology, while the low-cost estimate is based upon the optimistic costs in the studies reviewed. The mid-range values are the mean of the high and low prices.

Table 3: Cost of capital and O&M of technologies (2013$ / W), natural gas fuel (2013$ / MMBtu), HVDC transmission line (2013$ / MW-mile), and HVDC stations (2013$ / MW).

	Onshore	Offshore	PV	CCGT	NG Fuel	HVDC lines	HVDC Stations
LRHG Scenario	$2.16	$3.41	$1.19	$1.24	$11.10	$701.36	$182,856.11
MRMG Scenario	$2.25	$5.53	$2.57	$1.24	$8.82	$701.36	$182,856.11
HRLG Scenario	$2.36	$7.64	$3.94	$1.24	$5.40	$701.36	$182,856.11

Natural gas power plants are a more mature technology. Therefore, we only used a single cost for the natural gas power plants in all three of the cost scenarios (capital and fixed O&M), namely $1.24 / W. However, since natural gas prices have fluctuated wildly in the past, we take three cases from the Annual Energy Outlook (*74*) as our low-, mid-, and high- natural gas fuel costs. A representative fuel cost to cover the assumed 30-year service life of the natural gas plants was desired. The AEO projections for the natural gas fuel cost ended at the year 2040, hence that price was used in lieu of 2045. The three prices are shown in Table 3 and in Fig. 7 in 2013$ / MMBtu. Note that the cost of natural gas fuel is for delivery to the plant, not the well or hub price. Other key factors affecting the cost of natural gas generation are the heat

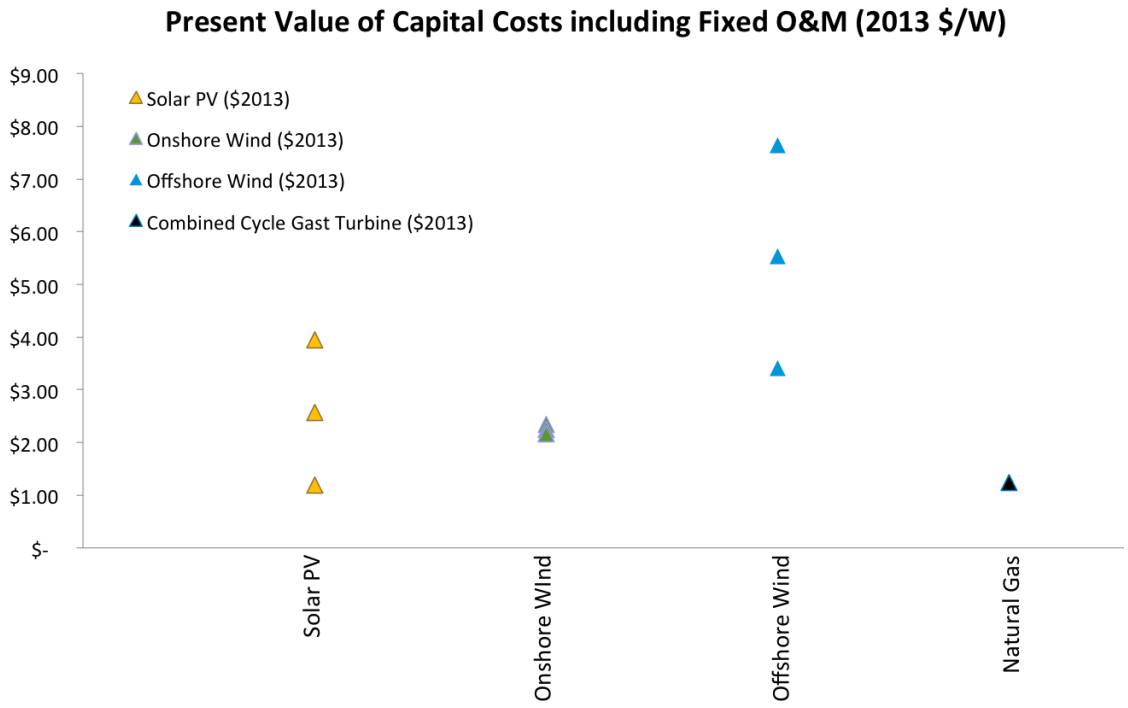

Figure 6: The projected 2030 overnight capital costs including O&M in 2013$.

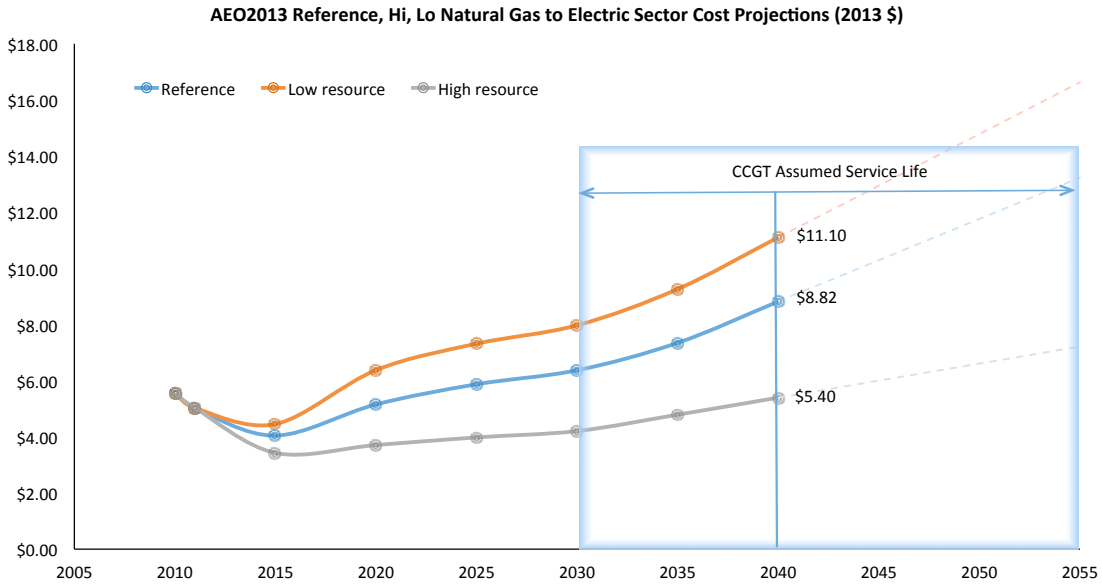

Figure 7: The EIA natural gas projections in 2013$ / MMBtu to 2040 and then extrapolated up to 2055.

rate (measure of efficiency of the plant), and cost of variable O&M. To limit the degrees of freedom in the present studies, these values were kept constant across the scenarios run. The values used were 6.430

MMBtu / MWh for the heat rate and $3.31 / MWh for the variable O&M (2013$) (*84, 85*).

The final key cost is that of high-voltage transmission. The handling of transmission includes the cost of erecting new HVDC lines, building new converter stations, and the power losses incurred as a result of moving power long distances (line losses). The high-voltage transmission is modeled as High-Voltage Direct-Current (HVDC) and so the costs used are associated with HVDC. To limit the degrees of freedom further, we used one set of HVDC costs for all scenarios. The transmission cost was created from an average of current estimates for HVDC transmission construction (*93, 94*). In an attempt to be conservative, the average price of transmission incurred an additional 5% cost increase to account for O&M. The HVDC transmission line cost was set at $701.36 / MW-mile and the station cost was held at $182,856.11 / MW. The HDVC transmission costs (lines and stations) are held constant between the cost scenarios, but it is important to point out that the cost per MW-mile is highly dependent on the length of the transmission lines (*93, 94*), as illustrated in Fig. 8. The total cost (the lines and the stations) per MW-mile is incorporated into the optimization model and so longer lines pay less per MW-mile and shorter ones pay more.

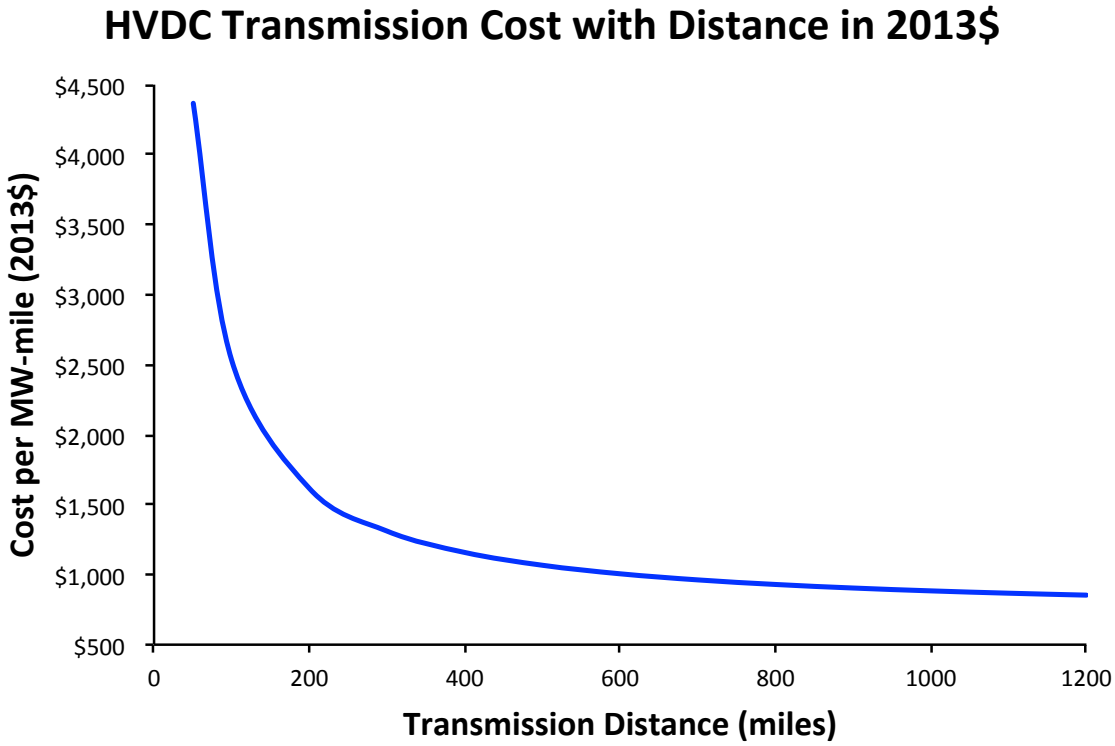

Figure 8: The cost of HVDC transmission (including lines and transformer stations) per MW-mile as a function of distance.

In keeping with the general methodology of the study, we chose not to model a technology that is not currently in operational use. At the time of the main simulation runs, a literature review showed that ∼99% of US grid storage was pumped hydroelectric. The estimated capital costs of a new pumped hydroelectric power plant ranged from $1.50 to $5.60 / W (*84*). When using these costs as inputs, the optimization model did not select any storage in the national solutions. It should be noted that we did not conduct model runs

for the smaller subdivisions as the storage element significantly lengthened the amount of time required to run a scenario.

Storage technologies and costs are in a period of rapid transition, and so more recently we performed additional simulations that included storage with $0.75 / W overnight capital costs, zero cost for electricity storage (i.e. $0 / kWh storage capacity), and zero fixed and variable O&M costs. Additionally, the round trip efficiency was set at 95%. In those simulations, only $\sim$16 GW of storage was selected (with a energy storage capacity of $\sim$208 GWh). In comparison, the total installed pumped hydroelectric storage in the US is $\sim$22 GW (*27*). Therefore, we believe it is reasonable to not include storage in the simulations as even at low cost it contributes minimally to the national solution.

We note that energy storage could have interesting possibilities if the costs are low enough, and we plan to conduct more work in the future (taking advantage of the NEWS model) to investigate the potential of these emerging technologies.

1.5 Transmission, Nodes, and Divisions

A key aspect of electric power systems is transmission, and we describe below how transmission is modeled in this study. Of particular importance are the concepts of nodal areas, nodes, regional market areas, and divisions (as illustrated in Fig. 10). A *division* is a subset of the full contiguous US that is completely independent of other divisions and is solved as a separate electric power system. No information or power transfer is allowed between divisions. A *nodal area* is a subset of a division, but is connected to other nodal areas within the division by *transmission*. Therefore, nodal areas are the building blocks of divisions. The NEWS model has a total of 256 nodal areas. In the limit of the largest number of divisions per domain, there is one nodal area per division. Within each nodal area the city with the largest population acts as the electric power sink (node) where all the demand for that nodal area resides. We iteratively divided the contiguous US from a single division into divisions of 2, 4, 8, 16, 32, 64, 128, and 256. Smaller divisions were made by repeatedly splitting the previous divisions in half (in terms of land area) vertically, then horizontally.

A critical set of nodal areas, called *regional market areas*, reside within the divisions and are connected by HVDC transmission that includes electric losses. The regional market areas consist of eight nodal areas connected by High-Voltage Alternating-Current (HVAC) transmission (see panel (d) in Fig. 10) with electric losses of 1% per 100 miles and is preprocessed. The preprocessing calculates the losses to transmit the power from the resource sites to the electric load sinks (nodes) of the regional market areas. The size of regional markets was chosen to balance the computational constraints in performing an optimization of this size and the steady state stability limit of HVAC transmission. The line arcs of the HVDC transmission network that is available for the optimization to choose to build is shown in Fig. 9. The HVDC transmission has electrical losses of 0.5% per 100 miles (*93,94*). We assumed the distances to be great circle distances, so that the transmission takes the shortest possible route between nodes. Since eight nodal areas create a regional market area, these regional market areas can only exist if there are less than 32 divisions; for 32 or more divisions only HVAC transmission is allowed. The largest city within the eight nodal areas is assigned the connection point for that regional market area to the HVDC transmission network. HVDC exists only to connect Regional Market Areas; no HVDC transmission occurs on scales smaller than the RMAs.

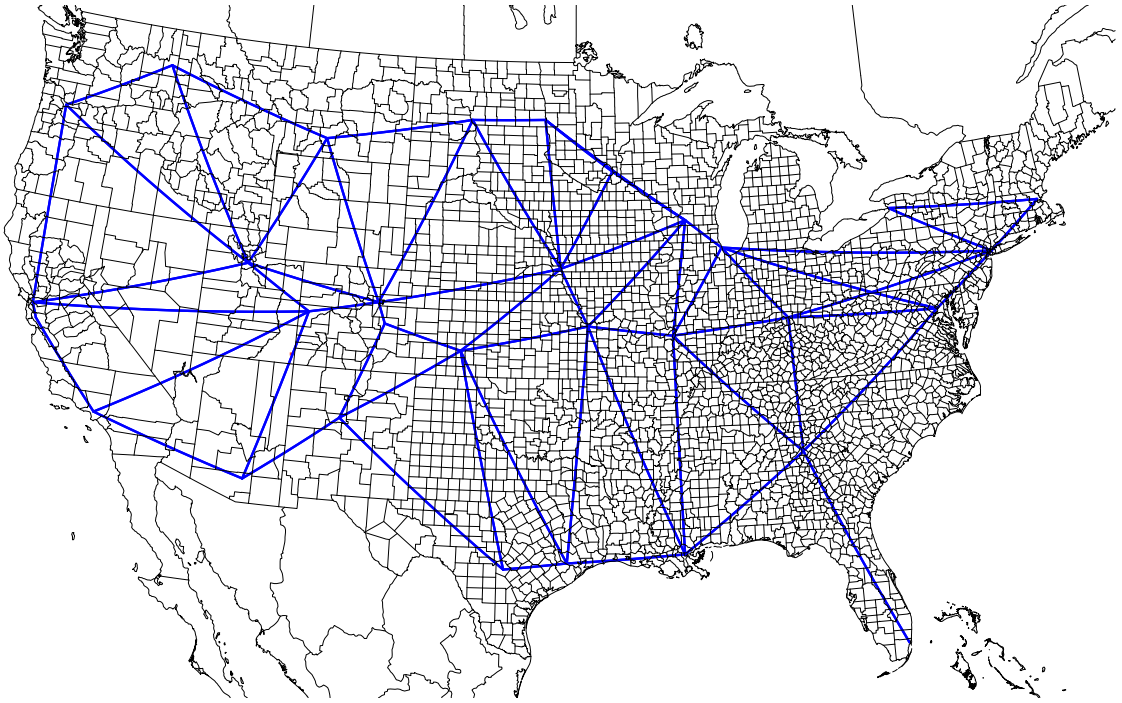

Figure 9: The HVDC transmission network that is available for the optimization to choose to build during the siting of resources. County boundaries are also shown. The end of the HVDC transmission lines are the nodes of the regional market areas.

HVDC use is increasing rapidly around the world with growing capacity. A few of the largest transmission projects around the world are: the Rio Madeira transmission link that was completed in 2014 is 2,385 km long and has a capacity of 7.1 GW (*95*); the North East Agra project is under construction, due to be completed in 2015, and is planned to be 1,728 km in length with a capacity of 8 GW (*96*); and the Hami-Zhengzhou link in China at a length of 2,210 km and a capacity of 8 GW (*97*) completed construction in late 2014. In 1967, it was shown that the limit in HVDC transmission (under superconducting conditions) is 100 GW (*98*); however, the technology is not able to get close to this limit yet. To limit the study to present day technologies, we assumed that the HVDC transmission lines have a maximum possible capacity of 12 GW (*99*). The 12-GW capacity can be considered as two parallel 6-GW lines (many of these exist currently) or a single 12-GW line (at the limits of current technology).

Figure 10 illustrates the concepts of divisions, regional market areas, and nodal areas. Note that the HVDC transmission network within the model is considered to be an approximation to account for costs of power flow across electric power systems rather than an exact representation of possible HVDC transmission networks.

1.6 Mathematical Formulation of the Optimization

The previous subsections (1.1–1.5) have described how the inputs for a mathematical optimization model were found. The present subsection is devoted to explaining the derivation of the optimization model itself.

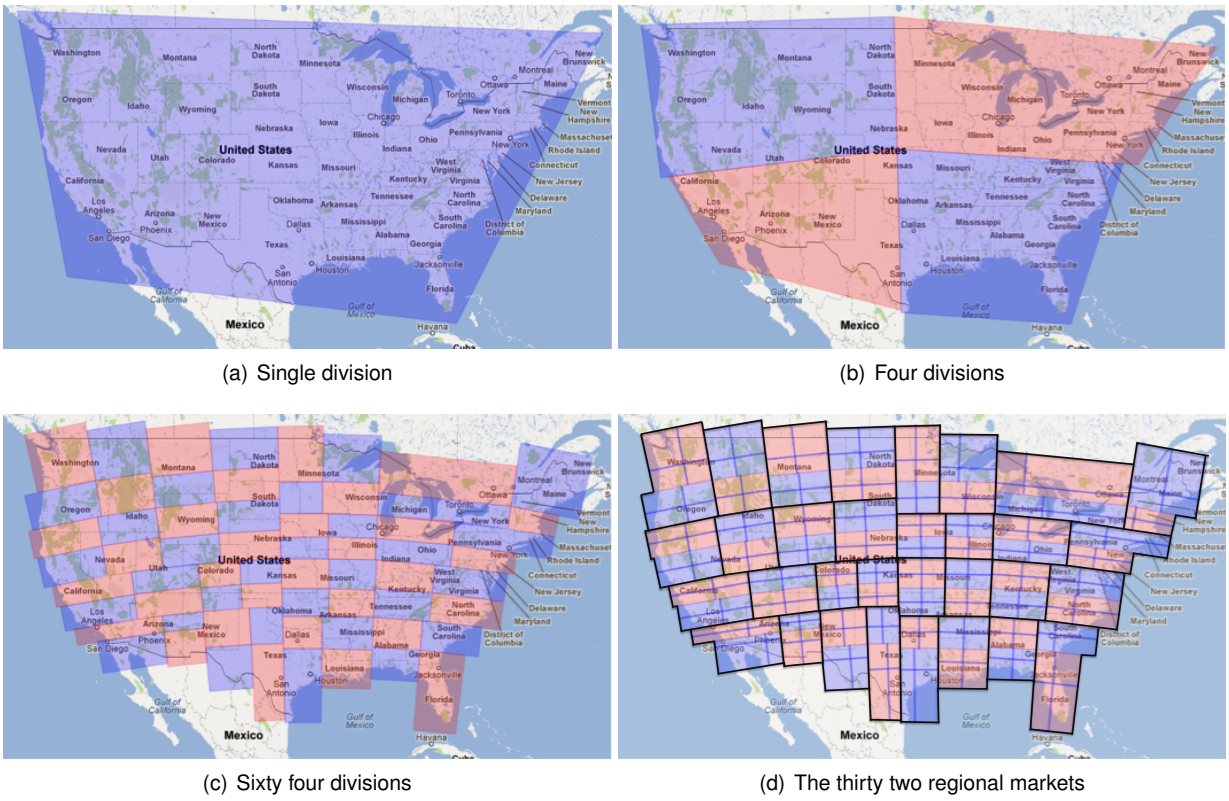

(a) Single division

(b) Four divisions

(c) Sixty four divisions

(d) The thirty two regional markets

Figure 10: Examples of the divisions, regional market areas and nodal areas utilized by the optimization. (a) A single division for the full contiguous US, that will consist of 32 regional market areas each containing eight nodal areas as represented by the black outlines in (d). (b) Four divisions defining four separate electric power systems for the contiguous US. Each division will contain eight regional market areas each containing eight nodal areas. (c) Sixty four divisions representing the contiguous US being made of 64 independent electric power systems. There are no regional market areas (because there are more than 32 divisions) and each division contains only four nodal areas. (d) The 32 regional market areas that contain eight nodal areas each can be connected by HVDC within divisions. Nodes are the largest populated urban areas within each nodal area.

It will draw together all the inputs (or exogenous variables) to be used within the model. More details on the mathematics of the optimization can be found in Clack *et al.*(*22*).

Various mathematical optimizations could be used to produce an *optimal* electric power system that includes large numbers of wind and solar PV power plants. The most appropriate one is chosen based upon what is meant by optimal. For example, if an optimal system is one that builds a set number of wind and solar PV sites and minimizes the total distance from the existing transmission system for all of those sites, then an ordinary least-squares (OLS) procedure (*100–102*) performed on distance could be adopted to locate the best sites. The OLS procedure suggested above is flawed from an electric power system perspective because it does not have the ability to guarantee the electric load is met. One could remedy this deficiency by expanding the model to include a regularization term, as in Regularized Least Squares (*103, 104*), that penalizes the solution for not meeting the electric load. Alternatively, one can

perform an optimization to find a system that generates the required amount of electricity needed in a specific time interval (usually a year). The electricity balance optimization has been carried out, albeit indirectly, by several authors (*105, 106*). The optimal system in the case of electrical electricity balance over a year has the drawback of not meeting the load on shorter temporal scales.

In the authors' opinions the most fundamental challenge for a realistic optimal electric power system with variable generation, such as wind and solar PV, is that the electric load must be met at every time step. One approach to tackle the problem of meeting the load is to perform a quadratic minimization of the differences between the electricity created by an optimal network of wind and solar PV plants and the electric load (*22*) and (*107*). It is then assumed that any shortfall (amount of electricity needed to meet the load after wind and solar PV has been produced) can be filled with a dispatchable source of electricity. The load matching optimization, in its simplest form, can be written as

$$\min \chi^2 = \sum_{\mathrm{j}} \left(\sum_{\mathrm{ik}} c_{\mathrm{ik}} w_{\mathrm{ijk}} - l_{\mathrm{j}} \right)^2 , \tag{13}$$

where c_{ik} is the installed capacity of the wind or solar PV plant, k, at location i, respectively, w_{ijk} is the *weather-driven* percentage output of the wind and solar PV plants at time j and l_{j} is the electric load at time j. The minimization in Eq. (13) will produce a system that is optimal in minimizing the total difference between the variable generation and the electric load, for the given time span optimized on. The mathematical problem outlined in Eq. (13) is another example of an OLS procedure.

Load matching may initially seem like an ideal mathematical technique for an electric power system problem. It takes into account the weather aspect of wind- and solar- generated electricity, and it ensures the load is met on short temporal scales. Unfortunately, there is a major drawback to the load-matching approach. There are no costs within the objective function, which in reality drives all business decisions. The load-matching procedure may provide the smallest divergence from the electric load needed, but the costs may be very high, and therefore the solution is purely academic. Clack *et al.*(*22*) showed that the a system produced by load matching versus cost-optimized can cost twice as much.

The mathematical optimization chosen for the current paper is a cost minimization that has linear constraints with regards to the electric load requirements, the transmission and losses encountered, the facilities required to be built, and the land use allowed for wind and solar technologies. The cost optimization is linear and finds an optimal system with regards to minimum yearly cost only. As stated in previous subsections, there is no attempt to model sociopolitical, grid integration or other costs (such as public objections, legal issues, distribution of power from the local substation, and so on). We recognize that not including the aforementioned costs is a limitation to the present study, however, we are attempting to establish the physical and technical limitations that could be used as a baseline optimal state.

The costs set out in subsection 1.4 are the primary exogenous (input or external) variables for the objective function, which is the equation that the algorithm is trying to minimize. We need to incorporate the annual amortized capital and fixed O&M costs for each technology, the natural gas fuel and variable O&M costs, and the capital and fixed O&M costs for transmission lines and for the transformer stations.

Thus, mathematically, the objective function appears as

$$\text{Minimize} \quad \psi = \sum_{\phi}\sum_{\kappa} \mathcal{C}^{v}_{\phi\kappa} \cdot V_{\phi\kappa} + \sum_{\mu}\left(\mathcal{C}^{g}_{\mu} \cdot G_{\mu} + \left(\mathcal{E}^{f}_{\mu} \cdot \mathcal{C}^{f}_{\mu} + \mathcal{V}^{f}_{\mu}\right) \cdot \sum_{\tau} D_{\mu\tau}\right) + \sum_{\hat{\alpha}}\sum_{\hat{\beta}} T_{\hat{\alpha}\hat{\beta}} \cdot \left(\mathcal{C}^{ts}_{\hat{\alpha}\hat{\beta}} + \mathcal{C}^{tl}_{\hat{\alpha}\hat{\beta}} \cdot \delta_{\hat{\alpha}\hat{\beta}}\right). \quad (14)$$

Here $\mathcal{C}^{v}_{\phi\kappa}$ represents the annual amortized capital and O&M costs (2013$ / W) of the variable generator of type κ at location ϕ, $\mathcal{C}^{g}_{\mu}$ is the capital and fixed O&M costs of the fossil fuel generators at location μ (2013$ / W), $\mathcal{C}^{tl}_{\hat{\alpha}\hat{\beta}}$ is the cost of each HVDC transmission line between $\hat{\alpha}$ and $\hat{\beta}$ (2013$ / MW-mile), $\mathcal{C}^{ts}_{\hat{\alpha}\hat{\beta}}$ is the cost of each HVDC transformer station pair (2013$ / MW), $\mathcal{E}^{f}_{\mu}$ is the heat rate of the fossil fuel plants (MMBtu / MWh), $\mathcal{C}^{f}_{\mu}$ is the cost of the fossil fuels (2013$ / MMBtu), and $\mathcal{V}^{f}_{\mu}$ is the variable O&M for the fossil fuel plants (2013$ / MWh). Table 3 provides all the costs used in the optimization and inside the algorithm they are converted into annual amortized costs. These are the exogenous variables $\mathcal{C}^{j}_{i}$ written out above. The other exogenous variable is the length of the HVDC transmission lines ($\delta_{\hat{\alpha}\hat{\beta}}$), which is preprocessed by calculating the great circle distances from the single largest cities (electric sink points or nodes) in each of the 32 regional market areas. Figure 9 shows the lines that are calculated. The variables $V_{\phi\kappa}$, G_{μ}, $D_{\mu\tau}$ and $T_{\hat{\alpha}\hat{\beta}}$ are endogenous (output or internal) variables and are computed by the optimization. $V_{\phi\kappa}$ is the installed capacity of the variable generators (MW), G_{μ} is the installed capacity of fossil fuels (MW), $D_{\mu\tau}$ is the amount of electricity coming from fossil fuels (MWh) at each time step τ, and $T_{\hat{\alpha}\hat{\beta}}$ is the capacity of the HVDC transmission lines (MW). All of the optimizations used natural gas as the fossil fuel source, except for the sensitivity to coal analysis that used both coal and natural gas.

Equation (14), the objective function, has of the order of 400,000 endogenous variables. The minimization of Eq. (14) results in a single cost (and the associated values of all the endogenous variables). The trivial solution of the minimization is $0, which corresponds to no generators installed, no natural gas burned, and no transmission built. The constraints set out in the remainder of the present section will act to force the value of ψ to be greater than zero. The competing effects of the constraints and the minimization of the objective function is what makes the site selection important.

The first constraint is the most fundamental: that the electric demand is met on every time step at every location. The electric demand in the optimization is input from subsection 1.3 and it is matched by combining the electric generation from wind, solar PV, natural gas, nuclear, and hydroelectric within each regional market area along with the HVDC transmission power flux and the curtailment of the wind and solar PV due to excess generation. The *load constraint* can be written as

$$\sum_{\phi}\left(b^{v}_{\phi\omega} \cdot \sum_{\kappa} V_{\phi\kappa} \cdot \mathcal{W}_{\phi\kappa\tau}\right) + \sum_{\mu} b^{c}_{\mu\omega} \cdot \left(D_{\mu\tau} + N_{\mu\tau} + H_{\mu\tau}\right) = \mathcal{L}_{\omega\tau} - F_{\omega\tau} + E_{\omega\tau}, \quad \forall\, \omega, \tau. \quad (15)$$

In Eq. (15) the weather data from subsection 1.1 is utilized. It appears in the first term of the left-hand side of the equation as $\mathcal{W}_{\phi\kappa\tau}$. The weather data is in the form of *hourly capacity factors*, which are multiplied by the installed capacity at that location ($V_{\phi\kappa}$) to give the generation at that particular site. The total wind

and solar PV generation is distributed into transmission nodal areas by $b^v_{\phi\omega}$. The subscript ω denotes the regional market area. The variable $b^v_{\phi\omega}$ is less than or equal to unity, and contains the information about the HVAC transmission losses. The second term is the total electric generation from the conventional generators (natural gas ($D_{\mu\tau}$), nuclear ($N_{\mu\tau}$), and hydroelectric ($H_{\mu\tau}$)). Again, the generation is distributed into the transmission nodal areas by $b^c_{\mu\omega}$. The right-hand side of Eq. (15) consists of the electric demand of each regional market area, which was discussed in subsection 1.3 ($\mathcal{L}_{\omega\tau}$), minus the HVDC transmission power flux ($F_{\omega\tau}$), plus the excess of generation or curtailment ($E_{\omega\tau}$). The excess generation term is a *slack* variable to take into account the possibility that generation can be more than the required electric load and transmission combined. The transmission flux term is explained more by the next two constraints. The *load constraint* is performed for every time step within every regional market area; for a one-year period yields ∼280,000 equations.

The following two constraints describe the transmission capacity term in Eq. (14) and the HVDC transmission power flux term from Eq. (15). The HVDC transmission network description inside the optimization is significant. The HVDC transmission allows power to be shared between the regional market areas, but at a cost to the system. The first constraint determines the capacity of the HVDC transmission lines and is called the *HVDC transmission capacity constraint*. The way the optimization handles the capacity of the HVDC transmission appears simple, but sets it apart from other optimization routines available for electric power systems. The *HVDC transmission capacity constraint* determines the capacity of the lines in both directions simultaneously. Other optimizations (*8*, *13*) find the capacity of *each arc* and find the related costs and consequently power flow is restricted to the direction that the transmission arc has been built, whereas the optimization described in the present paper computes the capacity of the *corridor for both arcs*. By performing the *HVDC transmission capacity constraint* in this manner, the optimization can dispatch power in either direction along that corridor once it has been built, rather than being restricted to the direction that was built in the arc form. Computing the capacity of both arcs simultaneously costs significant computational expense, since it doubles the degrees of freedom of the optimization of the network, but reduces the total system costs in a realistic manner. The constraint looks very simple mathematically as

$$\mathcal{T}_{\hat{\alpha}\hat{\beta}} \geq T_{\hat{\alpha}\hat{\beta}} \geq T_{\alpha\beta\tau}|_{\alpha,\beta=\hat{\alpha},\hat{\beta}} \geq 0, \quad \forall\, \hat{\alpha}, \hat{\beta}, \tau\ (\hat{\alpha} > \hat{\beta}). \tag{16}$$

Here $T_{\hat{\alpha}\hat{\beta}}$ is the capacity of the HVDC transmission line, which is passed up to the objective function in Eq. (14). $T_{\alpha\beta\tau}$ is the HVDC transmission power flow matrix found by Eq. (17) shown below. Equation (16) states that the capacity of the transmission line must be greater than the power flow within it at any time. The constraint has an upper bound denoted by $\mathcal{T}_{\hat{\alpha}\hat{\beta}}$, which in the present paper is set uniformly as 12 GW. The constraint in Eq. (16) automatically updates the opposite direction of flow capacity for use at future time steps. The *HVDC transmission capacity constraint* is performed for each transmission node at each time step of the optimization; providing ∼87.6 million equations. The difficulty with Eq. (16) is that to compute both directions simultaneously ,the transmission power matrix must be transposed (a computationally expensive procedure) along with the additional degrees of freedom created by opening a new transmission route for power to flow when a corridor is expanded.

The second HVDC transmission constraint is related to the HVDC transmission power flux, which can be positive, negative, or zero because power can flow in to or out of a regional market area. The flow term balances power, and therefore satisfies Kirchoff's law assuming constant voltage. The HVDC transmission

power flux is the summation of all the electric power entering and leaving a regional market area through its node carried by the HVDC transmission network. If the flux term is positive, the node is known as a *source node*, if it is negative, it is a *sink node*, and if it is zero, it is a *transshipment node*. The HVDC transmission power flow along the HVDC transmission lines is represented in a nonnegative 3-D matrix ($T_{\alpha\beta\tau}$). Hence, the HVDC transmission power flux is derived as

$$F_{\omega\tau} = \sum_{\alpha} T_{\alpha\beta\tau} \cdot (1 - \lambda_{\alpha\beta} \cdot \delta_{\alpha\beta})\Big|_{\beta=\omega} - \sum_{\beta} T_{\alpha\beta\tau}\Big|_{\alpha=\omega}, \quad \forall\, \omega, \tau\ (\alpha \neq \beta), \tag{17}$$

where $\lambda_{\alpha\beta}$ is the electric losses per mile along the transmission line and $\delta_{\alpha\beta}$ is the length of the transmission line. The electric losses are only applied at the receiving node. Equation (17) is the *HVDC transmission flux constraint* and the first term on the right-hand side is the summation of the power matrix multiplied by one minus the electric losses along each line (another matrix) while the second term just totals the transmission power leaving the same node. The summing variables α and β are the heads and tails of the transmission arc. The *HVDC transmission flux constraint* is performed for each of the nodes at each time step of the optimization; for a total of ∼280,000 equations. At each time step the upper triangle of the matrix, $T_{\alpha\beta\tau}$, must equal the lower triangle. The electric losses ($\lambda_{\alpha\beta}$) are set in subsection 1.5.

The optimization already derates the power produced by wind and solar PV ($\mathcal{W}_{\phi\kappa\tau}$) by 5% as described in subsection 1.1. The reduction in power is designed to approximate turbine and panel downtimes as well as interactions between wind turbines. For the fossil fuel portion of the generation, we instead impose the *planning reserve requirement constraint*. The planning reserve requirement controls how much larger the installed capacity must be than the peak power generation on any time step over the time horizon in the optimization. It can be written as

$$\sum_{\mu} b^{c}_{\mu\omega} \cdot G_{\mu} \geq \left(1 + \mathcal{R}^{g}_{\mu}\right) \cdot \sum_{\mu} b^{c}_{\mu\omega} \cdot D_{\mu\tau} \geq 0, \quad \forall\, \omega, \tau, \tag{18}$$

where G_{μ} is the installed capacity of fossil fuels, $D_{\mu\tau}$ is the electricity provided by fossil fuels at each time step, $b^{c}_{\mu\omega}$ is the variable to distribute generation to each regional market area, and $\mathcal{R}^{g}_{\mu}$ is the planning reserve margin (the percentage of additional installed capacity compared to peak demand). Equation (18) states that the installed capacity of the fossil fuel plants within each regional market area must be greater than the generation by fossil fuels at each time step within that same regional market area. The planning reserve requirement constraint is run in every regional market area on every time step; adding another ∼280,000 equations to the optimization algorithm. We could rewrite Eq. (18) such that it states

$$\sum_{\mu} b^{c}_{\mu\omega} \cdot G_{\mu} \geq \left(1 + \mathcal{R}^{g}_{\mu}\right) \cdot \sum_{\mu} b^{c}_{\mu\omega} \cdot \max\left(D_{\mu\tau}\right) \geq 0, \quad \forall\, \omega, \tag{19}$$

which would reduce the number of constraints dramatically. However, Eq. (19) is nonlinear and requires a much more computationally intensive algorithm to solve. Therefore, we adopt Eq. (18) as the constraint within the present optimization. The planning reserve margin is set at 15% in each regional market area.

To allow the optimization the benefit of (very slight) ramping of nuclear and hydroelectric, two constraints were devised. The constraints allow the estimated generation from nuclear and hydroelectric to vary about

the monthly figures described in subsection 1.3, denoted by $\mathcal{N}_{\mu\tau}$ and $\mathcal{H}_{\mu\tau}$ respectively. The two constraints (known as the *nuclear and hydroelectric dispatch constraints*) appear as

$$\mathcal{B}_{\omega}^{n-} \cdot \sum_{\mu} \left(b_{\mu\omega}^{c} \cdot \mathcal{N}_{\mu\tau}\right) \leq \sum_{\mu} b_{\mu\omega}^{c} \cdot N_{\mu\tau} \leq \mathcal{B}_{\omega}^{n+} \cdot \sum_{\mu} \left(b_{\mu\omega}^{c} \cdot \mathcal{N}_{\mu\tau}\right), \quad \forall\, \omega \tag{20}$$

and

$$\mathcal{B}_{\omega}^{h-} \cdot \sum_{\mu} \left(b_{\mu\omega}^{c} \cdot \mathcal{H}_{\mu\tau}\right) \leq \sum_{\mu} b_{\mu\omega}^{c} \cdot H_{\mu\tau} \leq \mathcal{B}_{\omega}^{h+} \cdot \sum_{\mu} \left(b_{\mu\omega}^{c} \cdot \mathcal{H}_{\mu\tau}\right), \quad \forall\, \omega. \tag{21}$$

Here $N_{\mu\tau}$ and $H_{\mu\tau}$ represent the nuclear and hydroelectric generation created by the optimization. The term $b_{\mu\omega}^{c}$ distributes the generation to the appropriate regional market areas. The percentage by which the nuclear and hydroelectric power output can vary from the values described in subsection 1.3 are bounded above by $\mathcal{B}_{\omega}^{n+}$ and $\mathcal{B}_{\omega}^{h+}$, and below by $\mathcal{B}_{\omega}^{n-}$ and $\mathcal{B}_{\omega}^{h-}$, respectively. For the present study,we assumed that the generation values set out in subsection 1.3 are the upper bounds for the generation used by the optimization ($\mathcal{B}_{\omega}^{n+} = \mathcal{B}_{\omega}^{h+} = 100\%$), while the lower bound for the nuclear power output is fixed at 97.5% ($\mathcal{B}_{\omega}^{n-} = 97.5\%$) and the hydroelectric power output is set at 95% ($\mathcal{B}_{\omega}^{h-} = 95\%$). Hydroelectric was allowed more freedom to dispatch than nuclear because it more readily dispatches in the current US electric power system.

It is clear that there cannot be an infinite number of generators at a specific location, however, an optimization routine needs to have a value supplied for it to be able to enforce a constraint of that nature. For wind and solar PV plants, we discussed the process for evaluating the area available for development by the optimization. We state that the values calculated from subsection 1.2 on land use and siting constraints provide an upper bound to the deployment of wind and solar PV, which we denote $\mathcal{B}_{\phi\kappa}^{v+}$. We can then constrain the installed capacity of wind and solar PV ($V_{\phi\kappa}$) by

$$\mathcal{B}_{\phi\kappa}^{v-} \leq V_{\phi\kappa} \leq \mathcal{B}_{\phi\kappa}^{v+}, \quad \forall\, \phi, \kappa. \tag{22}$$

We assume that the existing (2012) wind and solar PV plants remain functional through the optimization period and set the lower bounds for those optimizations. We call Eq. (22) the *wind and solar PV siting constraint*.

Conventional generators also have limits on siting. We found the location of all existing natural gas and coal fired power plants across the continental US and only allowed development of natural gas at those specific sites. We further assumed that no more than 10 GW ($\mathcal{B}_{\mu}^{g}$) could be developed at a single site. The largest natural gas plant in the US as of 2013 is 1.5 GW, while the largest in the world is 5.6 GW. We write the *natural gas siting constraint* as

$$0 \leq G_{\mu} \leq \mathcal{B}_{\mu}^{g}, \quad \forall\, \mu. \tag{23}$$

The US study optimization can be stated as *minimize Eq. (14) subject to Eqs (15), (17), (16), (18), (20), (21), (22), and (23)*. The optimization routine is written and solved using GAMS/CPLEX (*108*). The present study optimizations have $\mathcal{O}(10^7)$ variables, $\mathcal{O}(10^6)$ equations, and $\mathcal{O}(10^8 - 10^9)$ non-zero elements, which take $\mathcal{O}(10^6)$ iterations or $\mathcal{O}(10^5)$ seconds to complete on a dedicated high-performance server. For the geographic scaling portion of the present study we performed 81 optimizations, and for the natural gas price sensitivity portion we carried out another 135 optimizations to investigate the effect on the generator

and transmission network configurations. The optimizations themselves took a total of 15,552 core hours to complete.

2 Supplementary Results

The present section shows supplemental results from our study. The results are complementary to those shown in the main paper by expanding on the analysis. The study focused on investigating the amount of carbon-emission-free electricity generated by an electric power system under different cost scenarios. We define carbon-emission-free electricity to be the percentage of the electric demand met by wind, solar photovoltaics (PV), nuclear, and hydroelectric.

The same optimizations were performed on three separate years of weather and load data; 2006, 2007, and 2008. Each optimization was subject to the hourly resolution weather and load data for the whole year. The solutions varied between different years, but only by small amounts. In fact, each cost-optimized national solution was dispatched with the other two year's weather and load data and we found that no additional back-up capacity was required. However, for the simulations using smaller independent electric power systems (greater number of divisions) the amount of natural gas capacity needed varied depending on the year. The conclusion that the smaller area electric power systems did require extra natural gas plants implies an important feature; that isolated small geographic areas exhibit greater year-to-year variability than a larger encompassing geographic area. This phenomenon could be dealt with by enforcing the smaller geographic area electric power systems to hold higher amounts of reserves - further increasing costs. We focus on the 2007 weather and load data optimizations in this present section. We show all three data years when there is useful information to be displayed, otherwise it can be assumed that the different data years behave in a similar manner to the 2007 data year.

The rest of this section is broken down into three parts. First, we show expanded results on the geographic scaling study. Second, we describe the results of the natural gas fuel cost sensitivity study. Third, we illustrate the impact of coal without carbon capture and sequestration (CCS) on the optimization of a single connected US electric sector.

2.1 Geographic Scaling Study

Geographic scale and cost are two important inputs into the optimized solutions. For our investigation, we performed a total of nine optimizations for each cost (and data year) scenario for 1, 2, 4, 8, 16, 32, 64, 128, and 256 independent electric power systems. Because of the vast amount of possible outputs from the different scenarios computed, we show a selection of the optimized solutions. Figure 11 displays configurations of the cost-optimized electric power system for the Low-cost Renewable High-cost Natural Gas (LRHG) scenarios for four different grid size distributions: a contiguous US electric power sector with one connected system, eight independent systems, 64 independent systems, and 256 independent systems. Figures 12 and 13 show the same information as Fig. 11, but for the Mid-cost Renewables Mid-cost Natural Gas (MRMG) and the High-cost Renewables Low-cost Natural Gas (HRLG), respectively.

Figures 11–13 display the siting of wind, solar photovoltaic (PV), natural gas, nuclear, hydroelectric power plants and HVDC transmission lines by cost-optimizing electric power systems at different geographic scales. In Figure 3 of the main text, we showed wind and solar PV binned at different densities. In these images and all that follow in the supplementary information, we only show locations that have wind or solar PV. We do not bin them because the images are too small to notice the differences. In all three cost scenarios the optimization will construct HVDC transmission lines when it is economically advantageous.

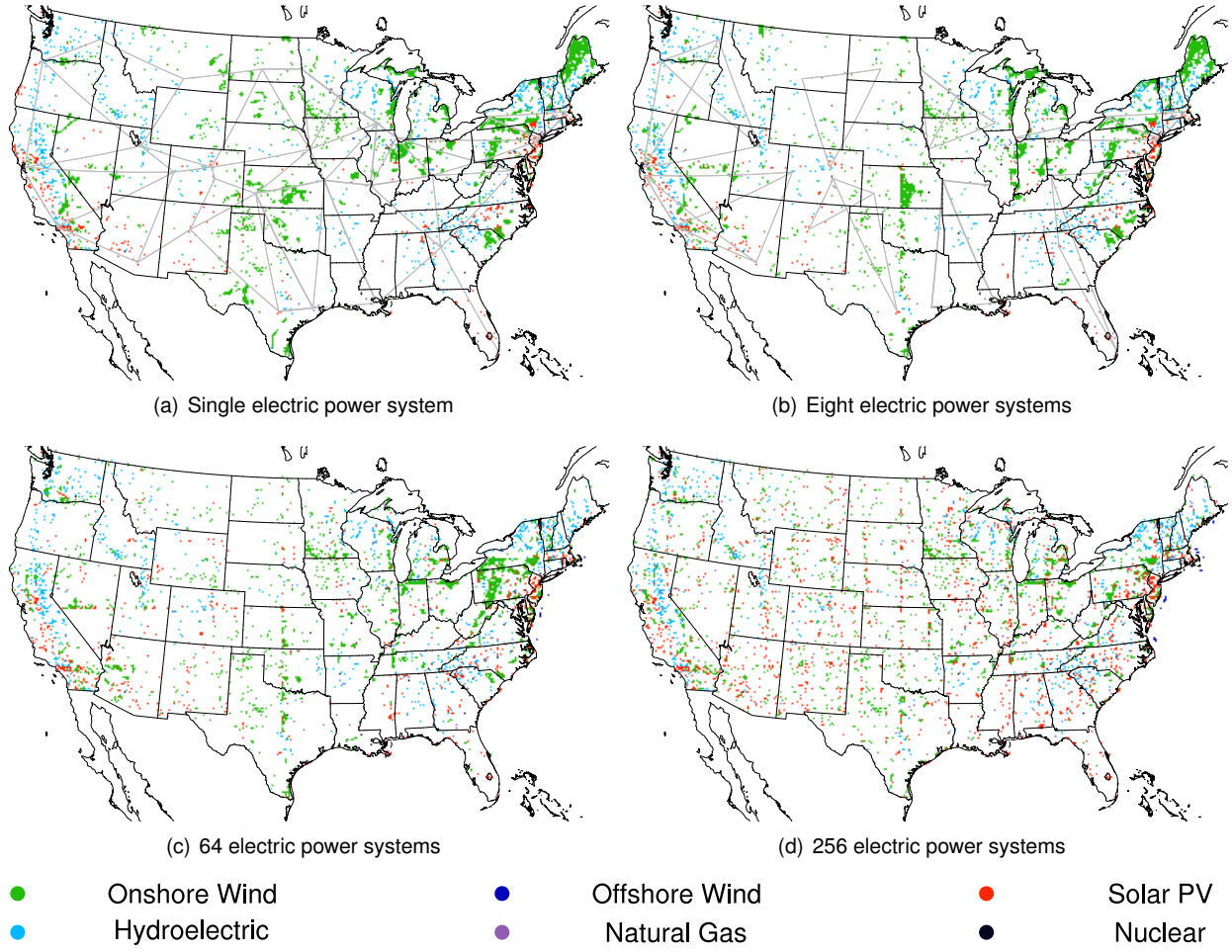

Figure 11: Configurations of cost-optimized contiguous US electric power sectors for the 2007 data year and Low-cost Renewable High-cost Natural Gas (LRHG) scenario. The colored cells represent a technology deployed within that model grid cell. It does not represent the amount that is found in that cell. The colors are shown under the maps. The gray lines represent High Voltage Direct Current (HVDC) transmission lines built by the optimization and the thickness of the line is proportional to the capacity. Only (a) and (b) can contain these HVDC transmission lines. (a) Shows the configuration for a single connected cost-optimized electric power system over the contiguous US. (b) Displays a cost-optimized electric power sector that contains eight independent electric power systems. (c) Is a cost-optimized electric power sector with 64 independent electric power systems. (d) The configuration of a cost-optimized electric power sector with 256 independent electric power systems.

Figures 11–13 show that the configuration of the electric power system is strongly dependent on the projected costs of technologies. For all three cost scenarios the optimization selects different configurations of power plants while retaining the construction of HVDC transmission lines, indicating that the electric power system benefits from HVDC transmission regardless of the constituent power plants. The vertical lines of deployment of wind power plants are explained by the shape of the nodal areas, which are shown in Fig. 10. The nodal areas were selected to have equal land area so that we could determine a functional

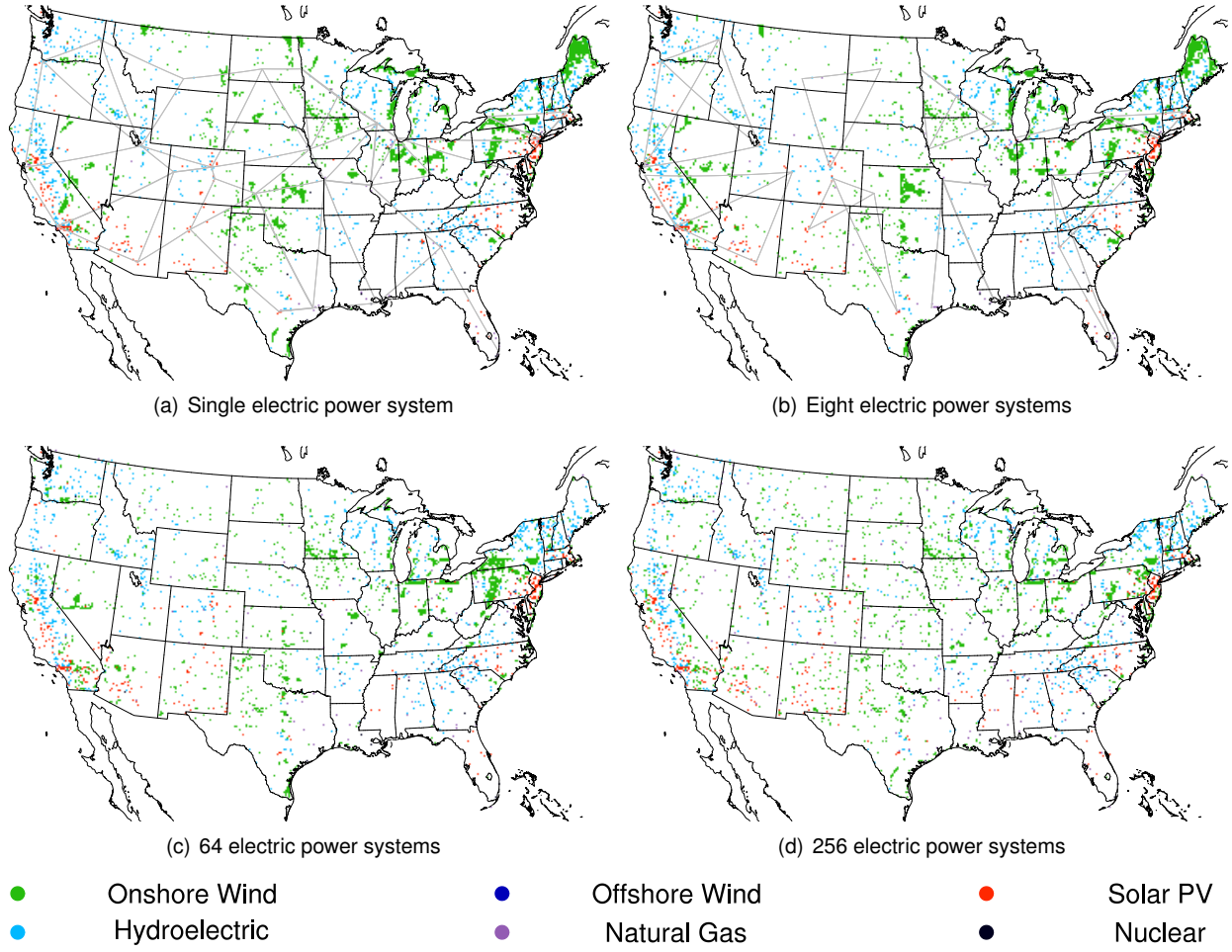

Figure 12: Configurations of cost-optimized contiguous US electric power sectors for the 2007 data year and Mid-cost Renewable Mid-cost Natural Gas (MRMG) scenario. The colored cells represent a technology deployed within that model grid cell. It does not represent the amount that is found in that cell. The colors are shown under the maps. The gray lines represent High Voltage Direct Current (HVDC) transmission lines built by the optimization and the thickness of the line is proportional to the capacity. Only (a) and (b) can contain these HVDC transmission lines. (a) Shows the configuration for a single connected cost-optimized electric power system over the contiguous US. (b) Displays a cost-optimized electric power sector that contains eight independent electric power systems. (c) Is a cost-optimized electric power sector with 64 independent electric power systems. (d) The configuration of a cost-optimized electric power sector with 256 independent electric power systems.

relationship between geographic area and wind and solar deployment. Thus, the lines of deployment are due to the optimization moving the wind plants closest to the high resource while reducing variability. Other shapes and sizes of nodal areas can be used, but the geographic scaling could not be quantified. Indeed, the nodal areas are an input to the NEWS model and can be changed readily if needed.

We observed that the number of wind and solar PV sites selected is lower in Fig. 13 compared with Fig. 11, indicating that without achieving renewable electricity cost goals, wind and solar PV will not be

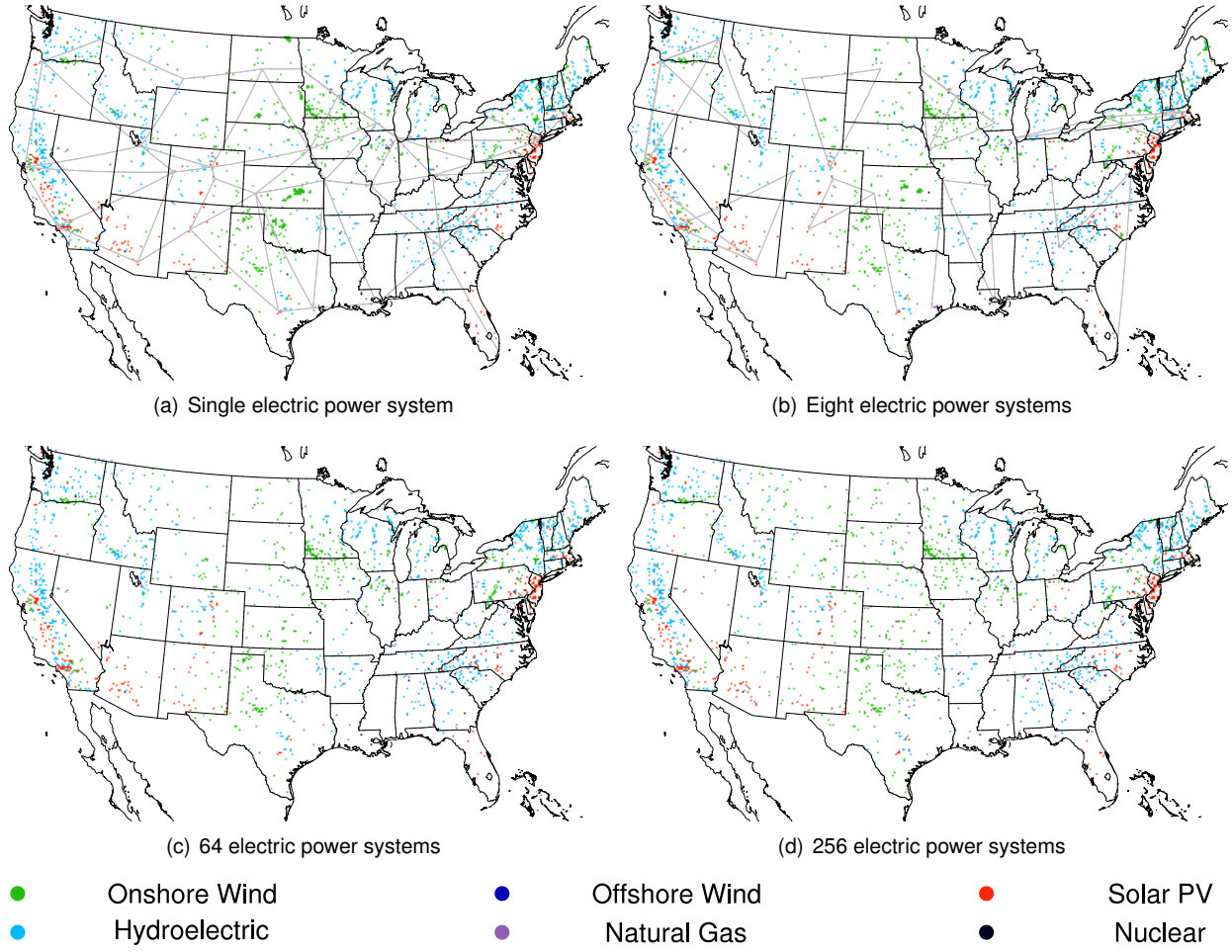

Figure 13: Configurations of cost-optimized contiguous US electric power sectors for the 2007 data year and High-cost Renewable Low-cost Natural Gas (HRLG) scenario. The colored cells represent a technology deployed within that model grid cell. It does not represent the amount that is found in that cell. The colors are shown under the maps. The gray lines represent High Voltage Direct Current (HVDC) transmission lines built by the optimization and the thickness of the line is proportional to the capacity. Only (a) and (b) can contain these HVDC transmission lines. (a) Shows the configuration for a single connected cost-optimized electric power system over the contiguous US. (b) Displays a cost-optimized electric power sector that contains eight independent electric power systems. (c) Is a cost-optimized electric power sector with 64 independent electric power systems. (d) The configuration of a cost-optimized electric power sector with 256 independent electric power systems.

significantly utilized in the production of electricity in the future, considered on an economical basis only. In Figs 11–13, we can also see that with larger geographic areas, or fewer number of independent electric power systems, the wind and solar PV tends to cluster more prevalently around optimal resource locations. Figures 11 to Fig. 13 demonstrate that without a large geographic area, enabled by HVDC transmission, the amount of wind and solar PV that can be economically deployed is reduced due to its variability. An exception to this is when solar PV is very cheap (as it is in the LRHG scenario), in which case the amount

of solar PV will increase slightly with decreasing geographic area because it can compete with natural gas peaking requirements. This result that should be viewed with some caution because the power data resolution is hourly and solar PV power production has zero inertia; hence cloud cover that is sporadic and sub-hourly could cause solar PV power to drop considerably (not captured by the current model), reducing its efficacy over small geographic areas.

Figure 11 shows that offshore wind is only deployed for the LRHG scenario. Further, offshore wind is developed to very small amounts. The deployment increases with increasing system numbers because the East Coast load needs fulfilling, but there is no access to the central plains when the geographic scale is diminished, and so offshore becomes economically favorable. This indicates that offshore wind will result in increased total annual cost compared with HVDC transmission and central plains wind power production.

For each scenario, the installed capacity of nuclear and hydroelectric power plants remains constant at 100.4 GW and 74.4 GW, respectively. Further, they are located in the model grid cell closest to their existing (as of 2012) geographic location. In addition, each optimization is initialized with the utility-scale onshore wind and solar PV that existed at the end of 2012 in the nearest model grid cell for total installed capacities of 59.5 GW and 2.5 GW, respectively (*109, 110*). Thus every scenario that is run has 236.8 GW of capacity installed at the outset.

Figure 14 shows the installed capacities (a,c,e) and amount of generation (b,d,f) by technology for each of the panels shown in Figs 11–13. They show that for all cost scenarios, the amount of wind and solar PV decreases with increasing system number (i.e. decreasing geographic area). These solutions are all cost-optimized, so there is no constraint that enforces some proportion of weather-driven renewable electricity. Comparing the LRHG (a,b) with the MRMG scenario (c,d), we see that solar PV is almost entirely removed from the MRMG solution. The reduction in solar PV between the solutions also leads to a significant drop in the total installed capacity of all combined generation because more natural gas is deployed, but is dispatched by the optimization at a higher capacity factor than in the LRHG scenario. It is worth noting that the onshore wind installed capacity drops by 14% from the LRHG to the MRMG single system solutions, while the generation from onshore wind only falls 3%. The difference is facilitated by more dispatchable natural gas. The placement of the onshore wind has many similarities between the LRHG and the MRMG scenarios for the high-resource locations.

The main observed differences between the MRMG and HRLG scenarios [Fig. 14 (c,d) and Fig. 14 (e,f)] are the reduction of onshore wind and the complete removal of new solar PV and another significant drop in total installed capacity for the HRLG scenario compared with the other two cost scenarios. Interestingly, the HRLG scenario, with a single connected system, has more than double the installed capacity of onshore wind compared with 2012. The cost inputs are relatively similar to those in 2012. Note that there are no incentives, such as production tax credits (PTC) or investment tax credits (ITC), in the optimization for any technology.

Somewhat surprisingly, the installed capacity for each cost scenario is within 60 GW for each of the optimizations for different system numbers, but the share of generation by weather-driven renewables decreases significantly with increased system number. This indicates that the electric power sector is most efficient when connected over large geographic areas irrespective of the generation technology; however, for weather-driven renewable technologies to be most effective, a large-scale connected system is essential. Using the data from the LRHG scenario, natural gas generation increases by 81% between the single

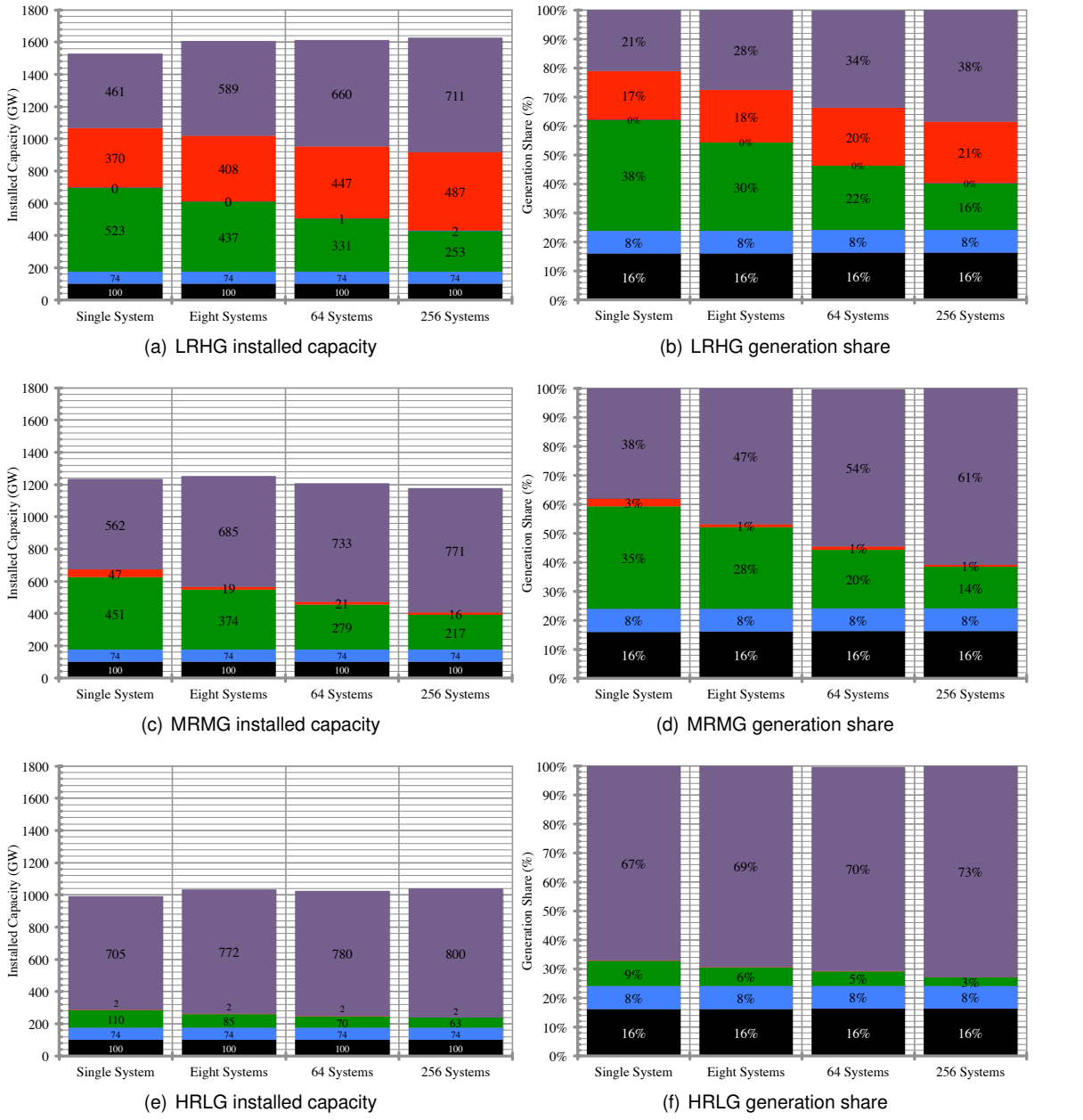

Figure 14: The installed capacity in GW (a,c,e) and generation share (b,d,f) by technology. Each panel shows different geographic scales of electric power systems for the 2007 data year optimizations. (a,b) is for the Low-cost Renewable High-cost Natural Gas (LRHG) scenario. (c,d) is for the MRMG scenario. (e,f) is for the HRLG scenario.

system optimization to the 256 division systems. Solar PV production increases 24% while onshore wind production falls 58%. The MRMG scenario shows a similar trend; natural gas generation increases by

61%, while wind and solar are reduced by 60% and 67%, respectively.

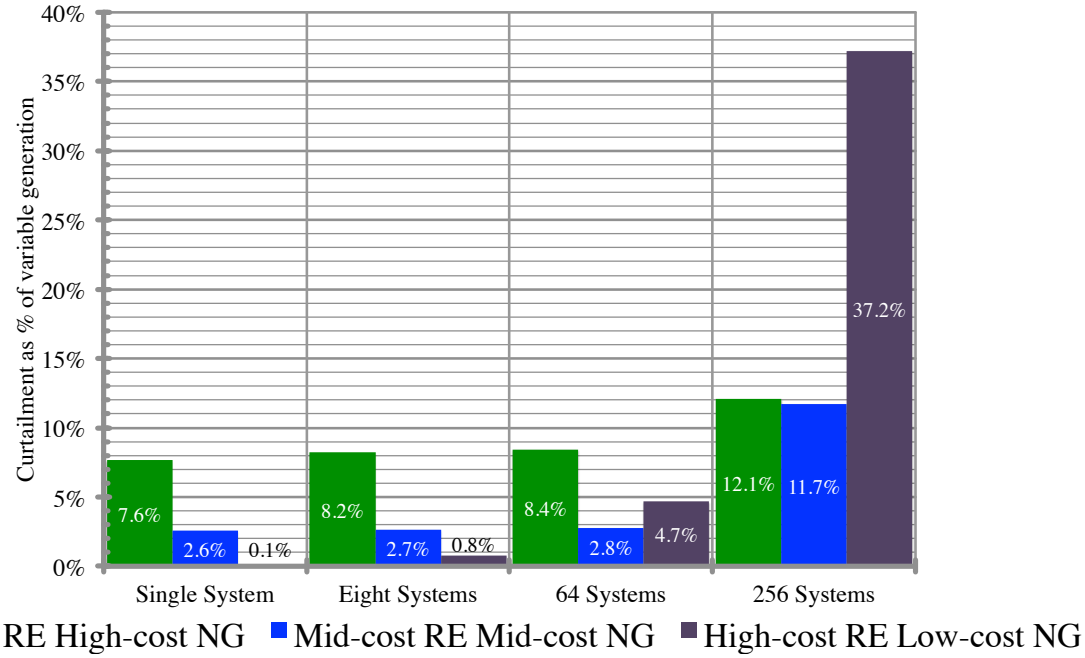

Figure 15: Curtailment of wind and solar PV for the three different cost scenarios. The curtailment is represented as a percentage of the variable generation. Green is for the LRHG scenario, blue is for the MRMG scenario, and purple is for the HRLG scenario. In all three cost scenarios the amount of curtailment increases with increasing number of systems (decreasing geographic area).

To put the large amounts of wind and solar PV for the LRHG scenario in the previous paragraphs into perspective, we compared the magnitude of the wind, solar PV, and natural gas installations found in the optimizations with 2012 installed capacities. Installed utility-scale wind energy in the US was 59.5 GW from more than 40,000 turbines (*109*), while the total installed utility-scale solar PV capacity was 2.5 GW (*110*). Hence, the onshore wind capacity would be approximately ten times greater than in 2012. Equivalently 205,000 2.5-MW wind turbines would be needed, which is five times greater than the number of turbines in 2012 (*109*). For solar PV, the required capacity would have to increase by 65 times compared to 2012 (*110*). Natural gas capacity is reduced slightly from the 2012 US natural gas plant capacity of approximately 486 GW. The installation rate of wind would need to average approximately 31 GW per year from 2015, which is only just over three times the installation rate of 2010 (*109*). Solar PV requires a rate six times greater than occurred in 2012 (*110*). The increase in distributed wind and solar PV generators could improve the security of electricity grid because larger numbers of smaller generators are harder to attack than fewer larger ones. Another important benefit of a system of this kind is the reduction of water use by electric generation. Wind and solar PV use much less water per MWh than fossil fuel generation. In fact, the LRHG scenario national system would consume 65% less water (emit to the atmosphere as water vapor) than the 2012 generation mix when ignoring evaporation from hydroelectric reservoirs (*111*).

In Fig. 15, we display the curtailment of wind and solar PV for each of the three cost scenarios for

four different geographic scales. It can clearly be seen that by increasing the number of systems (or divisions) the amount of curtailment increases. Therefore, increasing the number of systems not only decreases the amount of variable generation, but also more of that generation is curtailed (wasted). The significant curtailment (37.2%) for the HRLG scenario with 256 independent systems is can be explained by three effects: first, the optimization must use the 59.5 GW of existing wind generation that may not be in an optimal configuration for those 256 systems (it is recognized that 256 systems is double the number of systems that existed in 2012); secondly, the wind and solar PV electricity being produced is a small amount; and thirdly, the wind deployed in the existing system is in geographically large systems and so can be utilized more effectively and is not captured by the NEWS model at these system sizes. The study was designed to investigate geographic scaling on the electric power sector with variable generation, so existing balancing authority areas, independent system operators, etc. are not recognized within the model. Markets in 2012 that contained wind on their power grids reported between 2 and 4% of curtailment (*112*). Over recent years, the totals have been as high as 18%, but expansions in local transmission, changing policies for non-variable generators, improved forecasts, and increased system flexibility have improved these numbers (*112*). The excessive curtailment of wind and solar PV for the 256 division system for the High-cost Renewable Low-cost Natural Gas (HRLG) scenario occurs because without effective transmission and low natural gas fuel costs it is more economical to curtail the variable generation and use natural gas instead. Therefore, for the 256 division system studied (significantly more fragmented than the 2012 electric power system), the existing wind and solar PV plants are not economically optimal (i.e. if the optimization could choose not to build those existing wind and solar PV plants it would not have done so). For reference, the smallest geographic area studied in the model results in 256 equally sized 32,700 km^2 electric power systems, while in the current US system, the largest operator is the Midcontinent Independent System Operator (MISO) that covers an area of approximately 1,338,000 km^2 within the US (`www.misoenergy.org`). However, the geographic scale study implies that the numerous US electric power systems that cover small areas will not be able to deploy utility-scale wind and solar PV to high penetration levels (cost competitively) because of the variability of wind and solar PV within their boundaries.

In Fig. 16, we display a summary of the overall features of the geographic scaling study. Figure 16 (a) shows the CO_2 emissions from the electric sector compared with 1990 levels. It clearly indicates that more independent (therefore smaller) electric power systems emit more CO_2 than fewer systems; this holds true to all three cost scenarios. In Fig. 16 (b), we can see the cost of electric power systems compared with the single connected system. With increasing system number comes increasing costs. Figure 16 (c) demonstrates that the smaller the geographic area the less wind and solar PV generation there is. The reduction in wind and solar PV generation leads to increasing costs and higher CO_2. Therefore, these results indicate that to get the greatest reduction in CO_2 emissions from wind and solar PV for the lowest total annual cost, the largest connected electric power system possible should be implemented. In all cost scenarios, there is a reduction from 1990 levels; some of which is attributed to the avoidance of CO_2 from coal power plants. For example, for the High-cost Renewable Low-cost Natural Gas (HRLG) scenario with 256 independent electric power systems, 27% of the electricity is generated from carbon-emission-free technologies (compared with the 31% in 1990), but the system only emits 72% of CO_2 compared with 1990 levels.

For the remainder of the present subsection, we describe the features of electric power systems that

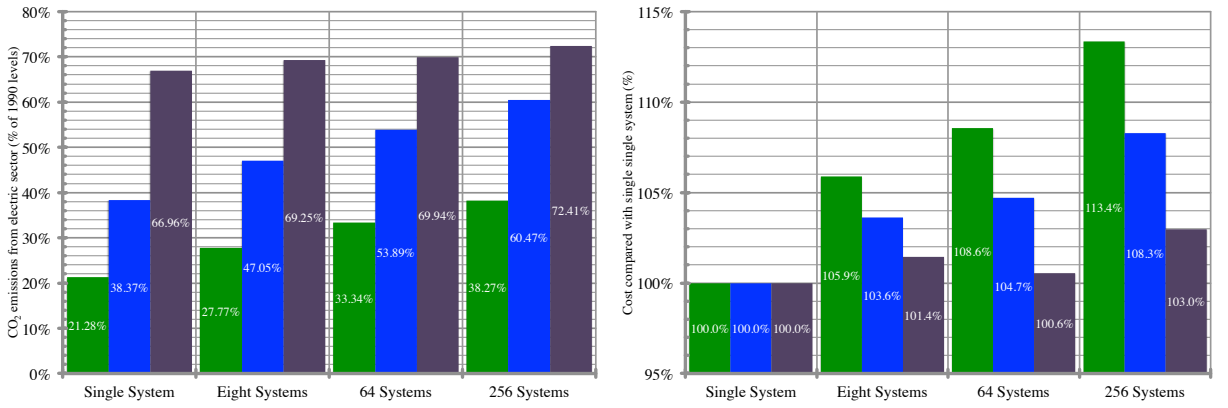

(a) CO_2 emissions compared with 1990 levels

(b) Cost of total system

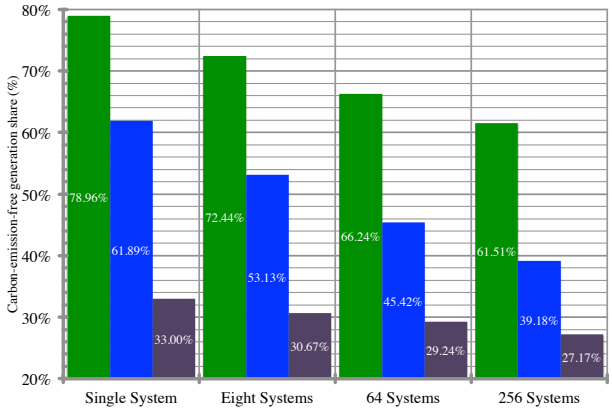

(c) Carbon-emission-free generation

Low-cost RE High-cost NG Mid-cost RE Mid-cost NG High-cost RE Low-cost NG

Figure 16: Summarized picture of the geographic scaling study. All three cost scenarios are shown. Four of the nine geographic scales investigated are shown. (a) Displays the CO_2 emissions from the electric sector as a percentage of the emissions from 1990 levels. It illustrates that with a decrease in geographic area (increase in number of independent power systems) the CO_2 emissions increase. (b) Shows the total cost of the electric power sector compared with the single connected contiguous US system. The panel indicates that cost-optimal systems over smaller geographic areas are more expensive than larger systems. (c) The share of the electricity generated by carbon-emission-free technologies. It can be seen that with smaller geographic areas less carbon-emission-free generation is selected by the optimization.

incorporate large amounts of wind and solar PV that are generated by the optimization model. The best scenario to perform this analysis on is the Low-cost Renewable High-cost Natural Gas (LRHG) scenario as it has the maximum wind and solar generation. Accordingly, the following figures will only display the LRHG scenario results for the 2007 data year.

A fundamental constraint in the optimization was to supply enough electricity to serve the load every single hour of the year within each electric power system without fail. To do so, the optimization algorithm has to ensure that the interplay of the generation from wind, solar PV, natural gas, nuclear and hydroelectric

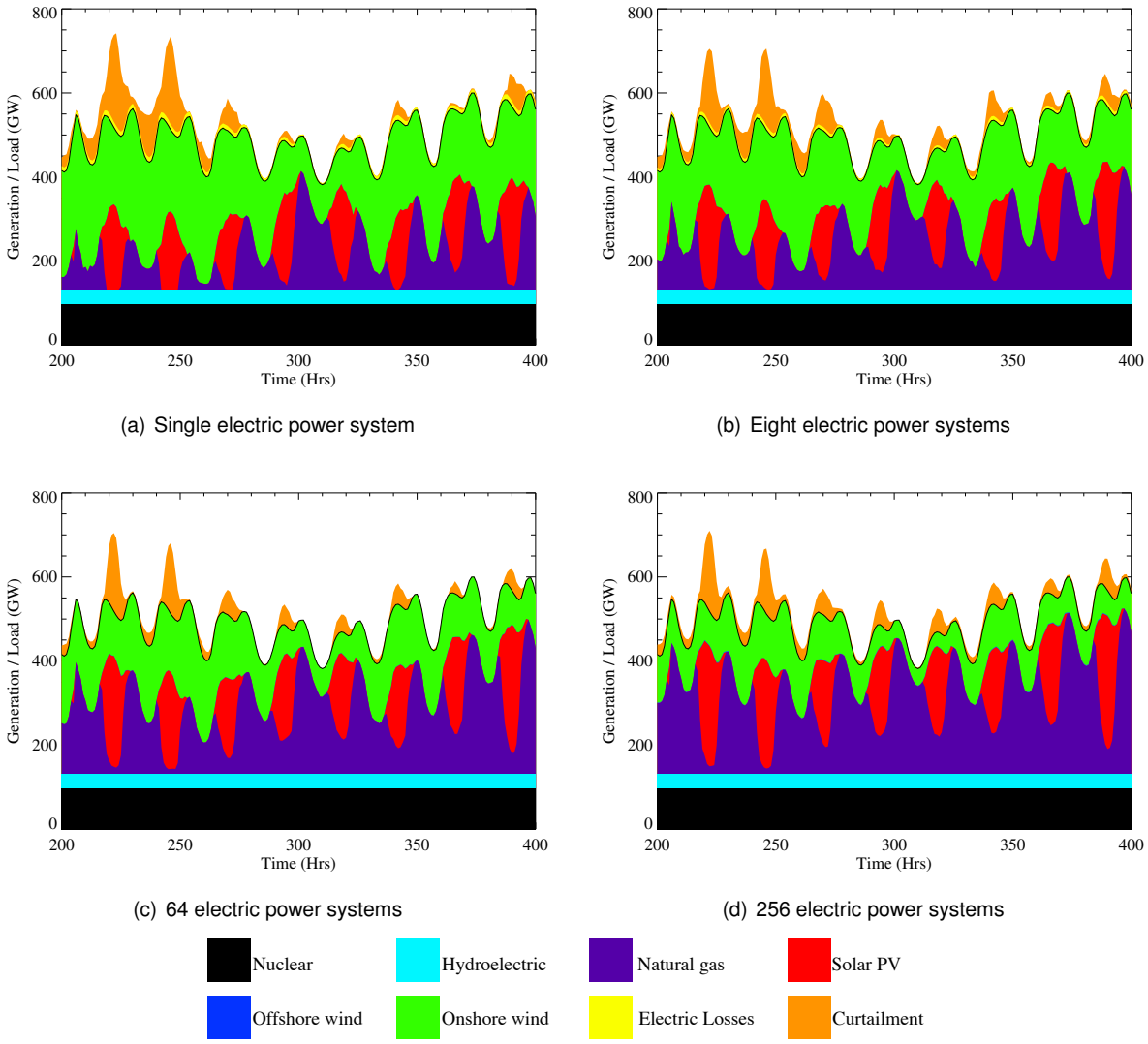

Figure 17: Sample wintertime dispatch stacks for the Low-cost Renewable High-cost Natural Gas (LRHG) scenario for the 2007 data year. The vertical axes displays the generation and load (black line above wind) requirements in GW and the horizontal axes label the hour of the optimization. The dispatch stacks show the time period of 08:00 UTC January 8th to 16:00 UTC January 16th. Each panel shows the aggregated US electric power sector generation and demand. The panels are for (a) a single connected electric power system, (b) eight independent electric power systems, (c) 64 independent electric power systems, and (d) 256 independent electric power systems.

sources, along with reduction due to the electrical losses along transmission corridors, results in electricity reaching its destination at the correct time step everywhere. The algorithm achieves this while producing a minimum total yearly cost. To illustrate how the different generators contribute we display 200 sequential hours from January and from July (to represent winter and summer) in Figs 17 and 18, respectively, showing how the electric demand varies on diurnal, weekly and seasonal cycles. The same four division

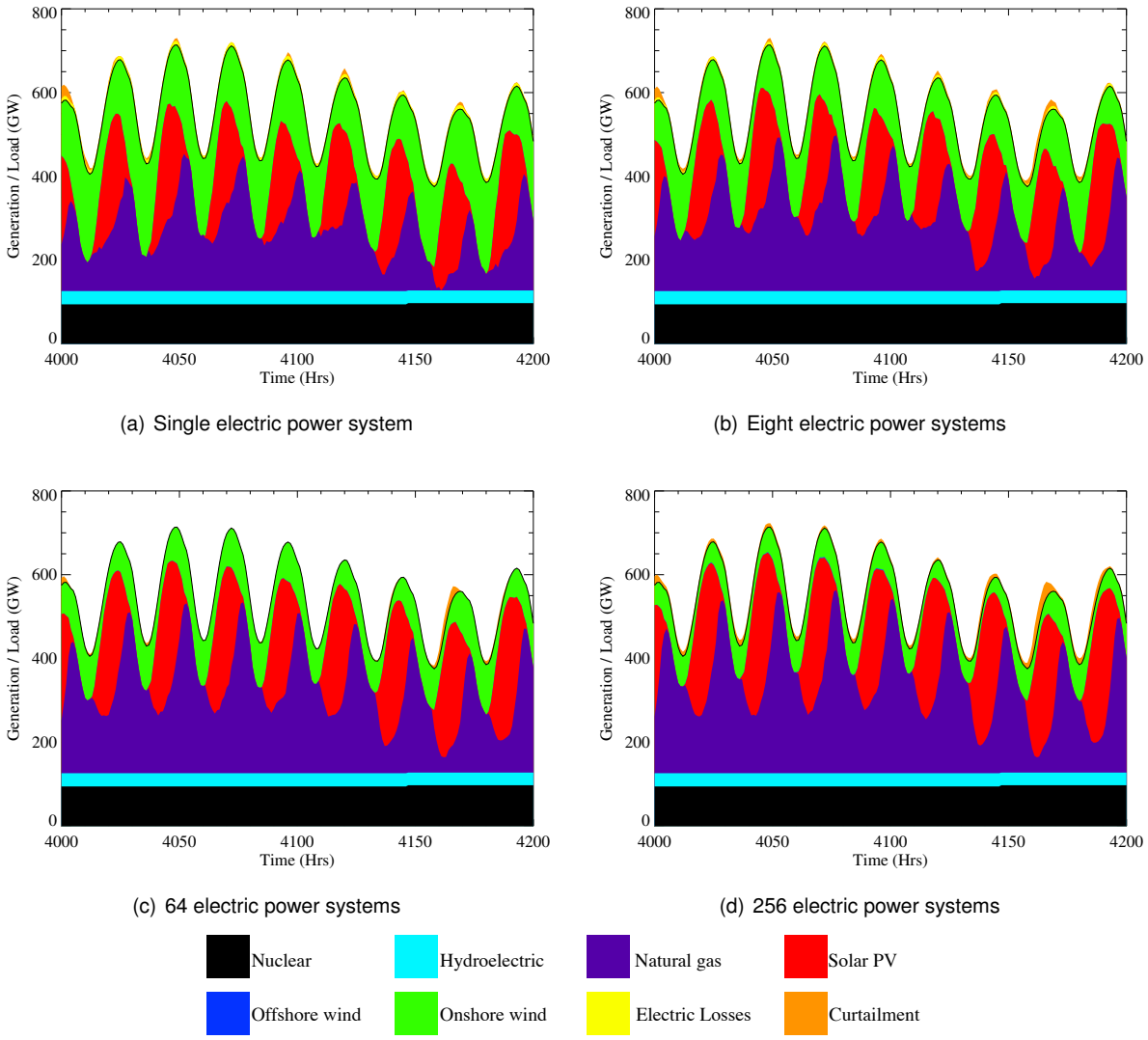

Figure 18: Sample summertime dispatch stacks for the Low-cost Renewable High-cost Natural Gas (LRHG) scenario for the 2007 data year. The vertical axes displays the generation and load (black line above wind) requirements in GW and the horizontal axes label the hour of the optimization. The dispatch stacks show the time period of 22:00 UTC June 15th to 06:00 UTC June 24th. Each panel shows the aggregated US electric power sector generation and demand. The panels are for (a) a single connected electric power system, (b) eight independent electric power systems, (c) 64 independent electric power systems, and (d) 256 independent electric power systems.

size configurations of the LRHG scenario are shown as in Fig. 11. The effect of geographic scaling on the use of wind and solar PV on hourly time steps is readily apparent. Most prominently, Figs 17 and 18 (d) have much less onshore wind contributing to the electric mix compared to panels (a). In addition, there is an increase in the ramping of the natural gas. In fact, in all of the panels, there is extensive ramping of the natural gas plants to complement the variations in the wind and solar PV.

One interesting aspect is the daily ramping of wind and solar PV and how that effects the natural gas daily cycling. Each morning the solar PV ramps up rapidly, and this compensates for the down ramp in the wind generation; in fact it over compensates for it, and natural gas is down ramped (indeed sometimes natural gas is turned off and some variable generation must be curtailed). We can observe that the solar PV reaches maximum output before the demand peaks (particularly obvious in summer). The difference in the maximum output in solar PV and wind leads to the natural gas needing to ramp up rapidly each each day reaching its maximum in the late afternoon. Even though we show additional ramping, it happens regularly and in a fairly similar pattern each day. Cycling like this is part of the daily rhythm of the electric demand; it is just exaggerated by the solar PV rapid ramping each day.

Even though storage was never selected by the optimization, because it was too expensive, there is significant opportunity for storage if it becomes cheaper or the societal benefits are high enough. In Fig. 17 we see times of over production, which in these solutions results in curtailment (when electricity is not utilized and shed). The over production could be used as an opportunity with storage and could then be dispatched to reduce the ramping needs of the natural gas plants and avoid scarcity pricing within electricity markets. Indeed, in our model we have simplified the hydroelectric power output; it may not vary much (5%) from the values set out in subsection 1.3. Of course, in reality it may be prudent to dispatch hydroelectric generation to follow the variations in wind and solar PV to complement their behavior. We did not do this in the current study because of the limitations on dispatching hydroelectric as discussed in subsection 1.3. In addition, we are focusing on the complementary nature of wind, solar PV, and natural gas with scale. If hydroelectric power output was dispatched as well, it would have added another degree of freedom and complexity, but could result in more variable generation being utilized.

Figure 17 depicts that at some time steps there is curtailment of variable generation and natural gas is being dispatched. These occurrences happen more frequently when the number of electric power systems increase (c.f. panel (a) and (d)). It appears to be a contradiction to have variable generation being curtailed (which increases net costs for variable generators) while burning fossil fuels (increasing the net cost of natural gas) at the same time in a cost optimization; however, this contradiction is only apparent and can be understood in terms of transmission. If there is congestion on transmission lines at a particular time step, the optimization has to choose whether to construct a higher capacity HVDC line or not. If over the entire year the cost to build a higher capacity line is greater than curtailing variable generation and burning natural gas (and building any extra required capacity), the line will not be expanded. Further, if the HVDC transmission line is already at full capacity (12 GW in the model), then the optimization has no choice but to curtail the electricity; if the amount of curtailed electricity increases substantially and the associated costs are no longer optimal, the optimization will change the generation mix. The reason the curtailment and natural gas dispatch increases with more electric power systems is simply because curtailment could be occurring in one system that is not connected to another system that is dispatching the natural gas plants.

Figures 17 and 18 highlight an important feature of the optimization model. The model dispatches generators, transmits power, and takes into consideration electric losses and curtailment while simultaneously deciding the siting of all the different technologies. It is important to do this because of the variable nature of wind and solar PV. Only computing the annual electricity production and consumption is not sufficient. Electricity must be provided where and when it is needed. When comparing the wind and solar PV generation it becomes possible to see that they have different and complementary benefits and challenges for

electric power systems. Solar PV has a big impact on ramping and cycling of natural gas. Solar PV ramps substantially each day because of its lack of inertia and following the Sun's daily cycle, while wind tends to ramp more slowly. Wind power output is generally higher at night than day and that complements the solar PV that peaks in the day (and none at night). Wind power output is less strongly correlated with the diurnal cycle than solar PV is and that allows lower frequency ramping of natural gas plants. It is clear from Figs 17 and 18 that the concepts of base load, intermediate load and peak load are not appropriate for variable generation-dominated electric power systems; instead a geographic metric would be necessary to show where electricity production and consumption is high and how transmission will need to be used to facilitate the flow of power between those regions.

Since Figs 17 and 18 show only 200 hours of two seasons, we need some way to consider the behavior of the wind and solar PV over the entire year. We construct histograms that show the difference between the aggregated carbon-emission-free generation and electric demand for the entire electric power sector for each optimized system. We display four examples in Fig. 19. When the difference is positive, there is a *surplus* of wind and solar PV generation, and when it is negative, there is a *shortfall* of wind and solar PV (where natural gas needs to be dispatched). In general, the histogram shifts to the left and becomes broader as the number of electric power systems increases. The shift to the left and the broadening indicates a greater need for natural gas capacity and ramping. All four of the examples have approximately the same maximum surplus ($\sim$200 GW) because of the high penetration of solar PV that creates high surplus in the spring and fall.

Another noticeable feature is that as the number of electric power systems increases (from panel (a) to (d)), the histogram becomes less smooth. It is worth mentioning that the peak of the histogram is to the left of the zero line. This is a consequence of the choice of optimization. If we optimized using load matching, the histogram would be centered on the zero line, and would be narrower. The behavior of the load matching technique is contained in Clack *et al.* (*22*). However, since we performed a cost-optimization, the histogram is shifted left of the zero line. The shift left is because the surplus electricity is an (implicit) cost to the wind and solar PV generators, which reduces its competitiveness against the natural gas power plants. With a single connected electric power system, the surplus can be greater because access to higher capacity wind and solar resources reduce the overall generation cost of wind and solar PV. Thus, more electricity can be curtailed for a given cost of natural gas. Other information can be found from the histograms shown in Fig. 19; the integral of the right-hand side of the black line is the amount of electricity curtailed and the integral of the left-hand side of the black line is the amount of electricity supplied by the natural gas generation. Note that to achieve 100% carbon-emissions-free generation the histogram would need to be entirely shifted to the right of the zero line. Therefore, as shown achieving higher amounts of wind and solar PV generation will increase costs nonlinearly. That is because with each wind and solar PV plant added, more electricity will be curtailed due to correlation between existing generators as the histogram marches to the right of the zero line. Some of this effect will be demonstrated by the natural gas sensitivity study in subsection 2.2.

We saw in Figs 17 and 18 that natural gas power plants are ramped regularly each day due to the wind and solar PV variable generation. The figures only show 200 hours in two seasons. To understand the overall performance of the natural gas plants with regards to ramping, we computed the change in output from one hour to the next for the every hour of the year in the optimized systems. Ramp rates are

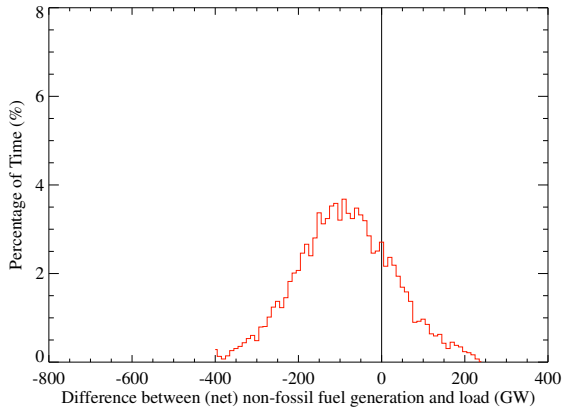

(a) Single electric power system

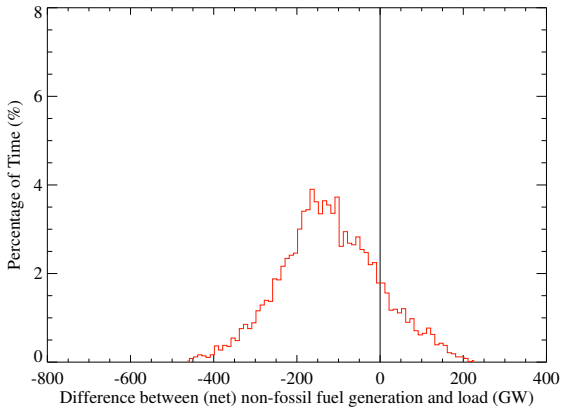

(b) Eight electric power systems

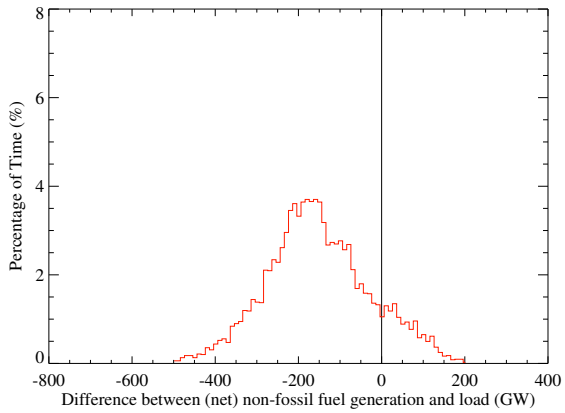

(c) 64 electric power systems

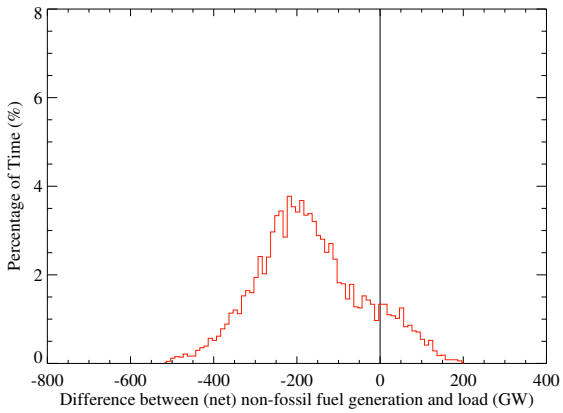

(d) 256 electric power systems

Figure 19: Histograms of the difference between the aggregated carbon-free-emission generation and the demand in GW for the US electric power sector. The panels display the values for the 2007 data year LRHG scenario. Negative values denote a need for fossil fuel generation and positive values represent requirements for curtailment of variable generation. The vertical axes represents the percentage of time represented by each 10-GW bin. The panels show the (a) single connected system solution, (b) eight independent systems, (c) 64 independent systems, and (d) 256 independent systems. It can be seen that with increasing system number the histogram moves further left, signifying a greater use of fossil fuels. In addition, the histogram is more broad, taking a wider range of values, therefore increasing ramping of the fossil fuel generators.

important because natural gas generators are constrained by physical limits; currently modern combined cycle natural gas power plants have the ability to ramp $\pm$7% of capacity per minute (*113*). The histograms of these computations are shown in Fig. 20. The histograms are binned in 2% increments of the aggregated installed capacity of natural gas. Again, we display the four example cost-optimized electric power sectors. It is clear from Fig. 20 that as the number of electric power systems increases (panel (a) to (d)) the peak of the histogram diminishes (fewer time steps with zero ramp rate) and becomes less symmetric. In general,

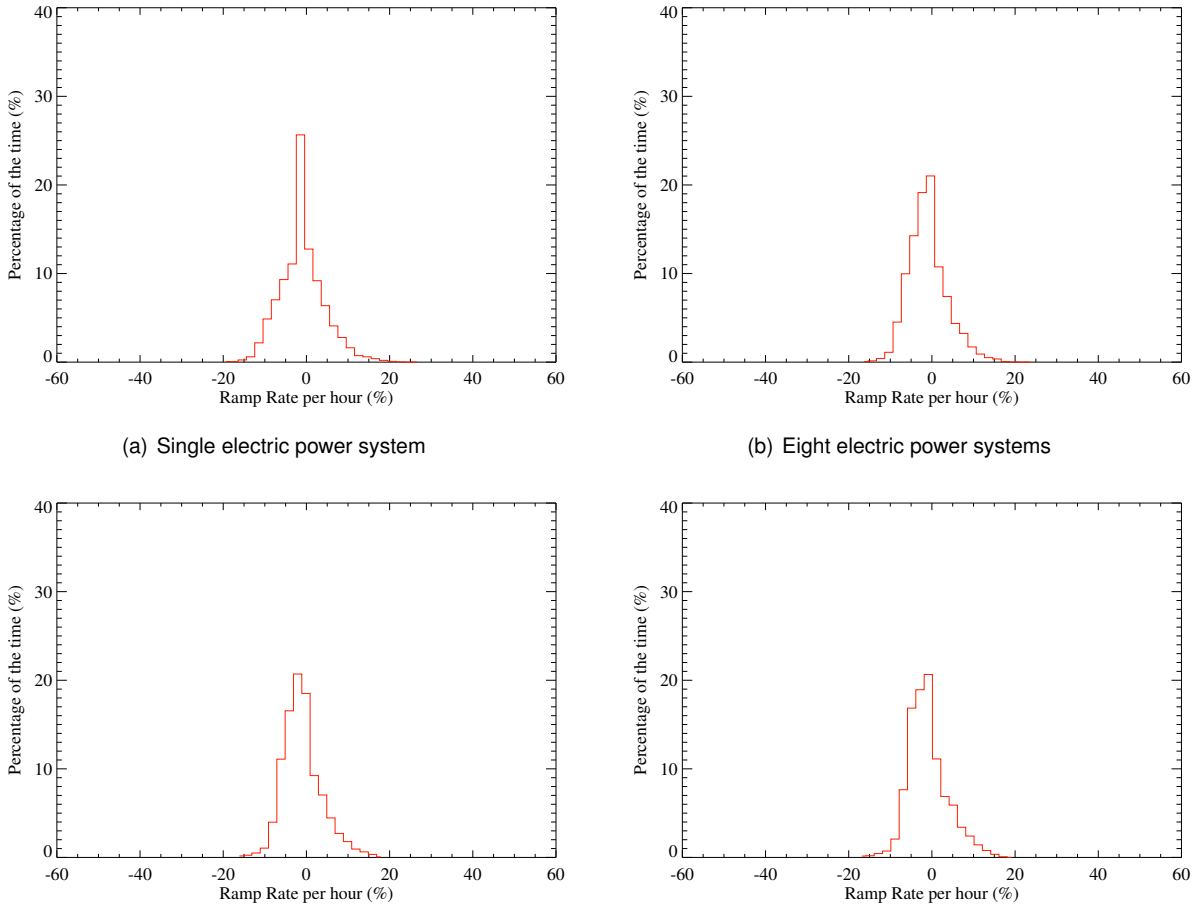

(a) Single electric power system

(b) Eight electric power systems

(c) 64 electric power systems

(d) 256 electric power systems

Figure 20: Histograms of the aggregated hourly rate of change of generation output (ramp rates) for the natural gas power plants. The vertical axes represent the percentage of time the system has a ramp rate of a certain value (2% bin size). The horizontal axes show the aggregated ramp rates of the natural gas power plant fleet. The panels show the (a) single connected system solution, (b) eight independent systems, (c) 64 independent systems, and (d) 256 independent systems. Immediately we can see that (a) has a much higher peak at 0% ramp rate for the natural gas fleet. This is due to carbon-emission-free generation supplying 100% of the electricity. It can also be seen that the aggregated fleet in (a) has wider tails than the other panels. The wider tails can be explained partly by the fact that a single system has lower installed capacity of natural gas plants than the other systems, but also because there is less variable generation in the more fractured electric power sectors.

the up ramps (when the power output from natural gas plants increases) have a longer tail than the down ramps, which is more pronounced in the electric power sector with more independent power systems. The difference between the up and down ramp behavior can be attributed to the combination of how the wind and solar PV power outputs vary in concert. The solar PV power output reduces rapidly each evening towards sunset, while the wind has inertia and takes times to ramp up; to balance the load, the system

must dispatch natural gas. In the morning the opposite is true, wind ramps down more gradually than solar PV ramps up; thus the dispatch down for the natural gas plants has a shallower gradient. In addition, the electric demand is higher in the late afternoon compared with the morning. Of course the described behavior is a generality, and there are times when this is not true, but over the year it averages out to cause the up ramps on the histograms to have longer tails.

Figure 20 indicates that with more electric power systems there are fewer large ramping events (say 10% of the natural gas power plant fleet). There are three reasons behind this. First, there is more natural gas plant capacity when there are more electric power systems (see Fig. 14). Hence, if the amount of ramping were the same in megawatts (MW) the percentage would be reduced. The second reason is that there is less wind and solar PV generation. Finally, we are only displaying aggregate values for the entire electric power sector. Each individual electric power system has its own mix of generators and the ramp rate histograms look different for each system because the amount of natural gas capacity varies between systems. It is not practical to show each individual system (or pick random ones), so for completeness, we note that the most extreme ramp rates are $\pm$60% of the natural gas installed capacity for any of the optimized systems within the 256 division LRHG scenario. The ramping does make the system control aspect more complex. However, even the extreme hourly ramp rates ($\sim$60% of capacity) are within the capabilities of modern natural gas combined cycle power plants. It is not known if the sub-hourly ramping is more extreme as the temporal resolution of the model is hourly and so we have no ability to comment on these timescales. It should be stated that the electric load has intrinsic ramping that must be matched by the generation fleet. It can be shown that the extreme ramps of the electric load for the 2007 data year are -18% and +13%. Hence, adding wind and solar PV does increase the ramping requirements of the dispatchable generators in the electric power sector; crucially (at hourly resolution) the ramping does *not* exceed the ability of current natural gas plant technology. In addition, in larger connected systems shared generator resources mean that ramping increases on a percentage aggregated basis, but can substantially reduce the ramping that would occur within some of the smaller electric power systems.

2.2 Natural Gas Sensitivity Study

The geographic study reduced the electric power sector down to a small number of generator types; wind, solar PV, nuclear, hydroelectric, and natural gas. It enforced that nuclear and hydroelectric capacity must remain constant, so that the effects of geographic scale on wind and solar PV with natural gas back up could be investigated. It is clear that the cost of these technologies has a big impact on the overall system configuration. One of the most volatile costs is that of the natural gas fuel. Monthly-averaged costs for natural gas fuel for electricity have been as low as $3.70 and as high as $13.43 (2013$) per million British thermal units (MM Btu) in the decade between 2002 and 2012 (`http://www.eia.gov/dnav/ng/hist/n3045us3m.htm`). The daily well head spot prices have a larger spread of $2.19–$23.40 (2013$) with these extremes occurring within one year of each other (`http://www.eia.gov/dnav/ng/hist/rngwhhdd.htm`). Clearly, the natural gas fuel cost changes at a much higher frequency than the technology costs. Therefore, it is important to analyze the sensitivity of cost-optimized electric power systems to natural gas fuel cost. The sensitivity study can also be utilized to calculate a carbon tax that would be necessary for a given market cost of natural gas fuel that facilitates a desired percentage of carbon-emission-free

generation for electricity. In the present subsection, we describe the results of a natural gas sensitivity study we conducted.

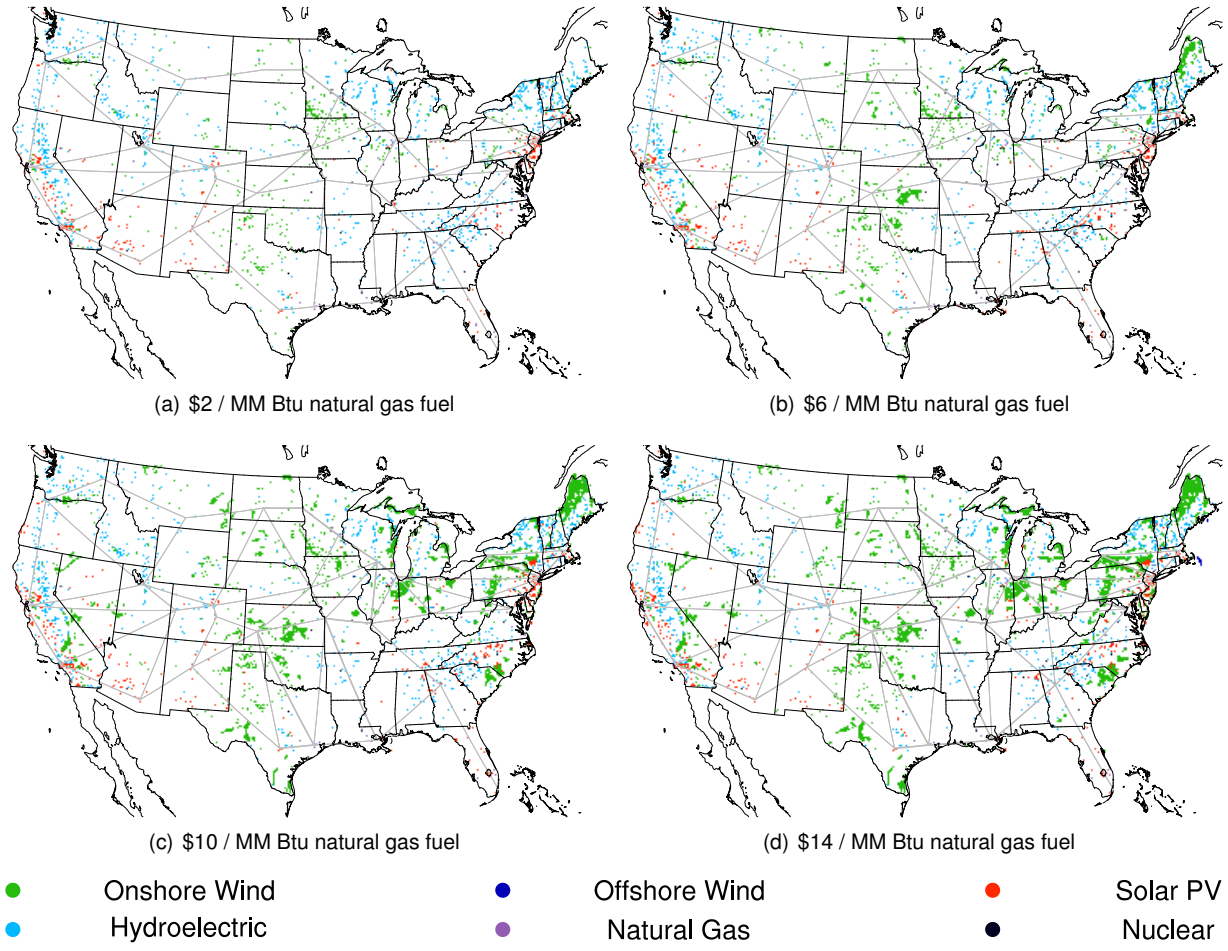

Figure 21: The changing configuration of a single connected contiguous US electric power sector due to natural gas fuel cost changes. The gray lines represent the HVDC built by the optimization and the thickness of the lines are proportional to the capacity. The renewable costs are set to those in the Low-cost for each technology. We show four of the 15 natural gas fuel costs run for the Low-cost Renewables over the data year 2007. We show the optimization configuration for (a) $2 / MM Btu natural gas, (b) $6 / MM Btu natural gas, (c) $10 / MM Btu natural gas, and (d) $14 / MM Btu natural gas.

The natural gas sensitivity study focuses on a single connected contiguous US electric power system. We performed the study on each of the three data years of 2006–2008. The cost of the generators and HVDC transmission are identical to those used for the three cost scenarios for the geographic scaling study (see Table 3). We do not use the natural gas fuel costs from that table. Instead, we vary the cost of natural gas fuel from $0 to $14 / MM Btu (2013$). For the natural gas sensitivity study, we performed a total of 135 optimizations. For the sake of clarity, we only show a single data year (2007) and a selection of graphics that illustrate the main points of the investigation. As with the geographic scaling study, the different data

years show small quantitative differences, but the overall results are qualitatively very similar. To be clear, the only difference between each optimization run for a specific data year and technology cost is the natural gas fuel cost.

Figure 21 shows the optimal configurations of four (from 15 possible) natural gas fuel costs for the Low-cost Renewables over the 2007 data year. As the natural gas fuel cost increases, the amount of wind and solar PV sites increases. The new siting of wind and solar PV between two natural gas fuel costs is interesting because it indicates the marginal cost of those new generators. The difference between panels (a) and (b) is more pronounced than between panels (c) and (d), even though the difference in natural gas fuel is the same at $4 / MM Btu, indicating that wind and solar PV marginal costs are higher between (c) and (d) than between (a) and (b). In Fig. 21 (d) there is a large offshore wind farm off the coast of Cape Cod. This indicates that at $14 / MM Btu offshore wind at $3.41 / W has become economical in a single connected electric power system. We can also see that the amount of HVDC transmission is substantially increased from low-cost to high-cost natural gas fuel, but the HVDC system is present in all of the optimizations regardless of generation mix. This reinforces the conclusion from the geographic scaling study that the HVDC transmission lines make the electric power sector more economical irrespective of generator technology.

Figure 21 also illustrates that as natural gas fuel cost increases, more wind and solar PV sites are selected; however, it is not guaranteed that if a site is selected at a lower cost of natural gas fuel it will be selected at a higher cost of natural gas fuel. For example, in Fig. 21 (b) there is a line of solar PV plants along the Tennessee-Alabama border that are not present in panels (c) or (d). This fact raises a fundamental concept: the future electric power system will be cost optimal only if the final system can be envisioned at the outset, although it may be that many roughly similar configurations may have only slightly different costs.

Figure 22 displays the total installed capacity (GW), while Fig. 23 shows the generation share (%). Both figures are divided by technology and are shown as a function of the cost of natural gas fuel. The $0 per MM Btu for natural gas fuel cost provides a reference point. The optimization must select 100.4 GW of nuclear and 74.4 GW of hydroelectric, along with a minimum of the existing 59.5 GW of onshore wind and 2.5 GW of solar PV. At $0 / MM Btu, we can see if any variable technology can compete with a dispatchable one without fuel costs. Not surprisingly, for the Mid-cost Renewable and High-cost renewable scenarios no technology can. For the Low-cost Renewable scenario, actually 3 GW (500 MW new installed) of solar PV ($1.19 / W) can compete economically with natural gas because solar PV is actually cheaper per installed Watt than natural gas ($1.24 / W) and there is part of the natural gas fleet that is only dispatched for summer time peaks. If they are dispatched infrequently, the capacity factor drops; increasing the cost of generation.

In Fig. 22 it is easy to compare the different cost implications for the installed capacity of the single connected contiguous US system. The higher the cost of natural gas fuel, the larger the total installed capacity. The solar PV is squeezed out of the systems entirely in the High-cost Renewable scenario. The High-cost Renewable scenario is simply a wind and natural gas dominated system. The solar PV presence in the Low-cost scenario reduces the installed capacity of wind compared with the High-cost scenario, yet the total installed capacity of all generation is much higher. We can explain this because solar PV has a lower capacity factor, but is more correlated to the load. So it increases its capacity at the expense of both

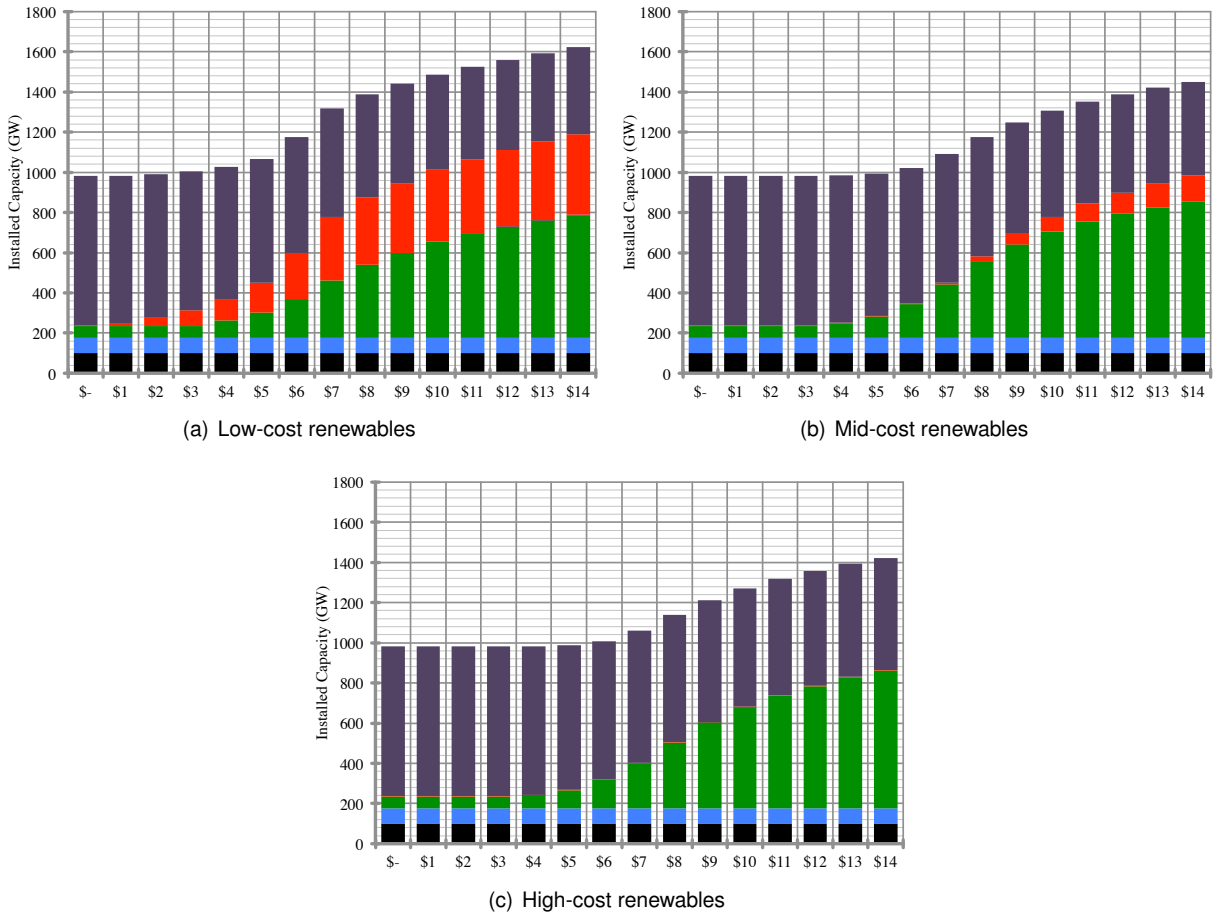

Figure 22: The installed capacity (GW) by technology for the natural gas sensitivity study over the 2007 data year. Each panel displays the capacity of each technology for the full range of natural gas fuel costs simulated. (a) Shows the Low-cost Renewables scenario, (b) displays the Mid-cost Renewables scenario, and (c) is the High-cost Renewables scenario. In all panels there is a cost of natural gas fuel below which no wind or solar PV is developed. Moreover, the deployment of wind and solar PV with increasing natural gas fuel cost is not linear. As more wind and solar PV are added, the overall installed capacity increases.

natural gas and wind; however, more installed capacity of solar PV is needed compared with the removed capacity of wind and natural gas.

Figure 23 depicts how the increase in installed capacity translates to the share of electricity generation by technology. It illustrates the effect of capacity factor on the change in distribution of technology share when compared with installed capacity. It is clear from Fig. 23 that there is a specific cost of natural gas fuel below which no (or very little) variable generation is chosen for large-scale development. For panel (a) it is ∼$2 / MM Btu, for (b) it is ∼$4 / MM Btu, and for (c) it is ∼$5 / MM Btu. Initially there is a steep increase in the use of wind and solar PV because high resource areas are available and curtailment is not an issue because their share of total electricity is still relatively low. Eventually, with continued natural gas

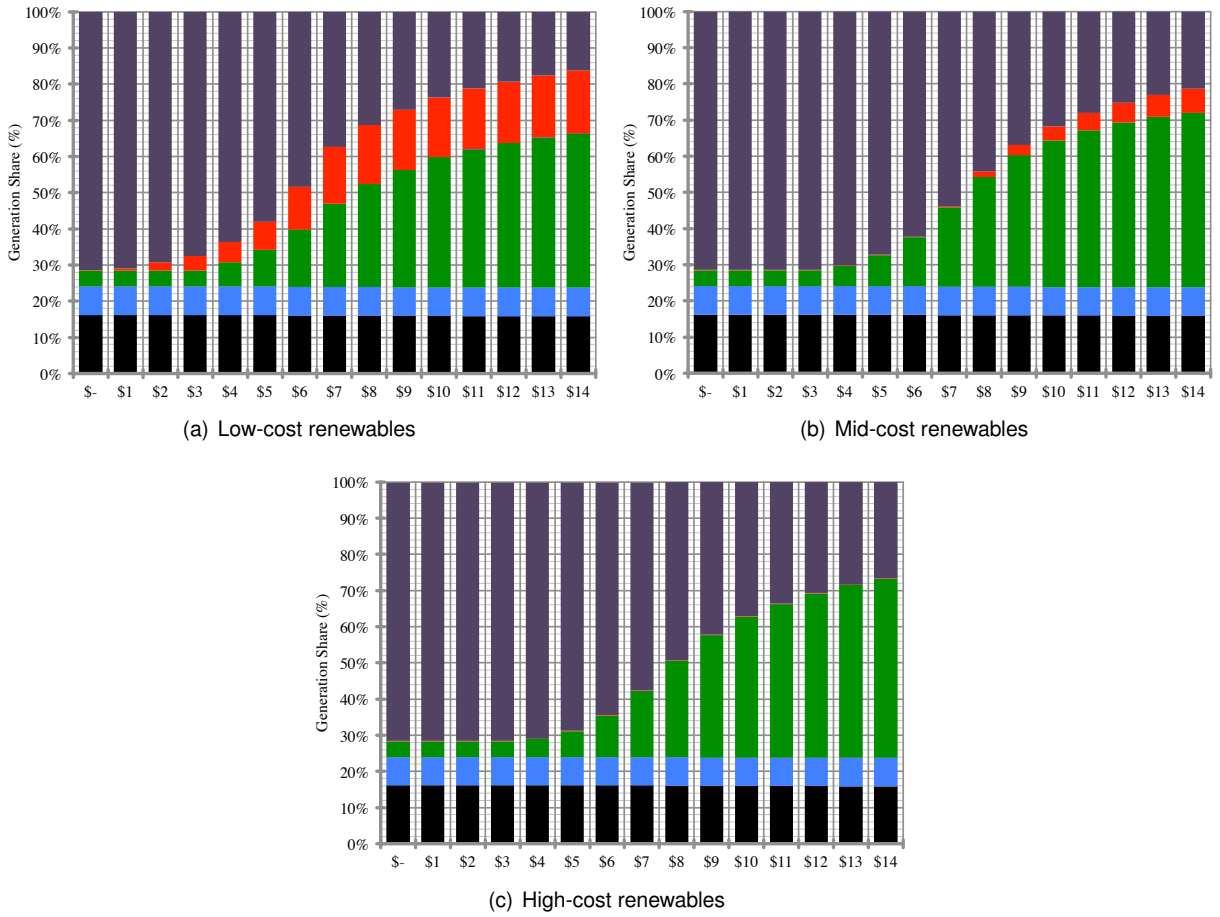

Figure 23: The generation share (%) by technology for the natural gas sensitivity study over the 2007 data year. Each panel displays the share of electricity provided by each technology for the full range of natural gas fuel costs simulated. (a) Shows the Low-cost Renewables scenario, (b) displays the Mid-cost Renewables scenario, and (c) is the High-cost Renewables scenario. The nonlinear behavior of the addition of wind and solar PV is very pronounced. Once all the high-resource, low-correlated wind and solar PV sites are developed, the system moves to less desirable choices, substantially slowing the increase in wind and solar PV generation share. From an economics standpoint this is understood to be caused by increasing marginal cost for wind and solar PV generators.

fuel cost increases, the highest resource sites are saturated, and when new sites are selected, some of the electricity begins to be curtailed further raising costs.

An interesting analogy is that of population growth. At first it is very rapid, but at some point the population reaches a turning point where resources and competition become scarce, which acts to limit the growth. The development of wind and solar PV is limited by the correlation between resources, transmission constraints, and curtailment of over-produced electricity. Using the three panels of Fig. 23, we estimate the inflection point is at a level of $\sim$60% carbon-emission-free generation (in these simulation that

equates to ∼36% combined wind and solar PV). The cost of natural gas fuel is necessarily different for each cost scenario where the inflection point to occurs. It is at these penetration levels that electric storage will increase in value to reach higher carbon mitigation amounts because it has the ability to decorrelate the generation from different wind and solar PV plants.

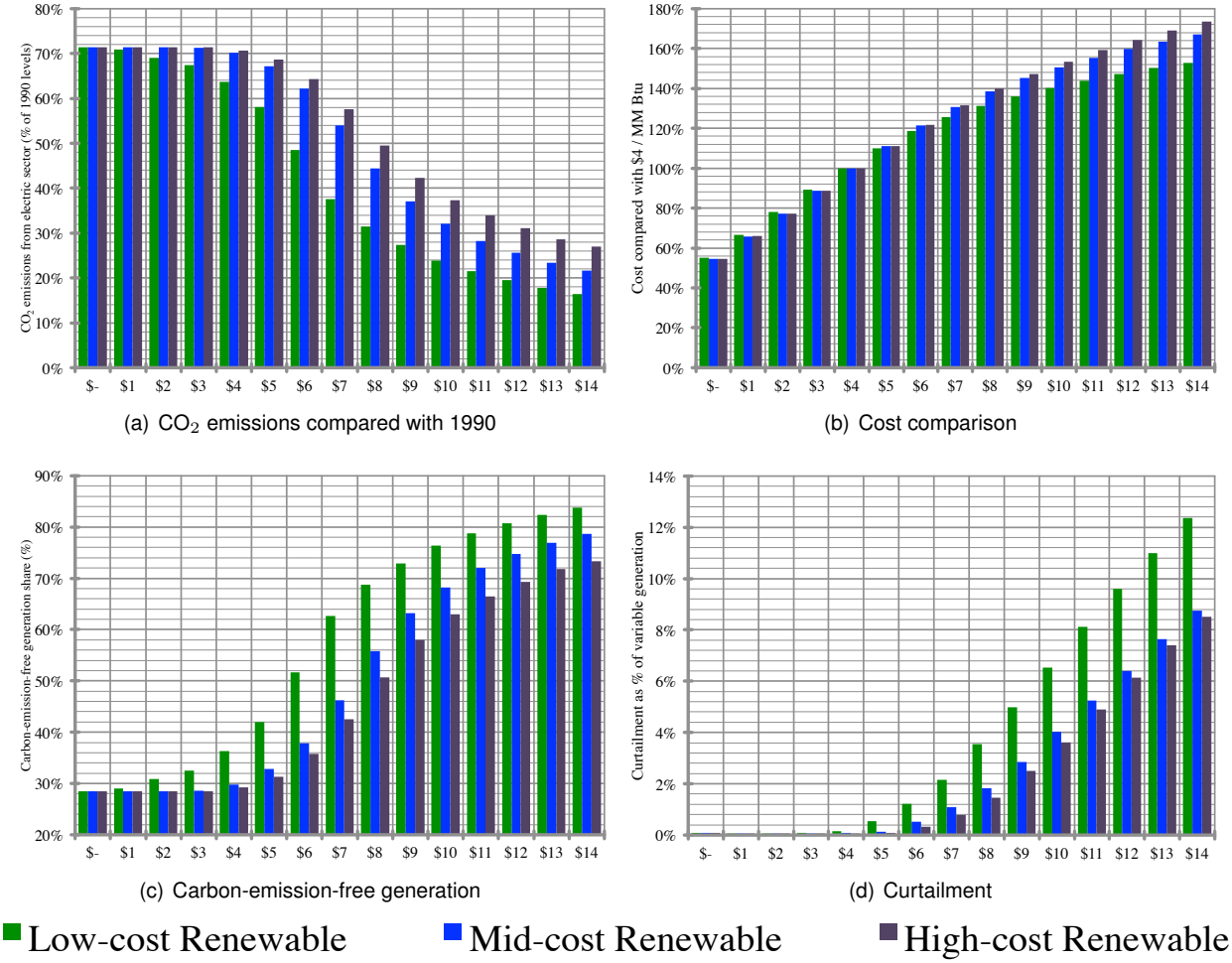

Figure 24: Summarized picture of the natural gas sensitivity study. All of the natural gas fuel costs are shown for the three different technology costs over the 2007 data year. (a) Displays the CO_2 emissions from the electric sector as a percentage of the emissions from 1990 levels. It illustrates the decrease in emissions with rising natural gas fuel cost, but with diminishing returns at the highest costs; there is a negative logistic relationship. (b) Shows the relative total system costs compared with the system produced by $4 / MM Btu natural gas fuel cost. The cost differences exhibit a power law relationship. (c) Highlights the carbon-emission-free generation at the various natural gas fuel costs. It can be represented by a logistic function, suggesting diminishing increases in wind and solar PV generation share with higher natural gas fuel cost. (d) Represents the curtailment of wind and solar PV as a percentage of total wind and solar PV generation at each natural gas fuel cost. The increase in curtailment is steepest for the Low-renewable scenario, which can be attributed to high penetrations of solar PV.

In Fig. 24 we plot the overall features of the cost-optimized electric power system with varying natural gas fuel costs. Panel (a) depicts the amount of CO_2 emissions from the electric sector compared with 1990 levels. As expected, as the cost of natural gas fuel rises, the amount of CO_2 emitted falls. The decrease happens more rapidly for the lower-cost renewables. Comparing the Low-cost and High-cost Renewable scenarios, we can deduce the benefit of solar PV in CO_2 emission reduction because the cost of wind only varies 9% between the two scenarios and solar PV is completely removed in the High-cost Renewable scenario (see Fig. 24). It is striking that the combination of wind and solar PV (see Low-cost Renewables scenario in Figs 23 (a) and 24 (c)) is far more effective at carbon mitigation than wind on its own (see High-cost Renewables scenario in Figs 23 (c) and 24 (c)).

Figure 24 (b) shows how the total annual cost of the system increases monotonically with increasing natural gas fuel cost as expected. The increase in costs can be approximated as linear until the $\sim$60% carbon-emission-free generation level is reached and then increases more slowly. The carbon-emission-free generation is represented in panel (c). The logistic nature of the carbon-emission-free generation share is clearly depicted. Curtailment, one of the main causes of the increasing marginal cost of additional wind and solar PV generation at high penetration levels, is shown in panel (d). Curtailment is the result of two factors. First the generators can be correlated and so over production will happen, which is more pronounced for solar PV (comparing the Low-cost Renewable with the High-cost Renewable scenarios). Secondly, the HVDC transmission capacity may reach its allowed limits (12 GW) and congestion can stop the flow of electricity. Interestingly, if all the electricity that was curtailed in the Low-cost Renewable scenario at $14 / MM Btu of natural gas fuel was able to be stored and then dispatched at some later time then carbon-emissions-free generation would be able to rise from 84% to 91%; however, it may still not be economical to do so.

We do not show the dispatch stacks for the natural gas sensitivity study because they do not provide any further meaningful information regarding the performance of the electric power systems compared to those shown in subsection 2.1. However, the histograms that show the yearly values for the ramp rates and the surplus/shortfall do show interesting features and insight. Figure 25 displays histograms of surplus and shortfall of carbon-emission-free generation for four example configurations. In subsection 2.1, we suggested that as higher amounts of wind and solar PV generation is added to the electric power mix, the histograms would become broader, shallower, and move to the right; Fig. 25 supports that claim. In panel (a) there is very little variable generation and accordingly the histogram is dominated by the evolution of the demand over the year. There is still nuclear, hydroelectric, and a small amount of wind and solar PV that means the histogram is not exactly the electric load variation. Notice that there is no time where the generation from carbon-emission-free generation exceeds the demand; a fact supported by the curtailment plot in Fig. 24. With successive increases in natural gas fuel cost, the histogram becomes less sharp and its peak moves right towards the zero-line. The plot in panel (d) shows the peak of the histogram very close to the zero line. From Fig. 25 one component of the increasing marginal cost of wind and solar PV with rising natural gas fuel cost is easier to understand. The area of the histogram to the right of the zero line is larger at high cost of natural gas fuel than at lower cost. Curtailed or wasted electricity is an implicit cost for variable generators and impacts their value. From a system control perspective, it is clear that the electric power system represented by panel (a) would have different characteristics to that in panel (d). Indeed, the way the system would need to be managed must change to accommodate the variable generation.

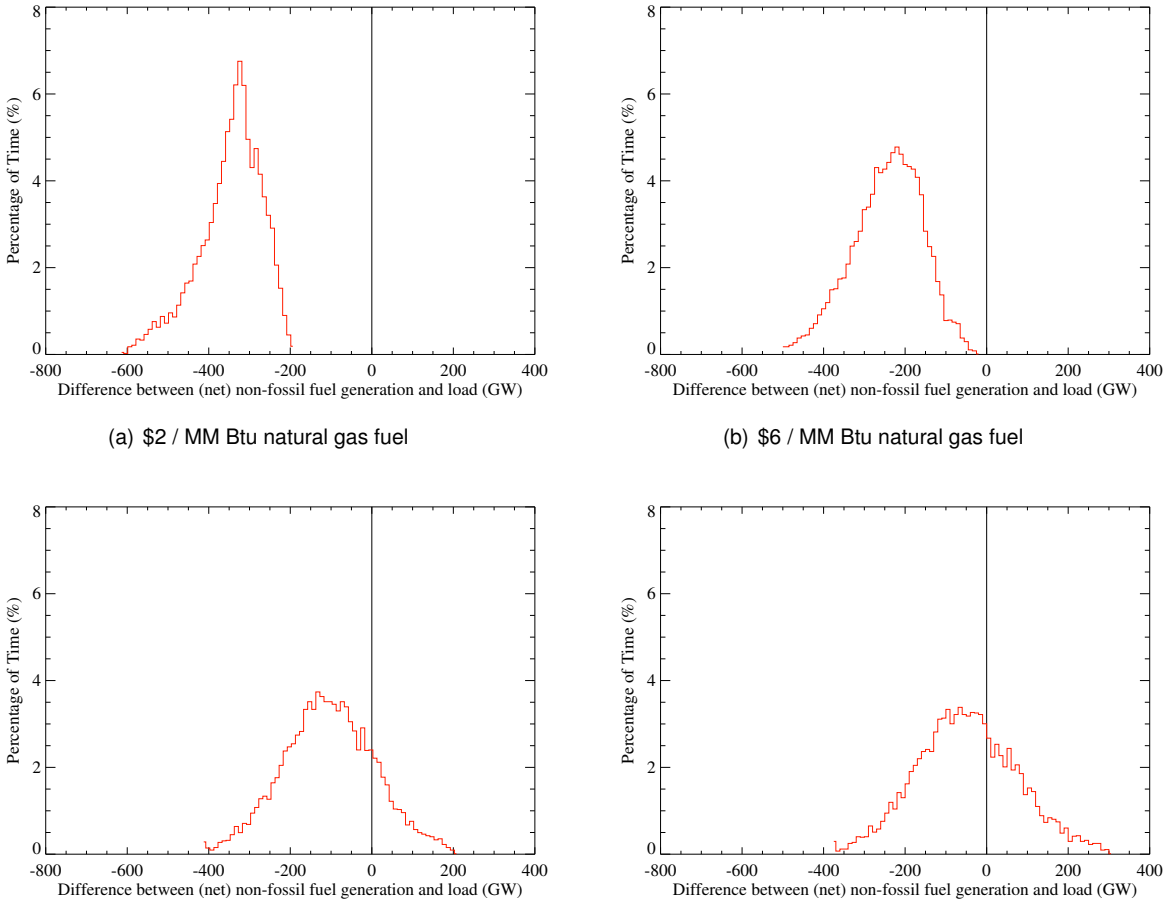

(a) $2 / MM Btu natural gas fuel

(b) $6 / MM Btu natural gas fuel

(c) $10 / MM Btu natural gas fuel

(d) $14 / MM Btu natural gas fuel

Figure 25: Histograms of the difference between the aggregated carbon-free-emission generation and the demand in GW for the US electric power sector. The panels display the values for the 2007 data year Low-cost Renewables scenario. Negative values denote a need for fossil fuel generation and positive values represent requirements for curtailment of variable generation. The vertical axes represent the percentage of time represented by each 10 GW bin. The panels show cost-optimal systems created from the natural gas fuel cost being (a) $2 / MM Btu, (b) $6 / MM Btu, (c) $10 / MM Btu, and (d) $14 / MM Btu. It can be seen that with increasing cost of natural gas fuel the histogram moves to the right, signifying a greater use of wind and solar PV. In addition, the histogram becomes broader and shallower, therefore increasing ramping of the fossil fuel generators.

For completeness, we include Fig. 26 that displays the aggregated natural gas hourly ramp rates. The panels illustrate the dramatic difference in the electric system behavior with vastly divergent generation mixes. The vast majority (over 99.5%) of ramps in panel (a) are contained within $\pm$7% of capacity per hour of the natural gas power plant fleet, while in (d) over 5% of ramps are greater than that range. The extreme ramps are still rare, but there is a noticeable increase. Interestingly, there is also an increase in the frequency of zero ramps.

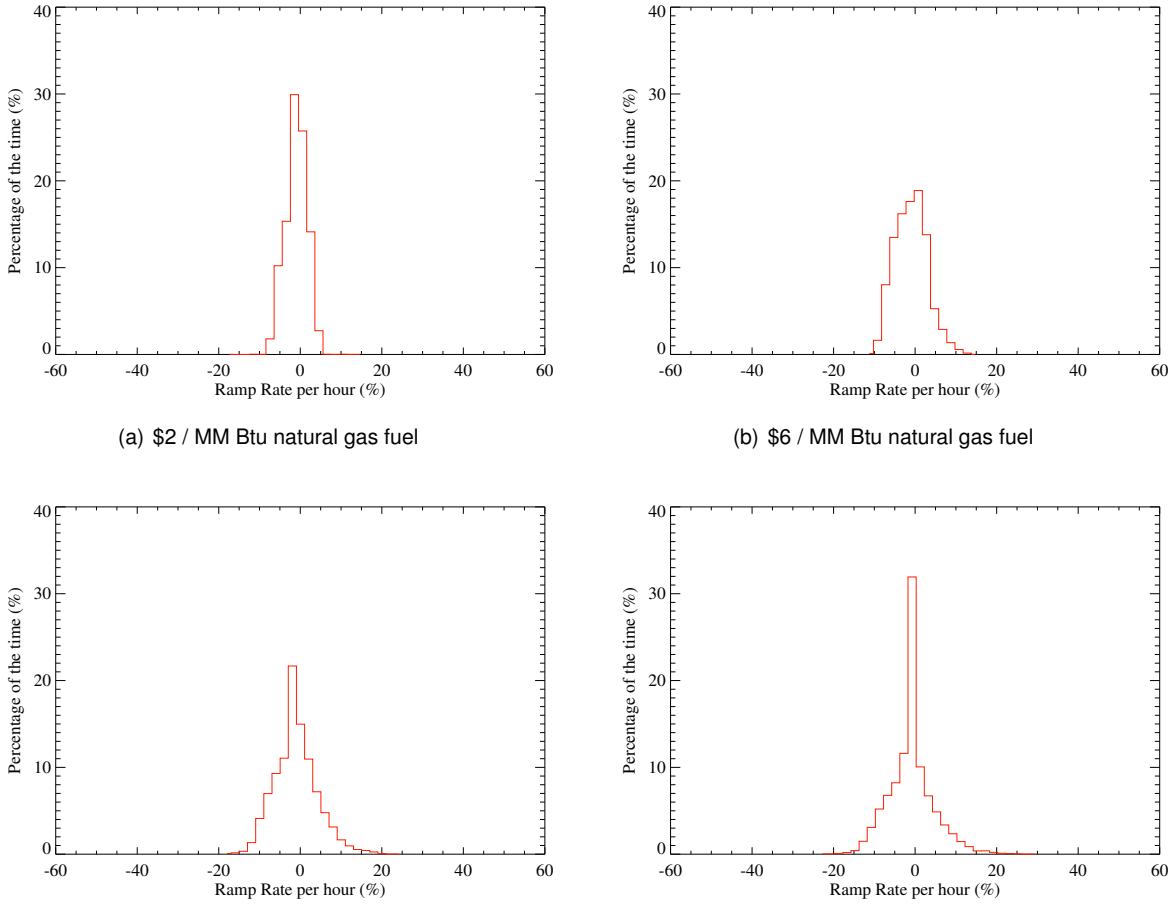

(a) $2 / MM Btu natural gas fuel

(b) $6 / MM Btu natural gas fuel

(c) $10 / MM Btu natural gas fuel

(d) $14 / MM Btu natural gas fuel

Figure 26: Histograms of the aggregated hourly rate of change of generation output (ramp rates) for the natural gas power plants. The vertical axes represent the percentage of time the system has a ramp rate of a certain value (2% bin size). The horizontal axes show the aggregated ramp rates of the natural gas power plant fleet. The panels show cost-optimal systems created from the natural gas fuel cost being (a) $2 / MM Btu, (b) $6 / MM Btu, (c) $10 / MM Btu, and (d) $14 / MM Btu. Immediately we can see that (a) and (d) have similar peaks at 0% ramp rate for the natural gas fleet, but that (d) has wider tails. The wider tails indicate a lower fraction of small ramps, but increased fraction of larger ones.

The natural gas sensitivity study has facilitated a look at how wind and solar PV generation responds to varying costs of dispatchable generation. It shows that more wind and solar PV is added with increasing fuel costs, but the rate of adoption starts to slow after $\sim$60% of carbon-emission-free generation due to curtailment and correlation effects.

2.3 The effect of coal plants (without CCS) in the optimization

We did not include coal for either the geographic scaling and the natural gas sensitivity studies. The main reason behind that decision was to limit the degrees of freedom of those investigations. However, we also considered that for the purposes of atmospheric carbon dioxide mitigation coal has some limitations: first, coal has high CO_2 emissions compared with natural gas; second, when considering coal with carbon capture and sequestration (CCS) it is not cost competitive against natural gas; and third, coal has an aging generation fleet that will almost entirely be retired by 2030. Nevertheless, currently coal is a dominant fuel source for electricity production in the US, thus it is instructive to study how the inclusion of coal as an option in the model impacts the cost-optimized electric power system for 2030.

To study the effects of coal plants in the electric power systems, we built a more comprehensive optimization model. We needed to do this primarily because coal has different characteristics than natural gas power plants. In addition, the more comprehensive model can be used for other sophisticated studies in the future. There are two main changes to the optimization model compared with the version used in the previous two studies, which are included to account for coal generation. First, a load-following reserve of 7% of total demand must be maintained at each time step. Secondly, coal power plants have a minimum power output requirement. These new improvements are added to the model described in subsection 1.6. The simpler model was used for the geographic and natural gas sensitivity because of runtime constraints and to limit degrees of freedom that can obscure trends.

For the present study, we only allowed wind, solar PV, natural gas, coal, nuclear and hydroelectric generators. We enforce a 7% load following reserves constraint because if a coal plant goes offline it is unlikely to recover within an hour (a single time step). Since coal power plants have much more thermal inertia than natural gas power plants and generally cannot operate at lower output levels efficiently, we included a minimum power output constraint for coal power plants such that output cannot drop below 65% of installed capacity (not including the planning reserves) at any time step.

The costs of the generators (except coal) are provided by Table 3, while the cost of coal is set to (in 2013$) $1.47 / W for capital costs, $3.04 / MMBtu for fuel, and $5.01 / MWh for variable O&M (*74*). Additionally, we supplied the model with the heat rate for the coal generation fleet. The value taken was 9,238 Btu / kWh, which represents a 12% decrease from the average value for the US coal fleet in 2012 (10,498 Btu / kWh) to take into account the recent EPA ruling on CO_2 from electricity producers (*114*). One last piece of extra information for the comprehensive optimization is the location of existing coal plants as of 2012. The information is used by the optimization as locations where coal power plants can be developed. The maximum size of installation is 10 GW (the same as for the natural gas power plants).

Figure 27 displays cost-optimal configurations for a single connected contiguous US electric power system. We performed the three cost scenarios as in the geographic scaling study, while holding the cost of coal as set out in the previous paragraph. Immediately evident is that a national HVDC transmission system is constructed by the optimization in all three cost scenarios; further reinforcing evidence that the US electric power sector would be more economical with such a national system. In every scenario, wind is constructed in large quantities in Kansas suggesting these locations are some of the most economical in a connected system. Strikingly, there are much lower amounts of wind and solar PV developed in these scenarios with coal compared with the same system that does not include coal.

To identify the electric power system breakdown by technology, we display the installed capacity and

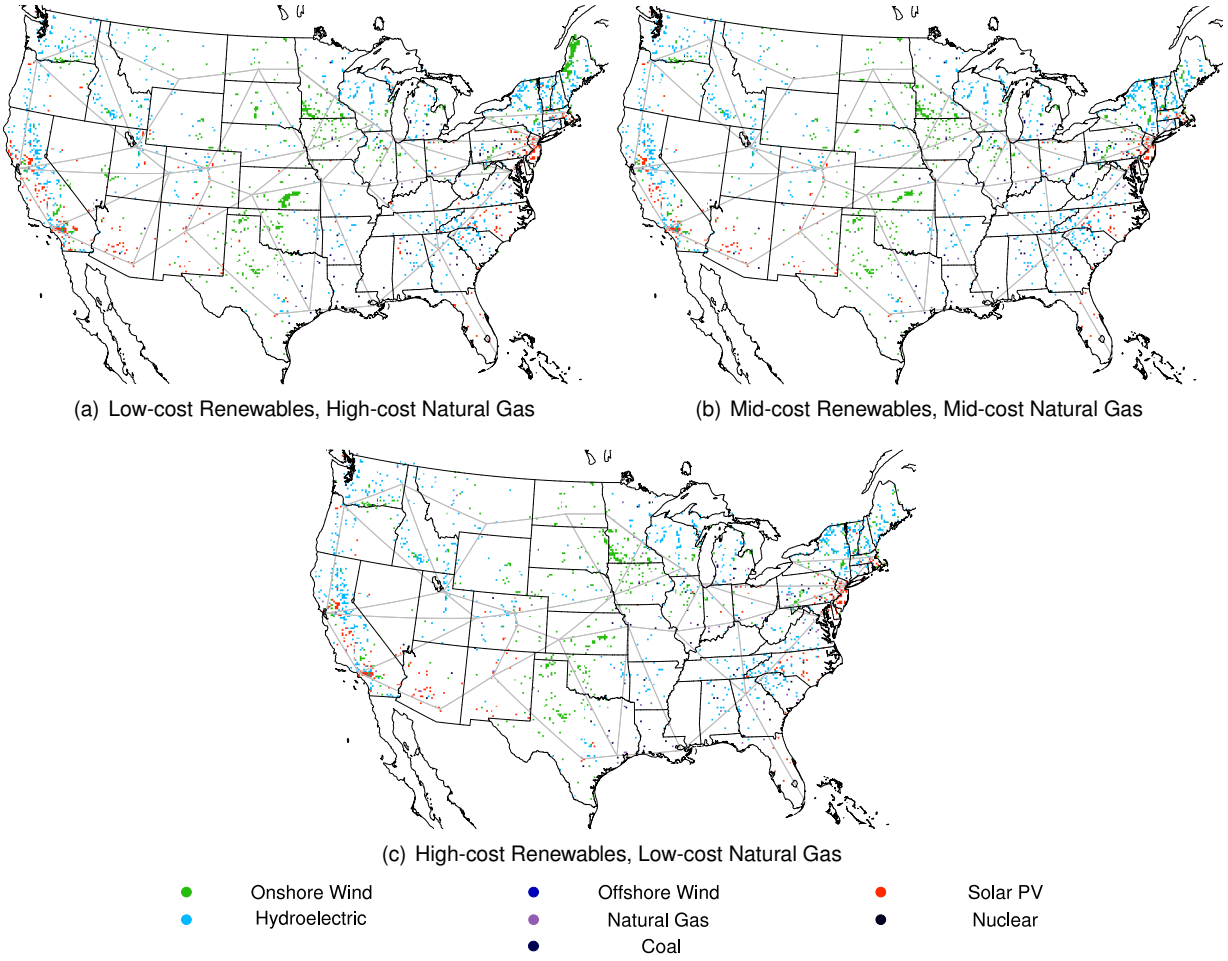

Figure 27: Cost-optimal configurations of a single connected contiguous US electric power sector that include coal power plants. We show optimization configuration for (a) Low-cost Renewable High-cost Natural Gas, (b) Mid-cost Renewable Mid-cost Natural Gas, (c) and High-cost Renewable Low-cost Natural Gas. The three configurations show less variation than in the geographic scaling or natural gas sensitivity studies. It can be seen that the most wind and solar PV is deployed in the LRHG scenario, but surprisingly the least is developed in the MRMG scenario.

generation share in Fig. 28. It is clear that more wind and solar PV is installed and used in the LRHG scenario than the other cost scenarios. For the MRMG scenario, wind and solar PV are squeezed out in favor of coal and natural gas. In the HRLG scenario, natural gas is cheaper and so it removes coal power plants, which allows more wind-generated power to be used within the system. Interestingly, the installed capacity of wind is up compared to 2012 in all scenarios by 40%–76%. In the LRHG scenario, solar PV replaces natural gas to help supply power for the summer time peaks. From Fig. 28, we can deduce that the inclusion of coal severely limits the economic development of wind and solar PV beyond a small share of the electricity generation mix. It should be noted that the EPA Clean Air Act efficiency improvements have been included for coal, which makes them cheaper to run and more economic. Without this efficiency

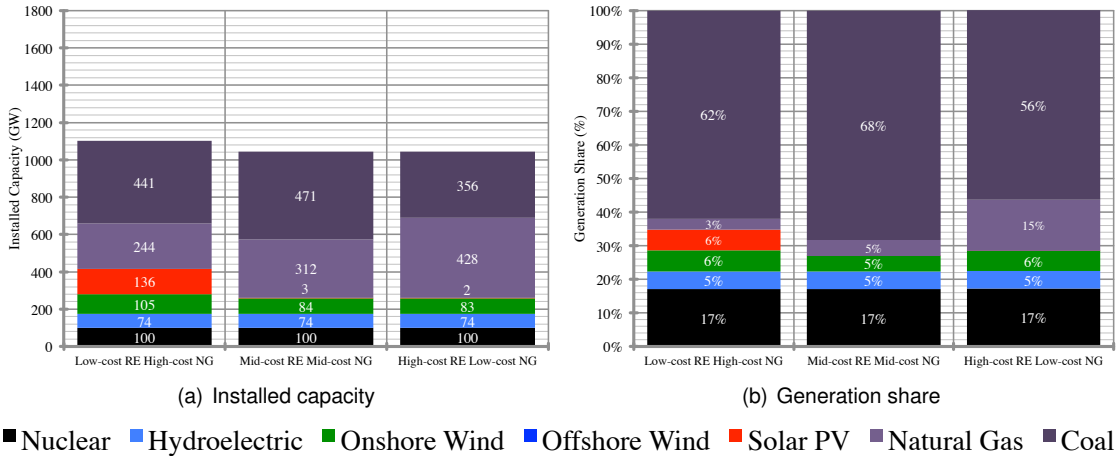

Figure 28: The installed capacity in GW (a) and generation share (b) by technology for each cost scenario. Coal power production dominates in all cases, but its installed capacity share varies more dramatically. In the LRHG scenario wind and solar PV development is noticeable, but it appears to happen at the expense of natural gas. The installed capacities between different cost scenarios are very similar, while the generation share changes are more pronounced.

improvement, the share of coal would be lower. The efficiency improvements could have a possible steep capital cost at older existing coal power plants, but our model assumes these retire and new ones are built in their place. If a coal power plant is fully owned by the operator, the cost of generating electricity is almost entirely fuel related and therefore efficiency changes will reduce its profitability (as capital will need to be spent improving the power plant). Additionally, if different constraints were to be imposed on the coal generation fleet within the model (such as a lower minimum power output constraint or higher coal fuel costs), the results could be drastically different.

Figure 29 contains all the main overarching features of the optimizations that include coal power plants. It is immediately obvious that the CO_2 emissions are higher than 1990 levels in all three cost scenarios. Therefore, including coal in the electric power mix without CCS at the assumed cost levels will thwart any mitigation possibilities. The total system costs are very similar between the different cost scenarios. There is greater carbon-emissions-free generation in the LRHG scenario compared with the HRLG scenario, but somewhat surprisingly, the CO_2 emissions are higher. This can be explained by the fact that the coal power plants emit more CO_2 per unit of electricity than natural gas and this share changes substantially between the two scenarios. In other words, the lack of natural gas generation in the LRHG scenario has negated the carbon mitigation impact of more wind and solar PV generation; while in the HRLG scenario, less generation comes from wind and solar PV, but more comes from natural gas, hence more CO_2 is mitigated. In all three cases, the curtailment rate is very high, between 16 and 43% of wind and solar PV generation. The high rate can be attributed to the lack of flexibility available to the coal power plant fleet to ramp down below 65%. Overall, Fig. 29 paints a bleak picture for carbon mitigation if coal power plants remain dominant without added flexibility to accommodate wind and solar PV generation. In contrast, with more flexibility (e.g. ability to gasify the coal and then run as a natural gas combined cycle plant) the coal power plants could contribute as in dispatchable generators as shown in the geographic scaling study (i.e.

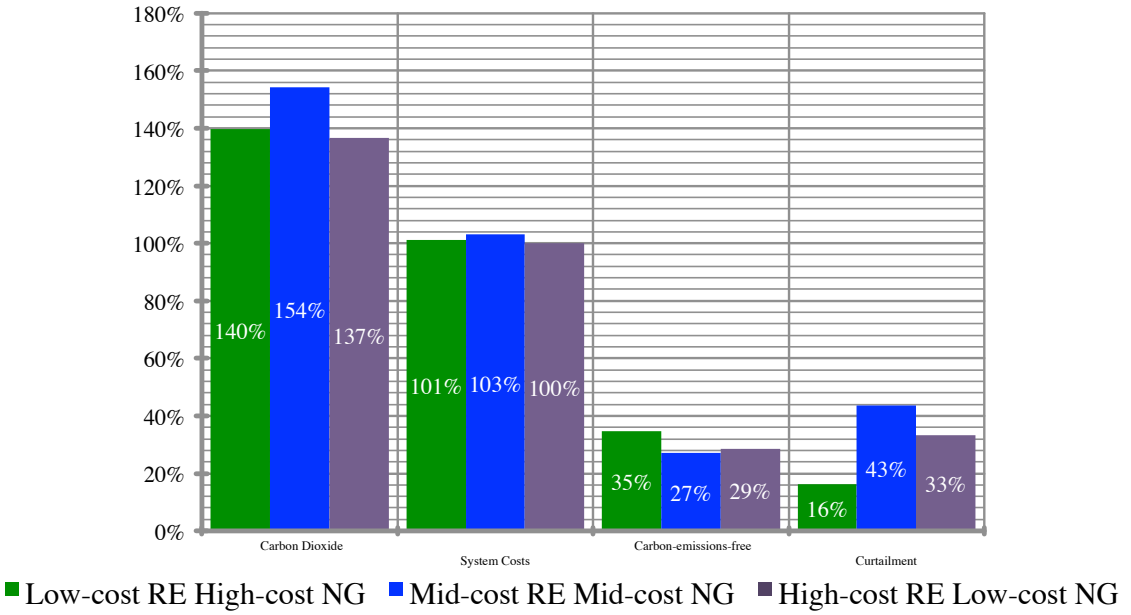

Figure 29: A summary of results from the optimizations with the addition of coal power plants. We show all three cost scenarios. From left to right we have: the carbon dioxide emissions from the system relative to 1990 levels; the total system costs relative to the HRLG with coal scenario; the percentage of carbon-emission-free generation; and the percentage of curtailment relative to the wind and solar PV generation. All scenarios emit much more CO_2 compared with 1990 levels, the costs are almost identical to each other, and curtailment is substantial.

replace some of the natural gas power plants). It is worth remembering that the conclusions in the present paper are all based upon total least cost. Thus, added constraints could enforce desired levels of CO_2 reductions at specified levels of cost increases.

Figure 30 shows how dominant coal is as a supplier of electricity in these scenarios. The coal at times will push wind and solar PV power to be curtailed because it is more cost efficient to waste wind and solar PV electricity than ramp down the coal plants. The plots also illustrate that the coal plants must vary their outputs frequently to compensate for the electric load diurnal cycle and variable generation. The additional ramping of these generation sources will have impacts on the system that are not modeled here (for example, changing heat rates or efficiency). The ramping of coal plants is more pronounced in the LRHG scenario than in the HRLG scenario. The extra ramping is due to two factors; first solar PV creates a midday spike in electric generation and second there is less natural gas in the LRHG scenario and so coal must compensate. The cost-optimal configurations from Fig. 27 do include 24–46 GW more onshore wind than was installed by the end of 2012. Moreover, the systems have almost the same installed capacity as there was in 2012, despite providing $\sim$14% more electricity. The primary reason for the lack of increased capacity is the HVDC transmission system that allows capacity diversity that is not currently possible. The CO_2 emissions are 17–33% higher than those in 2012 from the electricity sector (*74*).

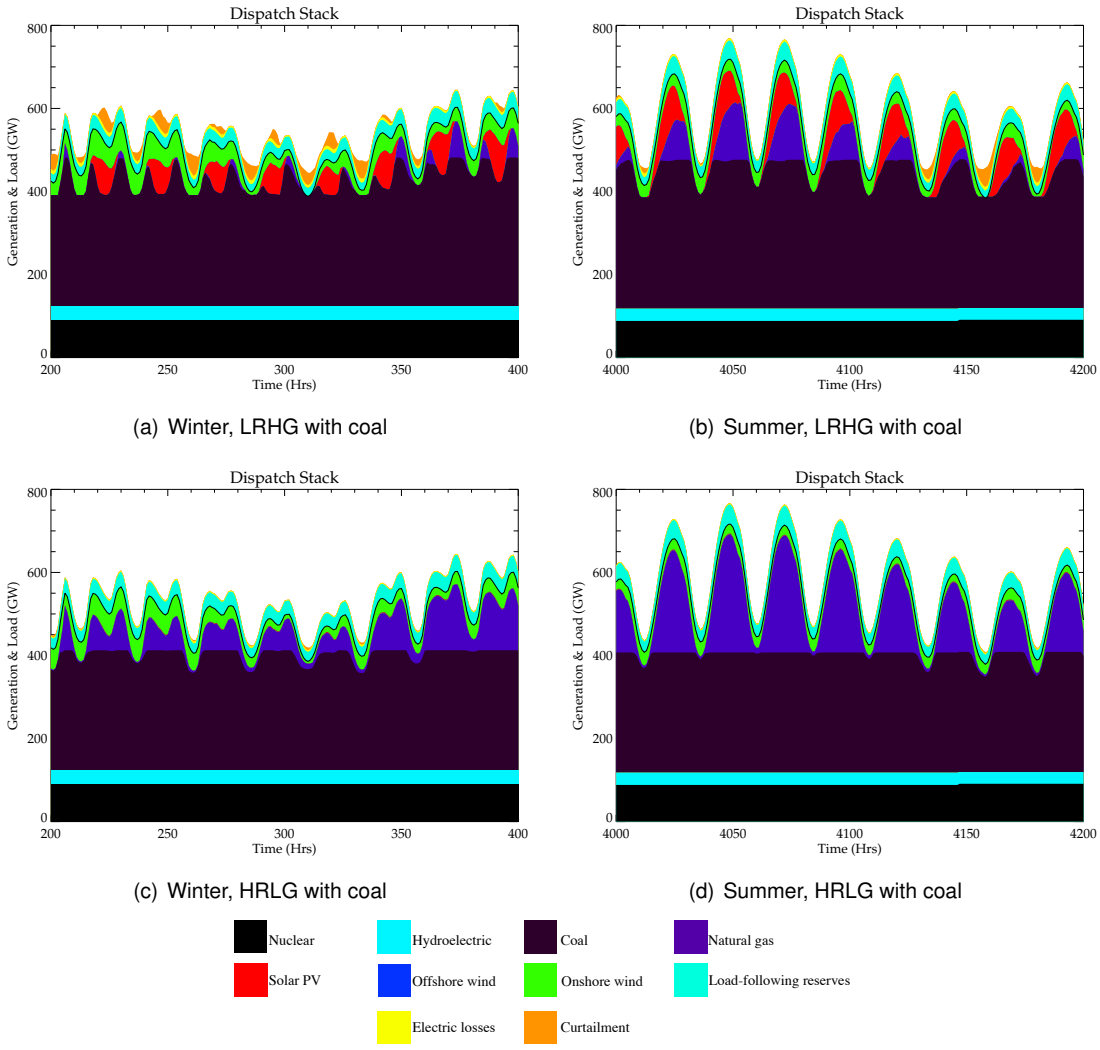

Figure 30: Sample wintertime and summertime dispatch stacks for the Low-cost Renewable High-cost Natural Gas (LRHG) with coal (a, b) and High-cost Renewable Low-cost Natural Gas (LRHG) with coal scenarios for the 2007 data year. The vertical axes display the generation and load requirements in GW and the horizontal axes label the hour of the optimization. The dispatch stacks show the time period of 08:00 UTC January 8th to 16:00 UTC January 16th for winter and the time period of 22:00 UTC June 15th to 06:00 UTC June 24th for summer. Each panel shows the aggregated US electric power sector generation and demand. The panels illustrate how different the electric power system will need to operate with the addition of wind and solar PV generation.

3 Summary of Assumptions and Key Model Features

One of the goals of the present paper is to quantify how much of the US electric demand could be met by wind and solar PV generation if a long-distance HVDC transmission network were overlaid upon the current US grid. Although locally the prevailing weather conditions may not be conducive for high wind and

solar power production, the HVDC grid would allow wind and solar PV power to be imported from more distant locations where excess wind and solar PV power are being generated. The level of penetration of wind and solar PV power is determined solely on an economic basis; using a cost-sensitive optimization based on three years of meteorological data at hourly resolution obtained from a state-of-the-art numerical weather prediction assimilation model on a 13-km grid over the US.

As with all modeling endeavors, the optimization model has key assumptions and features, which are described in detail throughout these supplemental materials. For the readers' convenience, we have compiled the present section to list some of the most important assumptions and features. Some of the main features of the optimization model are:

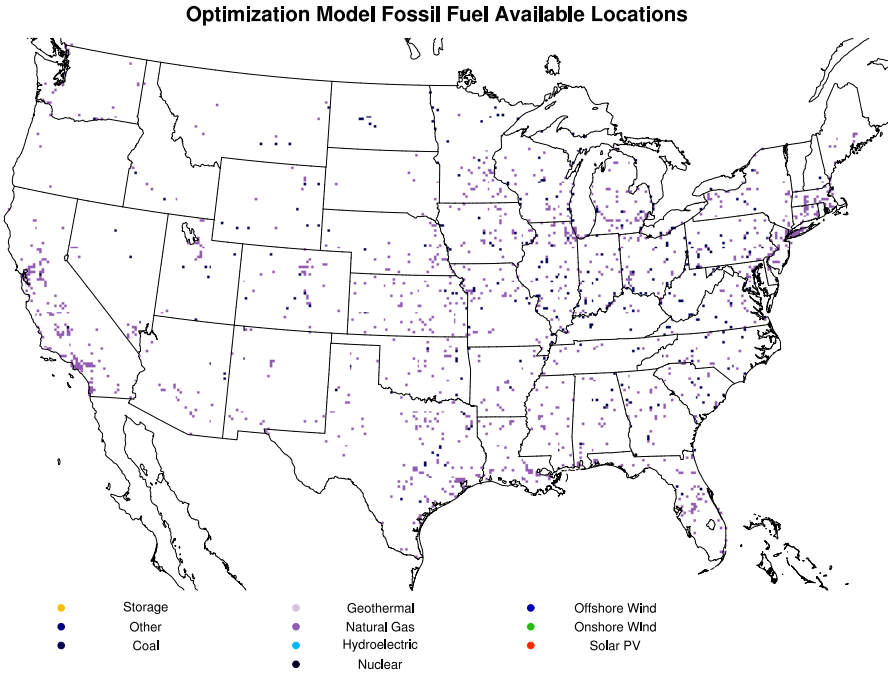

Figure 31: The natural gas power plant siting options in the optimization model. Natural gas plants can be built at existing natural gas and coal sites.

- Electric load is met or exceeded by the generation at every hourly model time step in every nodal area.
- The natural gas plants can only be sited at geographic locations that have fossil fuel plants in 2012 (shown in Fig. 31), to ensure that the necessary infrastructure and permitting is in place.
- Utility-scale solar PV is considered, but rooftop solar PV is not. The transmission handling of the optimization model is high level and does not extend beyond the last busbar before the customers are reached in each of the 256 nodal areas, where the rooftop solar PV resides. Further, the optimized

solutions tends to locate solar PV near nodal centers (cities) that can be substituted, in part, by rooftop solar PV if the cost becomes favorable.

- Indirect costs associated with approval of new generation facilities (legal, environmental, health, etc.) are not explicitly accounted for. However, the meta-analysis of the cost projections does include studies that do account for part of these costs.
- Negative externalities often associated with fossil fuel electricity generation are not assigned a cost in the present model, i.e. no carbon or other emissions tax is applied for the results presented and discussed in the present paper.
- Hydroelectric generation is dispatched based upon historical monthly average values for the three data years to account for the seasonal hydrological cycle.
- Nuclear generation is dispatched based on the lowest historical monthly average for the last decade to be conservative with respect to its production.
- Nuclear and hydroelectric generation is allowed to ramp by small amounts (2.5% and 5%, respectively) around the historical values for numerical stability.
- The modeled system is optimized, having the benefit of load distribution and weather data a priori; hence the resulting optimization is free from transmission congestion. Market dynamics associated with capacity-dependent transmission and weather forecast uncertainty are not modeled.
- Within each nodal area, AC electrical losses are simply modeled based on geodesic distance between generator and node center. The local AC distribution network is not modeled explicitly, but is assumed to be capable of providing necessary transmission within each nodal area.
- An additional overlay HVDC transmission system is used to transmit power between the 32 regional market areas. This is done because a) it is the most cost-effective from a capacity (MW-mile) basis over long distances, b) the associated line losses are significantly lower than with AC transmission, and c) there are no steady-state stability or other AC phase problems across long distances.

Some of the main assumptions used to build the model are:

- Three cost scenarios are presented in the present paper. All generators available to the optimization are assumed to have a 30-year service life. The annual plant cost is amortized over its service life using a real discount rate of 6.6%. The 2025 projection of costs are considered “Low”, present-day costs are considered “High” and “Mid” is a simple average of these two costs. The natural gas turbine technology is assumed to be mature and plant cost is not varied between the three cost scenarios. The natural gas fuel cost is taken from the 2040 high resource, reference, and low resource scenarios from the EIAs 2013 Annual Energy Outlook. Costs are held constant throughout the optimization period and across geographic regions.
- The optimization routine provides the single best solution in terms of cost. Numerous solutions exist that are slightly sub-optimal, but possess very similar features in terms of siting, dispatch, etc.

- The load-following and planning reserve requirements are identical at all geographic locations.
- Natural gas plants have no ramping constraints in the present paper. However, gas sector ramp rates were analyzed for the resulting systems and were found to be between 60% / hour up-ramp and 60% / hour down-ramp which is well within current combined cycle gas turbine capability.
- There is no pre-determined dispatch order. The cheapest generation sources will be brought online as needed at each model time step.
- Nuclear, hydroelectric, wind and solar PV generators that existed by the end of 2012 are assumed to be in-place and operational in all optimization scenarios, which we show in Fig. 32.
- Electricity storage is considered in the optimization model; however, current and projected storage costs resulted in it never being selected as an option; so it was removed to simplify the description of the model. Storage is selected if its price is considerably reduced, or other constraints are enforced (such as carbon mitigation targets etc.).
- Hourly electric load and meteorological data are sufficient to model the electric power system sub-hourly variability; since the electric grids are on such a large geographic scale.
- The projected load is simply the 2006–2008 load increased by 0.7% per annum. As such, there are no specific assumptions regarding electric vehicle charging or discharging.
- Social and political constraints on the development of generation plants and transmission are not considered; other than exclusion from existing protected areas (National Parks, urban areas, wildlife habitats, shipping lanes. etc.).
- Demand response, load shifting, or future electric load behavior alterations are not accounted for.

The assumptions in the NEWS model are designed to be conservative with respect to the potential of wind and solar PV to integrate within the electricity system. The 30-year service life with a 6.6% real discount rate is maintained across three generation cost scenarios that bracket the published projections (*74–85*). There are localized cost effects that could result in the optimal resource locations becoming unattractive for development; possibly reducing the penetration of wind and solar PV. If hydroelectric power could ramp much more than in the model more wind and solar PV could be integrated as hydro could be dispatched to balance the load instead of firing natural gas plants, reducing costs overall; thus allowing other generators to be deployed. Transmission costs clearly will effect the development of wind and solar PV. In addition, if large amounts of wind and solar are to be developed transmission congestion will need to be overcome and transmission development will be necessary. On balance, taking into account all of the effects of the various assumptions, the authors believe the net effect on the results will be small in terms of the overall penetration for wind and solar PV for a national system. Even storage cannot handle the large scale variations in wind and solar in the same manner as larger geographic areas can.

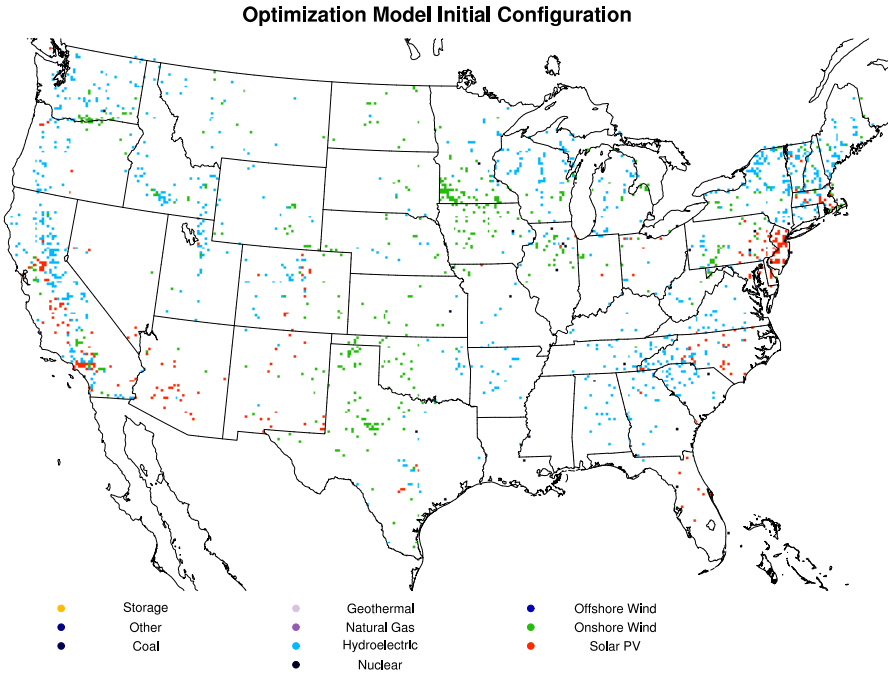

Figure 32: The optimization initial configuration. Existing (2012) wind, solar PV, nuclear and hydroelectric power plants are shown in the RUC grid space.

References and Notes

33. S. G. Benjamin, G. A. Grell, J. M. Brown, T. G. Smirnova, R. Bleck, *Mon. Weather Rev.* **132**, 473 (2004).

34. S. G. Benjamin, *et al.*, *Mon. Weather Rev.* **132**, 495 (2004).

35. X. Wang, *Mon. Weather Rev.* **138**, 2990 (2010).

36. A. Hammer, D. Heinemann, E. Lorenz, B. Lockehe, *Solar Energy* **67**, 139 (1999).

37. F. Vignola, R. Perez, Solar resource gis data base for the pacific northwest using satellite data - final report, *Tech. rep.* (2004).

38. R. Houborg, H. Soegaard, W. Emmerich, S. Moran, *Int. J. Remote Sens.* **28**, 4509 (2007).

39. F. Vignola, P. Harlan, R. Perez, M. Kmiecik, *Solar Energy* **81**, 768 (2007).

40. B. B. Hicks, J. J. DeLuisi, D. R. Matt, *Bull. Am. Meteorol. Soc.* **77**, 2857 (1996).

41. J. A. Augustine, G. B. Hodges, C. R. Cornwall, J. J. Michalsky, C. I. Medina, *J. Atmos. Ocean. Technol.* **22**, 1460 (2005).

42. K. Wang, J. Augustine, R. E. Dickinson, *J. Geophy. Res.* **117**, D23105 (2012).

43. J. J. Michalsky, *et al.*, *J. Geophys. Res* **108**, 4108 (2003).

44. F. Vignola, J. Michalsky, T. Stoffel, *Solar and Infrared Radiation Measurements* (CRC Press, Florida, USA, 2012).

45. J. W. Spencer, *Search* **2**, 172 (1971).

46. K. Pearson, *Biometrika* **6**, 59 (1908).

47. H. Theil, *Economic Forecasts and Policy*, Contributions to economic analysis (North-Holland Publ.., Amsterdam, Holland, 1961).

48. J. M. Stanton, *J. Stats. Ed.* **9**, 3 (2001).

49. T. Burton, D. Sharpe, N. Jenkins, E. Bossanyi, *Wind Energy Handbook* (John Wiley and Sons, Chichester, England, 2001).

50. D. L. King, S. Gonzalez, G. M. Galbraith, W. E. Boyson, Performance Model for Grid-Connected Photovoltaic Inverters, *Tech. rep.*, Sandia National Laboratories, Albuquerque, New Mexico (2004).

51. M. A. Green, K. Emery, Y. Hishikawa, W. Warta, *Progress in Photovoltaics: Research and Applications* **18**, 346 (2010).

52. G. M. Masters, *Renewable and Efficient Electric Power Systems* (John Wiley and Sons, Hoboken, New Jersey, 2004).

53. W. D. Soto, S. A. Klein, W. A. Beckman, *Sol. Energy* **80**, 78 (2005).

54. R. Karsteadt, D. Dahle, D. Heimiller, T. Nealon, Assessing the Potential for Renewable Energy on National Forest System Lands, *Tech. rep.*, United States Department of Agriculture Forest Service and National Renewable Energy Laboratory (2005).

55. Center for International Earth Science Information Network (CIESIN)/Columbia University, and Centro Internacional de Agricultura Tropical (CIAT), Gridded Population of the World, Version 3 (GPWv3): Population Density Grid. Palisades, NY: NASA Socioeconomic Data and Applications Center (SEDAC), `http://sedac.ciesin.columbia.edu/data/set/gpw-v3-population-density` (2005).

56. National Renewable Energy Laboratory, Solar Prospector Map Service, `http://maps.nrel.gov/prospector`.

57. M. Schwartz, D. Heimiller, S. Haymes, W. Musial, Assessment of Offshore Wind Energy Resources for the United States, *Tech. rep.*, National Renewable Energy Laboratory (2010).

58. DOC/NOAA/NESDIS/NGDC > National Geophysical Data Center, NESDIS, NOAA, U.S. Department of Commerce, Great Lakes Bathymetry, `http://www.ngdc.noaa.gov/mgg/` (2009).

59. Cape Wind, `http://www.capewind.org/FAQ.htm`.

60. BelWind, http://belwind.eu/en/facts-and-figures/.

61. National Oceanic and Atmospheric Administration, Marine Cadastre Multipurpose Dataset, http://www.marinecadastre.gov/default.aspx.

62. C. Potter, *et al.* (7th International Workshop on Large Scale Integration of Wind Power and on Transmission Networks for Offshore Wind Farms, 2008).

63. P. Denholm, M. Hand, M. Jackson, S. Ong, Land-Use Requirements of Modern Wind Power Plants in the United States, *Tech. rep.*, National Renewable Energy Laboratory (2009).

64. Federal Energy Regulatory Commission, Form 714, http://www.ferc.gov/docs-filing/forms/form-714/overview.asp.

65. IEA, Global Electric Statistics, http://www.iea.org/statistics/topics/Electricity/.

66. B. Gjorgiev, M. Cepin (20th International Conference on Nuclear Energy For New Europe, 2011).

67. P. Low, M. Annamalai, B. Kuepper, E. Nielsen, D. Hua, Climate and Hydrology Datasets for use in the RMJOC Agencies' Longer-Term Planning Studies - Part III - Reservoir Operationals Assessment: Columbia Basin Flood Control and Hydropower, *Tech. rep.*, Bonneville Power Administration and The Army Corp of Engineers (2011).

68. US Nuclear Regulatory Commission, Operating Nuclear Power Reactors, http://www.nrc.gov/info-finder/reactor/.

69. Global Energy Observatory, Current List of Hydro Power Plants, http://globalenergyobservatory.org/list.php?db=PowerPlants&type=Hydro.

70. US Energy Information Administration, US Nuclear Generation and Generating Capacity, http://www.eia.gov/nuclear/generation/index.html.

71. US Energy Information Administration, Electric Power Monthly, http://www.eia.gov/electricity/monthly/epm_table_grapher.cfm?t=epmt_1_1.

72. Bureau of Economic Analysis, Gross Domestic Product (GDP), www.bea.gov/national/xls/gdplev.xls.

73. Annual Energy Outlook, *Tech. rep.*, US Energy Information Administration (2011).

74. Annual Energy Outlook 2012 with Projections to 2035, *Tech. rep.*, U.S. Energy Information Administration (2012).

75. M. M. Hand, *et al.*, Renewable Electricity Futures Study, *Tech. rep.*, National Renewable Energy Laboratory, Golden, Colorado (2012).

76. Annual Energy Outlook 2009, *Tech. rep.*, U.S. Department of Energy (2009).

77. Evaluating a Proposed 20% National Renewable Portfolio Standard, *Tech. rep.*, National Renewable Energy Laboratory (2009).

78. Annual Energy Outlook 2010, *Tech. rep.*, U.S. Department of Energy (2010).

79. G. Keith, *et al.*, Beyond Business as Usual: Investigating a Future without Coal and Nuclear Power in the US, *Tech. rep.*, Civil Society Institute, Synapse Energy Economics Inc. (2010).

80. W. Musial, B. Ram, Large-Scale Offshore Wind Power in the United States, *Tech. rep.*, National Renewable Energy Laboratory (2010).

81. M. Bolinger, R. Wiser, Understanding Trends in Wind Turbine Prices over the Past Decade, *Tech. rep.*, Ernest Orlando Lawrence Berkeley National Laboratory (2011).

82. Working Group III, Renewable Energy Sources and Climate Change Mitigation, *Tech. rep.*, Intergovernmental Panel on Climate Change (2011).

83. SunShot Vision Study, *Tech. rep.*, U.S. Department of Energy (2012).

84. Updated Capital Cost Estimates for Electricity Generation Plants, *Tech. rep.*, U.S. Energy Information Administration (2010).

85. Black and Veatch Hldg Co., Staff Report, 2012: Cost and Performance Data for Power Generation Technologies, *Tech. rep.*, DOE National Renewable Energy Laboratory (2012).

86. Bureau of Labor and Statistics, Consumer Price Index, `ftp://ftp.bls.gov/pub/special.requests/cpi/cpiai.txt`.

87. Annual Energy Outlook 2013, *Tech. rep.*, U.S. Department of Energy (2013).

88. Centro Solar, 30 year performance warranty on Centrosolar glass-glass modules, `http://www.centrosolar.com/en/customers/news-events/news/news-single/article/30-jahre-leistungsgarantie-auf-glas-glas-module-von-centrosolar/`.

89. Solar World, SunModule Protect, 30 year limited warranty, `http://www.solarworld-usa.com/~/media/www/files/warranties-certifications/solarworld-sunmodule-protect-30-year-warranty.pdf`.

90. Worldwide Energy and Manufacturing USA Co., Limited, Limited Warranty for Amerisolar PV Module(s) 2012, `http://www.weamerisolar.com/pdf/01.pdf`.

91. Wind, W. P. T. Office, WindVision: A New Era for Wind Power in the United States, *Tech. rep.*, Department of Energy (2015).

92. M. C. Romberg, Wind turbines for 40 years?, `http://www.renewablesinternational.net/wind-turbines-for-40-years/150/435/85411/`.

93. M. P. Bahrman, B. K. Johnson, *IEEE Pow. Energy Magn.* **5**, 32 (2007).

94. M. Bahrman (IEEE Transmission and Distribution Conference and Exposition, 2008).

95. ABB, The longest transmission link in the world - 2,375 kilometers, `http://new.abb.com/systems/hvdc/references/rio-madeira`.

96. ABB, North-East Agra, http://new.abb.com/systems/hvdc/references/north-east-agra.

97. Chinese Government, China building power transmission line of world's largest capacity, http://english.gov.cn/2012-05/14/content_2136713.htm.

98. R. L. Garwin, J. Matisoo, *Proceedings of the IEEE* **55**, 538 (1967).

99. M. P. Bahrman, *Standard Handbook For Electrical Engineers - Chapter 15* (McGraw-Hill Professional, New York, NY, 2006).

100. G. H. Golub, C. F. van Loan, *SIAM J. Numer. Anal.* **17**, 883 (1980).

101. G. H. Golub, P. C. Hansen, D. P. O'Leary, *SIAM J. Matrix Anal. Appl.* **21**, 185 (1999).

102. I. Markovsky, *Stat. and Its Interface* **3**, 329 (2010).

103. A. N. Tikhonov, *Soviet Math. Dokl.* **4**, 1035 (1963).

104. A. N. Tikhonov, V. Y. Arsenin, *Solution of Ill-posed Problems* (Winston and Sons, Washington, 1977).

105. C. L. Archer, M. Z. Jacobson, *J. Geophys. Res.* **108**, 4289 (2003).

106. C. L. Archer, M. Z. Jacobson, *J. Geophys. Res.* **110**, 12110 (2005).

107. W. Short, V. Diakov, *Wind Energy* p. 1099 (2012).

108. R. Rosenthal, GAMS — A User's Guide, *Tech. rep.*, GAMS Development Corporation (2012).

109. American Wind Energy Association, U.S. Wind Industry Fast Facts, http://www.awea.org/learnabout/industry_stats/index.cfm.

110. SEIA, Solar Industry Data, http://www.seia.org/research-resources/solar-industry-data.

111. J. Macknick, R. Newmark, G. Heath, K. C. Hallett, A Review of Operational Water Consumption and Withdrawal Factors for Electricity Generating Technologies, *Tech. rep.*, National Renewable Energy Laboratory (2011).

112. L. Bird, J. Cochran, X. Wang, Wind and Solar Energy Curtailment: Experience and Practices in the United States, *Tech. rep.*, National Renewable Energy Laboratory (2014).

113. K. Gunsch, Phase Two Wind Integration: Discussion Paper, http://www.aeso.ca/downloads/Wind_Integration_Discussion_Paper_-_Phase_Two.pdf.

114. EPA, EPA Clean Air Act 2014, http://www.epa.gov/region07/air/rules/111d.htm.